Development of porous microneedles: a novel approach to collect biomarkers for organ-on-a-chip monitoring

Renata Patrícia Faria Maia

Dissertation for the Degree of Master in Molecular
Bioengineering at Faculdade de Engenharia da Universidade do
Porto and Instituto de Ciências Biomédicas Abel Salazar

Supervisor: Doutor Paulo de Castro Aguiar

Co - Supervisor: Doutora Raquel Oliveira Rodrigues

This work results partially from the project reference EXPL/EMD-EMD/0650/2021, SensBrain4Med, supported by Fundo Europeu de Desenvolvimento Regional (FEDER) and by Fundação para a Ciência e Tecnologia (FCT), IP.

FCT
Fundação para a Ciência e a Tecnologia
MINISTÉRIO DA CIÊNCIA, TECNOLOGIA E ENSINO SUPERIOR

UNIÃO EUROPEIA
Fundo Europeu de
Desenvolvimento Regional

“Pudesse eu não ter laços nem limites
Ó vida de mil faces transbordantes
Para poder responder aos teus convites
Suspensos na surpresa dos instantes!”

Sophia de Mello Breyner Andresen in “Pudesse eu”

This page was intentionally left blank.

ACKNOWLEDGMENT

Escrever esta página, deixa-me num misto de sentimentos. É o fim da mais bela das minhas histórias, cinco capítulos cheios de magia, drama, lágrimas, aventuras e muitas, mas mesmo muitas boas gargalhadas. Ao longo do meu percurso, nem sempre soube que decisões seriam as certas e muitas das vezes arrisquei e abracei o desconhecido. E sinto que depois deste capítulo não me resta mais nada, que não, fazer o mesmo. Todas as minhas escolhas resultaram neste caminho em que os altos superaram em muito os baixos e dou por mim, com as lágrimas nos olhos a pensar nos muitos nomes a quem devo agradecer.

Primeiro, gostava de agradecer a minha coorientadora Raquel Rodrigues, com ela aprendi o amor pela investigação e ciência. Tenho que lhe agradecer a muita paciência que teve para me motivar nos momentos difíceis, ensinar-me e para travar as minhas ideias malucas. A Raquel é realmente um daqueles seres humanos raros que dificilmente temos a sorte de encontrar, e por isso sou grata por a ter como minha orientadora e ter a oportunidade de aprender com ela. Espero sinceramente que seja o início de muitos outros projetos juntas. Quando for “Grande” quero ser como ela.

Ao Professor Paulo Aguiar quero agradecer a generosidade de abraçar este projeto e de se encontrar sempre disponível para me ajudar. Foi um prazer ter cruzado o seu caminho. A todos os membros do CMEMS e do i3s que me ajudaram a realizar testes, conseguir material no laboratório, que deram feedback e que me acompanharam durante este período e que, de alguma forma, me deram alento e motivação para superar os obstáculos que iam aparecendo, obrigada. Destaco aqui: Ricardo Vidal, Paulo Sousa, Vânia Pinto, Graça Minas, Andrea Zillie, Rui Lima.

Os próximos agradecimentos são da maior importância, aos meus pais (Patrícia e Sérgio) aos quais devo a existência e tudo aquilo que sou. Durante estes anos apoiaram-me em tudo e deram-me as ferramentas para chegar

aqui. Orgulho-me muito deles e serei eternamente grata por tudo. São o melhor que tenho na vida. À minha irmã, Nádia, obrigada pelo companheirismo, pelas dores de cabeça que me dá e por ser o ser humano mais chato do mundo, mas sem o qual eu não conseguiria viver.

A toda a minha família muito obrigada pelo amor e orgulho que vejo que sentem por mim, pelo apoio e coragem ao longo deste percurso e por sempre me incentivarem a ser aquilo que quisesse. Tenho o maior orgulho na nossa família e nos valores que me passaram. Aos meus primos, tios e avós, obrigada por tudo, mas principalmente por serem sinónimo de alegria, lar, bem-estar. À Mónica, Bruno, Carmo e António o meu agradecimento por tudo. Ao meu avô, com 84 anos por me dar o privilégio de aprender com ele e a alegria de me ver tornar em quem sou hoje. A uma estrelinha muito especial que me levou a seguir este caminho, e à qual devo a decisão de lutar por fazer ciência e a esperança constante que aquilo que possa descobrir irá, de alguma forma, impactar a vida de muitas pessoas.

Ao meu namorado, André, pelo tornado de stress que teve que aguentar nos últimos meses e pelo apoio e amor incondicional nos momentos difíceis. Por ser o primeiro a festejar todas as minhas pequenas vitórias, obrigada.

Por último, quero agradecer aos meus amigos por toda a amizade e partilha ao longo dos anos. E pedir desculpa por ter estado desaparecida para escrever esta dissertação. Quero salientar nestes agradecimentos alguns deles. Para começar, a minha Joana Nápoles que mesmo à distância com os muitos vídeos que me enviou, ajudou a que nunca me faltasse motivação. À minha melhor amiga, Adriana, que me apoio e aturou imenso ao longo dos anos e nunca deixou de estar presente neste percurso. À Catarina Rodrigues e à Daniela Araújo pela amizade, conversas profundas e pelo melhor grupo de sempre. Ao Miguel e a Sara agradeço pela paciência para me aturarem nas horas em que me tornei impossível devido ao stress. A Ana Sofia pela amizade e partilha científica que nos une, pela troca de outputs e pelas longas viagens de comboio. À Tânia Queirós e Miguel Paula quero agradecer a amizade e serem um exemplo de profissionais e pessoas, tenho muito orgulho em vocês. À Tânia Silva, a minha loira, que sempre fez esforços para compatibilizar o meu tempo livre com o dela, para que nunca faltasse tempo para um café, obrigada por após tantos anos continuares aqui. Beatriz Cardoso e André Calheiros, obrigada por me ensinarem a levar a vida de uma forma mais leve. Aos 3 meninos, Lamela, Miguel A. e Pedro Machado obrigada por todas as boas memórias, pelos passeios de carro quando estava a stressar e principalmente ao Miguel, obrigada pelas mensagens de 2 em 2 dias a pressionar-me para acabar a dissertação, parece que resultou. À Márcia Barbosa, por ser um exemplo de força e resiliência que admiro muito e ser sinónimo de família. Aos meus primos Manuela e Faria por todas as conversas interessantes sobre os mais variados tópicos.

Por fim e não menos importante, aos 3 seres humanos que tornaram a minha vida no Porto melhor, mais divertida e cheia de cor. Ana Stuve, Bernardo Pereira e Inês Coutinho chamar-vos de amigos é uma honra, conto convosco para mais jantares deliciosos com direito a fogo de artificio. Mas quando este faltar, não há nada melhor que o som das nossas gargalhadas. Obrigada por terem tornado o Porto um lugar ainda mais especial e tão cheio de boas memórias.

A todos que passaram pelo caminho e fizeram da minha vida um lugar mais feliz, e cheio de boas memórias, o meu muito obrigada.

ABSTRACT

Organ-on-a-chip (OoC) is a miniaturized advanced microfluid device that recapitulates important biological and physiologic parameters of 3D human tissue/organs. Despite recent advances, the *in loco* detection of biomarkers on OoC is still a challenge, mainly because of the low concentration of key biomarkers released by the minoritized organ models, the complex design of the biochips, and their broad applications, where standard integration of biosensors is hard to achieve.

Here, in this work, the solution envisioned aims to develop a porous MN patch capable to collect media, which will be further integrated into an OoC device (more precisely on the organ chambers) and use the media as biological fluid to analyze the released biomarkers in a multisensory system. Thus, we propose a novel array of porous MNs using polydimethylsiloxane (PDMS) as bulk material to be further incorporated into the advanced microfluidic device (OoC).

To produce porous PDMS MNs, three distinct casting materials were used (i.e., glucose, homogeneous silica nanoparticles, heterogeneous silica nanoparticles), followed by leaching processes to remove the casting material and produce pores. The leaching method for silica nanoparticles was achieved with NaOH, and for glucose, H_2O. Besides this difference, the process was similar to the sugar leaching method used for the glucose particles, although in the first case it includes a homogenization and evaporation stage of the silica material dispersed in ethanol.

In this study, the morphology, wettability, air permeability, swelling, porosity, surface chemistry, and mechanical characteristics of the produced MNs were investigated. Overall, by using the SEM images aided by ImageJ, it was observed that homogeneous silica particles showed a higher number of small and homogeneous pores with greater interconnectivity. On the other hand, glucose allows larger pores with almost no interconnectivity

between them. In the case of heterogeneous silica-PDMS, smaller pores are visible compared to the glucose samples, but the air permeability results were better using the homogeneous silica-PDMS at comparable concentrations. Air permeability was used to evaluate the porous network interconnectivity.

To enhance the mechanical properties of porous PDMS microneedles, a chemical treatment with hyaluronic acid (HA) solution was applied at a concentration of 2 mg/mL. Overall, it was concluded that HA enhances the strength of MNs. Other characterizations revealed that the wettability of MNs is also influenced by HA treatment.

To assess the wettability, the contact angle between water drops and the modified-PDMS surface was measured. The results before and after etching for every microneedle exhibit a hydrophobic behavior, after being immersed in HA, the behavior changes to hydrophilic. Interestingly, during the performance of contact angle measurements, samples with a higher concentration of homogeneous silica treated with NaOH, exhibit an electroosmotic flow effect. To better understand this phenomenon, the surface chemical composition of these samples was studied using Energy Dispersive Spectrometer (EDS). The result was that on MNs with electroosmotic action, the proportion of oxygen was greater than on the other MNs, indicating that hydroxyl (-OH) groups must be closely associated with the electroosmotic effect, possibly created by the NaOH etching process.

Overall, the results indicated that homogeneous Silica at 10% is the porogenic material with the most promising combined characteristics (i.e., a high percentage of pores, interconnectivity, wettability, and air permeability) to produce the porous PDMS MNs arrays, to be further integrated into the advanced microfluidic device to collect biological samples for monitoring of OoC.

RESUMO

Organ-on-a-chip (OoC) é um dispositivo de microfluídica avançado miniaturizado que recapitula importantes parâmetros biológicos e fisiológicos de tecidos/órgãos humanos em 3D. Apesar dos avanços recentes, a detecção de biomarcadores em OoC ainda é um desafio devido aos baixos níveis de biomarcadores libertados pelos mini órgãos e devido à complexidade dos *designs* e aplicações desses sistemas, onde a integração de biossensores é difícil de ser alcançada.

Aqui, neste trabalho, a solução idealizada visa desenvolver e integrar um dispositivo microfluídico integrado com um patch de microagulhas capaz de coletar líquido das câmaras de órgãos para posterior análise em um sistema multissensorial integrado. Assim, propomos uma nova matriz de microagulhas porosas usando polidimetilsiloxano (PDMS) como bulk material a ser incorporado no dispositivo microfluídico avançado (OoC).

Para produzir MNs de PDMS porosos, três materiais de fundição distintos foram usados (ou seja, glicose, nanopartículas de sílica homogéneas, nanopartículas de sílica heterogéneas), seguido por processos de etching para remover o material de fundição e produzir poros. . O método de etching para nanopartículas de sílica foi realizado com NaOH e para a glicose, H_2O. O processo foi semelhante ao método de etching do açúcar utilizado para as partículas de glicose e sílica, embora no caso das partículas de sílica inclua uma etapa de homogeneização em etanol e evaporação.

Neste estudo, a morfologia, molhabilidade, permeabilidade ao ar, swelling, porosidade e características mecânicas e químicas da superfície dos microagulhas produzidos foram investigados. Utilizando as imagens microscopia eletrónica de varrimento analizadas pelo ImageJ, observou-se que partículas homogéneas de sílica permitem atingir o maior número de poros pequenos e homogéneos com maior interconectividade. Por outro

lado, a glicose permite a obtenção de poros maiores, mas em menor número, quase sem interconectividade entre eles. No caso de sílica-PDMS heterogénea, poros menores são visíveis em comparação com as amostras de glicose, mas os resultados de permeabilidade ao ar foram melhores usando a sílica-PDMS homogénea em concentrações comparáveis. A permeabilidade ao ar foi usada para avaliar a interconectividade da rede porosa.

Para melhorar as propriedades mecânicas das microagulhas, porosas foi aplicado um banho da solução de ácido hialurónico na concentração de 2 mg/mL. No geral, concluiu-se que o ácido hialurónico aumenta a resistência das microagulhas. O comportamento hidrofóbico das microagulhas. Outra caraterização mostrou que a molhabilidade também é influenciada pelo ácido hialurónico.

O ângulo de contato entre as gotas de água e a superfície foi medido para avaliar a molhabilidade. Antes e depois do etching, cada microagulha apresenta um comportamento hidrofóbico; no entanto, após serem imersas em ácido hialurónico, o comportamento muda para hidrofílico. Curiosamente, durante a realização de medidas de ângulo de contato, amostras com maior concentração de sílica homogénea e tratadas com NaOH exibem um efeito de fluxo eletroosmótico. Para entender melhor este fenómeno, a composição química da superfície dessas amostras foi estuda usando Espectroscopia de raios x por Dispersão de Energia

O resultado mostrou que nas microagulhas com effeito eletroosmótico a proporção de oxigênio foi maior do que nas outras, indicando que os grupos hidroxilo (-OH) devem estar intimamente associados ao efeito eletroosmótico, possivelmente criado pelo processo de etching com NaOH.

No geral, os resultados indicaram que as microagulhas de PDMS-Sílica Homogénea 10% são a estratégia com mais caraterísticas promissoras (por exemplo: alta percentagem de pores conectados, molhabilidade, e permeabilidade ao ar) para produzir as microagulhas porosas de PDMS e integrar no dispositivo microfluídico avançado para coletar amostras biológicas para monitoramento de OoC.

LIST OF CONTENTS

LIST OF FIGURES

LIST OF TABLES

ABBREVIATIONS

2D Two-Dimensional

3D Three–Dimensional

CAD Computer-Aided Design

CK-MB Creatine kinase MB

DAB Droplet-born Air Blowing

DMA Dynamic Mechanical Analysis

DNA Deoxyribonucleic Acid

ECM Extracellular Matrix

EDS Energy Dispersive Spectrometer

HA Hyaluronic acid

HER-2 Human Epidermal growth factor receptor 2

iPSC Induced pluripotent stem cells

ISF Interstitial fluid

MNs Microneedles

MOoC Multi-Organ-on-a-chip

Ns Non-significant

OoC Organ-on-a-chip

Pa Pascal

PDMS Polydimethylsiloxane

PLGA Poly (lactic-co-glycolic acid)

PMMA Polymethylmethacrylate

ρPDMS PDMS density

ρWater Water density

RNA Ribonucleic acid

RT Room temperature

SD Standard deviation

SOoC Single-organ-on-a-chip

SEM Scanning Electron Microscopy

SPR Surface Plasmon Resonance

TEER Trans-Epithelial Electrical Resistance

W_f Final weight

W_i Initial weight

MOTIVATION AND GOALS

In the past few decades, new approaches to study and better mimic human organ models have emerged, such as the case of organ-on-a-chip (OoC) platforms, which emerged to substitute the gold standard techniques (i.e., static 2D cell culture and animal models) that are recognized for their lack of representativity. OoCs are advanced microfluidic devices containing miniaturized organ models that grow in dynamic *in vitro* conditions and enable the modeling of human physiology, function, and pathology. For the development of OoC models, a microfluidic chip designed to replicate the parameters of an organ-specific microenvironment is required. The spatial arrangements of cells, the existence of biomechanical stresses, and tissue characterization techniques, are all important factors that need to be considered.

Although this technology has only been recently developed (less than two decades ago), it is considered a hot topic technology due to its high potential to understand diseases or biological processes that remain unclear. Therefore, OoCs are an important technology tool to do basic research or even perform drug screenings to evaluate the best therapy for an individual patient (the so-called personalized medicine).

During the past years, the interest in the OoC field has grown and platforms had become more sophisticated. However, some limitations for their applicability at the preclinical stage are still a challenge that needs to be surpassed, as they generally lack real-time monitoring and sensing capabilities. These capabilities are essential to evaluate the metabolic behavior of the tissues/organs and the cellular surroundings that represent the *in vivo* physiology and the physical environment of the tissue constructs, which must be constantly monitored to evaluate the performance of OoCs.

At present, this gap is being bridged with the development of micro(bio)sensors that are meant to be integrated into OoC devices, allowing for real-time analysis of biological processes. Integration of (bio)sensors in OoC platforms is still a technological gap that needs to be fulfilled to achieve an end-use preclinical platform. Currently, the response of organ models to the analyzed parameters is post-analyzed off-line, which besides time-consuming, is prone to contamination and sample degradation, hampering their feasibility as a standard, autonomous and robust preclinical model for laboratory practice. To address this issue, this Master project, performed through a collaboration between the Faculty of Engineering, University of Porto (FEUP) and University of Minho (Engineering School, CMEMS), the creation of a microarray of porous microneedles that will serve to collect the feeding fluid for a multiplexed (bio)sensor system (in development within the CMEMS group), where important biomarkers can be continuously measured and monitored.

To achieve this goal, the project was divided into four main objectives, namely:

1) Design and fabricate a PMMA mold for the casting of PDMS MNs;
2) Design and optimize porous MNs developed in PDMS, using glucose and commercial silica nanoparticles to create the porous structure after the leaching method;
3) Coat the PDMS porous MNs with hyaluronic acid (HA) to overcome the possible low mechanical strength, improve biocompatibility and optimize the natural hydrophilicity behavior of PDMS.
4) Perform a full characterization of the developed porous PDMS MNs, namely mechanical, physicochemical, and hydrophilic behavior, among others.

1. INTRODUCTION

1.1 ORGAN-ON-A-CHIP PLATFORMS

Organ-on-a-chip (OoC) platforms are an *in vitro* technology that mimics tissue and micron organs while maintaining tissue/organ-level physiology and homeostasis. They are based on microfluidic devices with perfused micrometer-sized chambers that are fed by continuous cell culture media flowing from the organ models [1]. This continuous flow of cellular media allows the mimic of shear flow conditions and nutrient/gases exchanges, which keeps the cell culture alive for a longer period than the static *in vitro* cultures [2]. Therefore, OoC can reproduce key aspects of the complexity of organs and biosystems, by simulating microenvironments, interfaces, nutrient gradients, and circulation [3].

OoC can be classified as single-organ-on-a-chip (SOoC) or multiorgan-on-a-chip (MOoC), depending on the number of organ models that are comprised in the advanced microfluidic platform. The selection of the OoC is highly dependent on the goal of these advanced microfluidic devices. In literature, it can be found several studies where SOoC were developed to study single target organs, such as liver [4], heart [5], brain [6], kidneys [7], among others, and where the platform receives the corresponding name of the organ (such as liver-on-a-chip for liver modeling). These platforms are essential to acquire a deep knowledge of cell-cell and physiological interactions of an organ, by decoupling into their different cell/tissue components, while maintaining their physiological integrity. This is a great advantage of these platforms since neither the current gold standard technologies (i.e., 2D/3D static culture cells or animal models) are able to achieve it [8]. Moreover, researchers are also integrating more than one organ to establish crosstalk between them, resulting in MOoC platforms, which have a large potential to enable new basic biology inquiries and drug screening advances [9]. Communication between organs is essential to ensure the complexity of physiology and functionality. Although *in vivo* organs are separated, information and interactions, are mediated via the circulation system. As a result, integrative methodologies are crucial for developing physiological organ-organ interactions in OoC platforms. Individual organs are connected by microfluidic systems, simulating the *in vivo* role of vascular perfusion, and allowing control over the culture environment to mimic some elements of homeostasis. In fact, MOoC approaches are more in line with the body-on-a-chip philosophy, which is a target goal among the pharmaceutic, biomedical, and biotechnological industries.

However, human-on-chip technology (or body-on-a-chip) is still in its early stages, and various obstacles must be overcome to increase its physiological relevance and translation to the clinical stage, namely organs organ sizing, integration and interconnectivity, common feeding media for the different tissues, biomaterial improvement for the different tissues, real-time monitoring, among many other [3].

Despite these challenges to achieving the so desired human-on-a-chip, OoC technologies offer a wide range of applications, as depicted in Figure 1, including drug research, which is one of the main applications of OoC. The industry of new drugs is highly time-consuming and has big costs [10]. One of the main reasons for being so difficult to develop new medicines and put them on the market is the fact that drug candidates usually fail during clinical trials, due to the inherent differences between animal models (typically used to screen those new drugs) and humans. In fact, the standard *in vitro* experiments and animals used to evaluate the drug efficacy and toxicity assessments are associated with many uncertainties and side effects. Therefore, OoC can provide more complete and useful information compared with small mammal animals and static 2D/3D culture assays. Due to its construction, OoC platforms make it easier to detect drug toxicity, both anticipated and unexpected, on healthy and diseased organ models, as well as address biological questions. Another important issue that OoC can help medicine to evolve, is the fact that the bulk of drugs on the market do not produce the desired results in all patients, which can be either ineffective for some individuals or harmful to their health. Because OoC can be developed with patient primary human cells or stem-cell-derived cells (iPSC-derived cells), the OoC system has the potential to be designed as a model platform capable to mimic individual physiology and predicting optimized drug treatments, as previously referred to as personalized medicine [11].

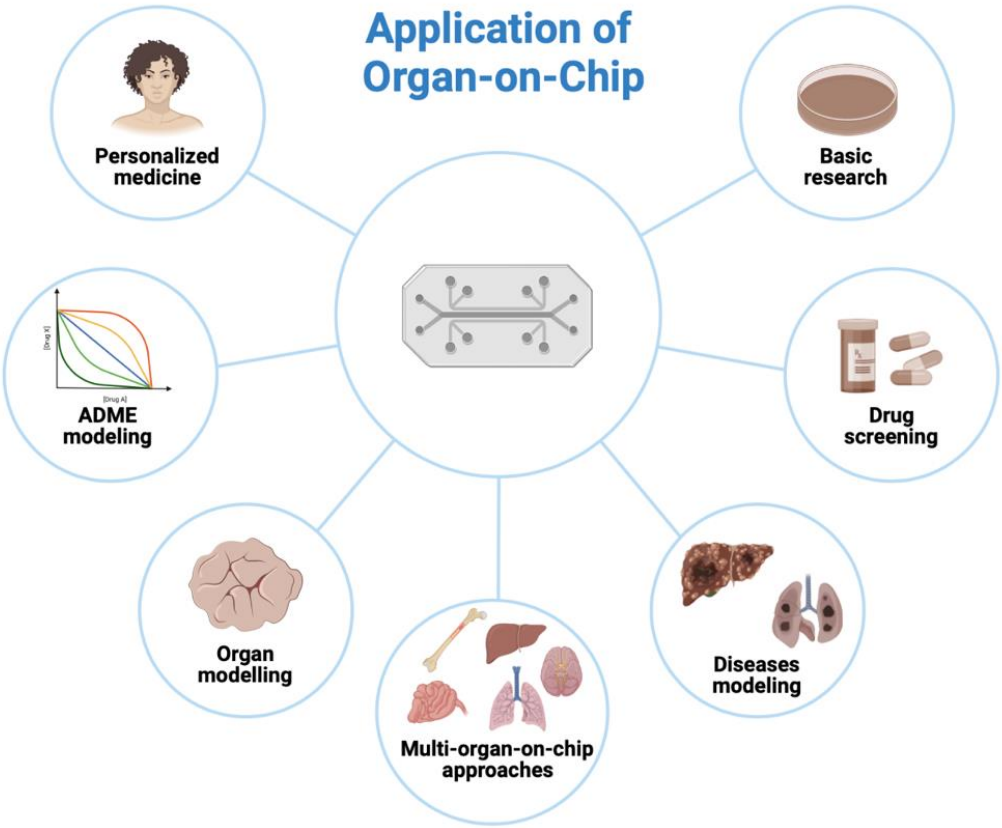

Figure 1: Representation of the possible applications of OoC from basic research to personalized medicine.

Therefore, this emerging technology has several advantages, including replacing and reducing animal use, being less time-consuming than using animals, personalized medicine, and replicating complicated physiologic body features. However, despite the enthusiasm and progress of OoC, important hurdles must be overcome to create a valid and robust preclinical model. As above stated, the design of the OoC platform must be appropriate for the study's purpose, but also its validation as an end-using device. For that, appropriate organ scaling, tissue vascularization, recapitulation of the immunological response, repeatability, organ monitoring, oxygenation, pH, shear rate, cell viability, and cell density, are some of the parameters that need to be considered when designing an OoC [8]. Among all these parameters, monitoring the OoC platforms is a huge step to guarantee reproducibility and appropriate chemical, physical, and cell analysis. Therefore, the fabrication and integration of biosensor modules into the advanced microfluidic platform has to be a future achievement from the end-user perspective. Focusing on this purpose, the next sub-chapters will be dedicated to a brief revision of the most important aspects related to microfabrication, microcirculation, and design strategies for the integration of biosensors to monitor organ models in OoC.

1.1.1 MICROFABRICATION AND MATERIALS

Microphysiological systems, or OoC, have been made possible thanks to advancements in microfluidics, microfabrication techniques, and tissue engineering. Among the fabrication materials, polydimethylsiloxane (PDMS), a silicon elastomer polymer, is the most used to make traditional microfluidic devices, because of its unique properties, such as flexibility, low interfacial free energy on its surface, optical transparency, chemical inert, good gas permeability, liquid impermeability, and good thermal stability, as well as its elastomeric properties that allows a quick, low cost and reproducible way to fabricate and prototype microfluidic devices by soft lithography [12], [13].

Additionally, PDMS is biocompatible and non-toxic to cells and blood, which made PDMS widely used to create OoC. On the other hand, using PDMS to culture cells have some disadvantages. Among these disadvantages, the natural PDMS hydrophobicity is pinpointed to affect the results of biochemical analysis, due to the adsorption of small biomolecules [14]. Cell adhesion to PDMS can also be an issue of its hydrophobicity, generally solved by coating the surface with hydrophilic biomolecules, such as proteins. However, this strategy is non-permanent due to the low surface energy of the PDMS [15]. To surpass this challenge, other strategies have been developed, such as a combination of PDMS with other materials to improve the functionality of OoC and complement the PDMS lacks.

For instance, Poly(methyl methacrylate) (PMMA) is another material widely used to fabricate OoC devices, such as skin-on-a-chip [16] (Figure 2A), or human blood vessels [17], Figure 2B, wherein represented. However, most of the time, this material is used to produce devices using a hybrid combination of PDMS and PMMA, as was the case of the study performed by Pitingolo et al., 2018, which investigates the potential of a colorectal-on-a-chip platform for cancer drug testing [18], Figure 2C.

Besides the physical structure of the device, in some cases to mimic the organ function, it is necessary to reconstitute a membrane or a physical division. In this case, the selection of the material has to consider parameters such as gas transfer, type of cell lines, and liquid permeability that better mimic the organ's physiology and function. Jang et al., 2013, described one of these organs: a kidney-on-a-chip platform, that was developed using molding and soft lithography to perform drug screening tests. In this OoC, the main channel was made with PDMS and a porous polyester membrane that was placed inside the channel to divide it into two regions, the apical luminal and basal interstitial [19]. In another study, performed by Hassell et al., 2017, a polyester membrane was also incorporated into a lung-on-a-chip device. In this case, to simulate the alveolar configuration [20]. Another example of fabrication with multimaterials is the gut-on-a-chip developed by Kulthong et al., 2020, which developed this OoC with three glass slides, a porous membrane of polyester, and a silicone gasket [21] (Figure 2D).

Engineering different strategies to create OoC and approximate the model to the *in vivo* function and structure is crucial. Thus, a wide range of new materials and techniques are being considered [22]. Although most devices are still made of PDMS, alternative materials such as soft materials (i.e., hydrogels) are being investigated. An example is the work of Vershusel et al., 2014 [23], which employed 3D bioprinting instead of soft lithography to produce an one-step production approach. Various hydrogels have been used for 3D bioprinting such as GelMA [24], gelatin [25], collagen I [22], fibrin [26], and alginate [27], among others [28]. But also, combinations of these materials can be used, for example, Kang et al., 2016, described a 3D bioprinting system to produce tissues with a mixture of gelatin, fibrinogen, HA, and glycerol [29]. These combination of materials serves to fulfill the extracellular requirements needed to emulate the extracellular matrix (ECM) of living organs, specially the mechanical strength and nutrient supplies.

Among the techniques to produce organ models, bioprinting has gained a position as a technique to create OoC models, because of its potential to print several materials and cell lines simultaneously with good spatial resolution and repeatability. It is an alternative to traditional techniques (e.g., spheroids), which enables researchers to develop artificial organotypic tissues with regulated cells and ECM distribution, and an extracellular microenvironment similar to what is seen *in vivo* [30].

Inkjet, laser, and pressure-based bioprinting are the three primary types of 3D bioprinting technologies, and they have emerged as one of the most advanced and practical advances in disease modeling and tissue engineering [30]. Since the 3D bioprinting development (Figure 2E), several organ models and structures were biofabricated, one of the most representative devices is the heart-on-a-chip [31].

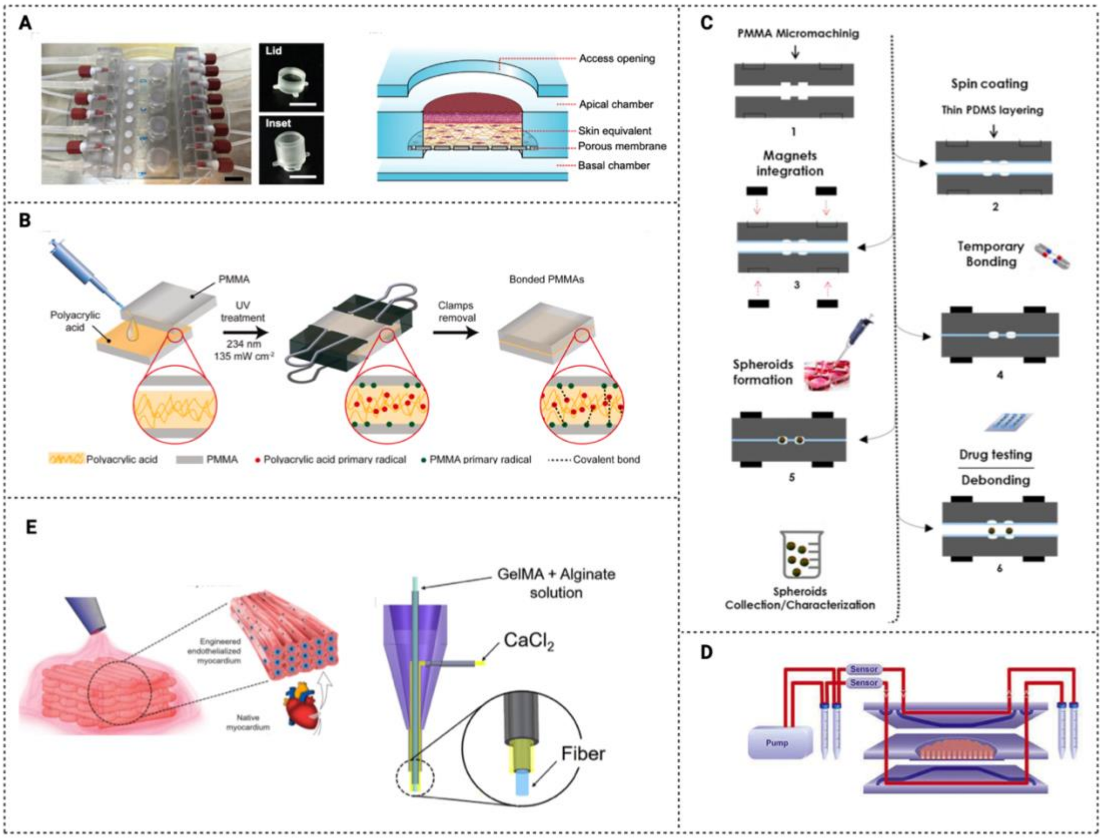

Figure 2: OoC devices and materials. **A** Skin-on-a-chip device adapted from [16], **B** OoC device to engineering vessels from [17], **C** Colorectal-on-a-chip device [18], **D** Gut-on-a-chip platform [21], **E** Bioprinting example of a heart-on-a-chip from [31].

OoC systems are created by integrating microfluidic technologies and tissue engineering in a single device to simulate physiological settings [32]. The microfluidics technologies englobing: parallel channels, multilayers technology, spinning microfluidic technologies [32], and the techniques to develop the biological part (biofabrication) such as bioprinting, cell patterning, paper-base, spheroids, and organoids (Figure 3).

Historically, the first advanced microfluidic device coined as OoC was derived from the work of Hub et al., 2010, which developed a lung-on-a-chip, using a multilayer approach to produce a tissue-tissue interface [33]. This new multilayer microfluidic technology concept opened the door for a new advanced bioplatform that considers the fluid stress and cyclic forces, which is vital for many organ functions and ideal to mimic tissue interfaces and barriers systems, such as the brain [34], kidney [35], and intestine [36].

Another strategy is to create parallel channels, which have been used to build OoC systems based on easy fabrication and operation settings. Furthermore, with this strategy, it is possible to control the concentration gradient of nutrients. For example, parallel designs were used to study metastasis from breast cancer to bone [37], and control oxygen in microfluidic devices [38]. Parallel channels are, in general, constructed with micropillars, microgrooves, or hydrogels to interconnect the channels. An example of this approach is the work of Ren and coworkers (2013), where is described a system with a micropillar array-aided tissue interface mimicking a microfluidic device for the dynamic study of hypoxia-induced myocardial injury in a microenvironment-controllable manner [39].

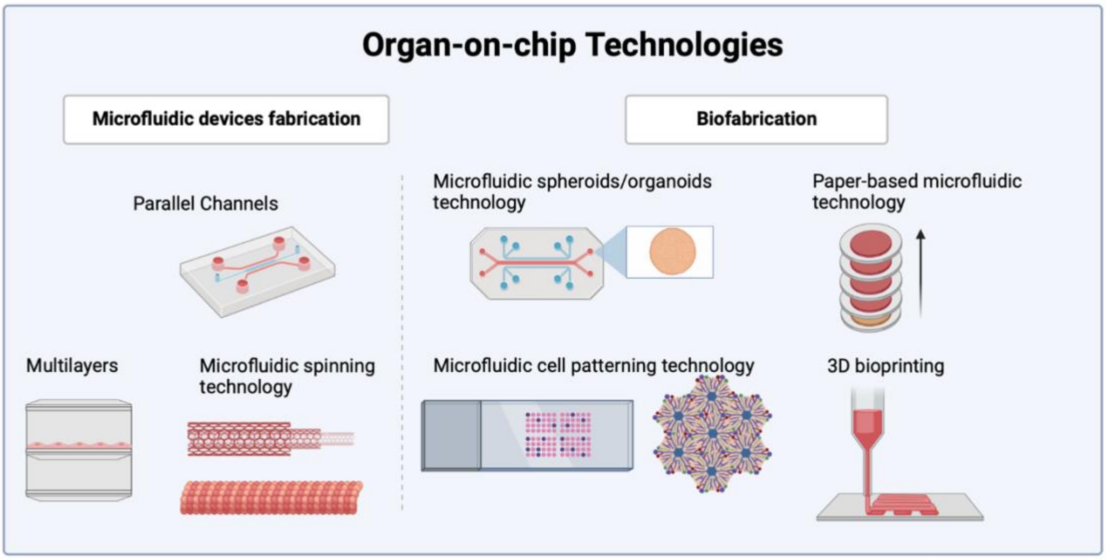

Figure 3: OoC technologies for the construction of OoC platforms.

In general, the construction of MOoC platforms consists of the coupling of single OoC devices, each simulating a different organ, via capillary connection [40], [41], [42], another strategy to build MOoC is the integration of different organ models in a single plate [43], [44] (Figure 4).

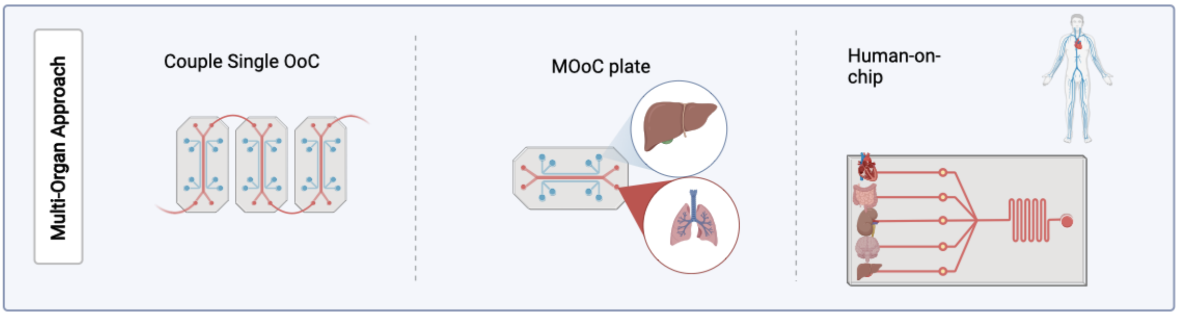

Figure 4: MOoC technologies.

1.1.2. MICROFLUIDIC SYSTEMS

As already mentioned, tissues and multicellular structures in living organs are subjected to a variety of interfacial mechanical forces, including blood flow, compression, and tension, which have been identified as important factors in a wide range of physiological processes by [45]. The precise control of flow permits accurate models of the living organ to be built at the microscale. Mechanical stimuli commonly applied in OoC systems can be classified into three categories: shear flow (laminar, pulsatile, and interstitial), compression, and stretch/strain [46]. Since flow induces shear stress, which generates gene expression, cellular morphology, and cell polarity [47], it is important to consider the type of flow and its impact on the OoC system.

Non-dynamic organ chambers are a strategy in which connections between organs rely on physical proximity instead of connective flow. The circulation works through diffusion forces. In the alternative, the dynamic flow runs medium, which can be perfused in one way, or it can be recirculated (Figure 5). In this case, flow is generated using a driving force, such as a pump. But the aid of external pumps has more probability of the formation of bubbles, which can be solved by using a bubble trap in the microfluidic device. Also, external pumps required more tubing, and it can lead to leakage that can create uncontrolled conditions [48]. Ideally, the circulation system should be created without external pumps, thus, reducing the complexity of connections and tubing [49]. Aiming for this solution, a pumpless and tubeless system was described by Delon et al., 2020. This system is based on the use of hydrophilic thread to provide a driving force for perfusion through constant evaporation in the controlled conditions of a cell incubator [50].

In the case of connected single OoC units and integrated MOoC, platforms can reproduce one-way communication from organ A to organ B (Figure 5A-B) or two-way communication (recirculation) between organ A and organ B (Figure 5C-E). Organ systems can be designed to arrange the individual chambers in serial, parallel, or both. One way circulation enables crosstalk to organs located downstream, is since the direction of flow eliminates upstream communication. While, recirculation systems, allow interconnect organs and evaluate both the upstream and downstream communication [10].

Incorporating suitable physiologically accurate biomechanical stimuli into OoC models is challenging. The type of organs, analysis, and the questions to be addressed influence the choice of the circulation system, where the dynamics of flow, shear stress, and concentration gradients must be considered [51]. One of the engineering challenges is the need to incorporate detection and analysis methods into the microfluidic device. Monitoring of OoC is required to develop a better understanding of which circulation system is ideal and understand physiological processes in real time. On the other hand, real-time information can feed algorithms for evaluating drug responses over extended periods, biological responses, and tumor metastasis. For that, the integration of sensors is required.

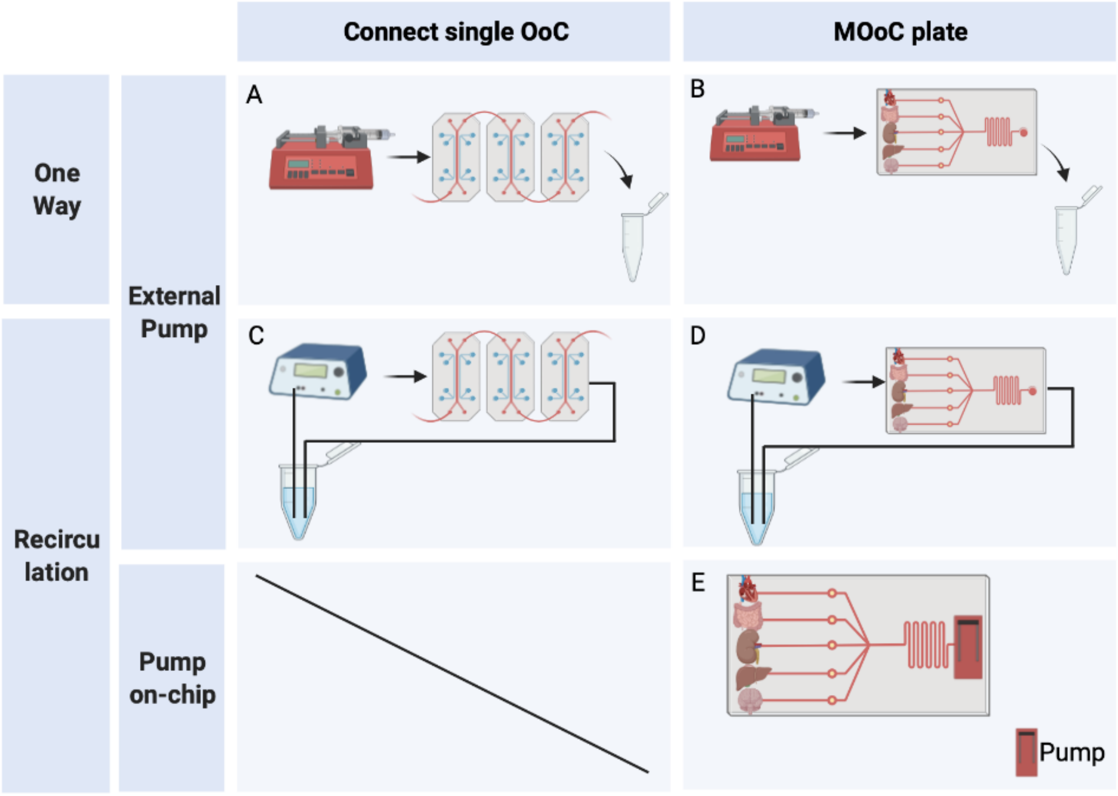

Figure 5: Circulation systems typically observed in SOoC and MOoC devices.

1.2 MONITORING OF OOC

As abovementioned, monitoring OoC is a challenging task, that is in general based on laborious and time-consuming techniques, such as microscopy techniques (confocal, for example), and/or analytical techniques (ELISA tests, biomolecular, genomics, among others) to assess and characterize the viability and homeostasis of the organ models. In addition, these methods commonly require that the organ model has to be sacrificed, needs several time points, and demands to stop the circulation of the system, which contribute to possible contamination and disturbance of the normal cell activity and increases the probability of biased results. Therefore, it is crucial the development of a better method to evaluate the performance of OoC. Biosensors (box 1) integrated with OoCs are a promising alternative for monitoring and characterizing the OoC, with the advantages of being less invasive and allowing continuous, real-time, and long-term analysis. Also, it has the advantage to reduce volumes and distances in the microfluidic platform, making the biorecognition of molecules easier.

In the past decade, several (bio)sensors' methodologies have been developed to monitor OoC such as pH [52], barrier integrity [53], temperature [54], oxygen, [55], and response to electrical [56], mechanical [57], and cells drug response [58].

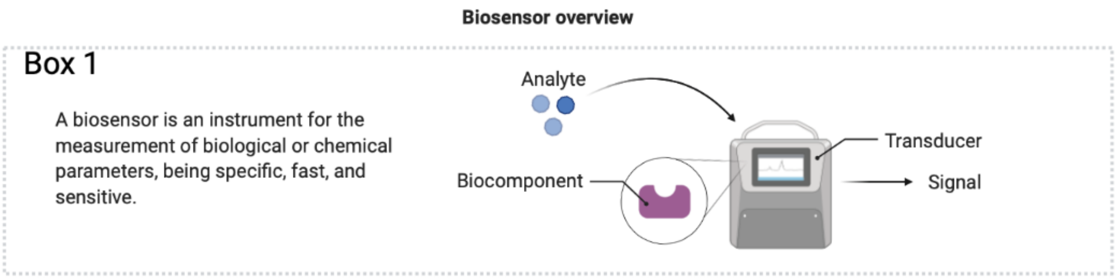
Biosensor overview

Box 1

A biosensor is an instrument for the measurement of biological or chemical parameters, being specific, fast, and sensitive.

Despite all of the efforts to incorporate biosensors into OoC platforms, this field is just getting started [59]. Advantaging, biosensors have a low detection limit, high selectivity, responsiveness, and required less analysis time than standard methodologies [60]. Proteins, biochemical signals, and other molecules released from cells provide essential information about the viability, functionality, possible immune response, cell-cell signaling, and new molecular pathways of the organ [61]. A predictable and repeatable cell culture environment is maintained by continuously evaluating all of these factors in real time. Because OoC can be designed with different biomodels and for diverse applications, biosensors must be adapted for the designed application. Overall, the biosensor system, integrated into the OoC, should be able to monitor multi-parameters, such as cell behavior, physicochemical gradients, and stimulations (electrical and mechanical), to provide complete information about OoC performance.

Electrochemical (EC) and optical sensors are the common types of (bio)sensors developed for OoC integrated platforms.

Electrochemical sensors can use amperometry, enzymatic, impedance spectroscopy, and transepithelial/transendothelial electrical resistance

(TEER) [60]. Amperometry and voltammetry biosensors detect the fluctuation of free electrons, which can be applied to measure oxygen reactions. Enzymatic has a similar principle, but it detects metabolites, such as lactate and glucose [62]. Impedance spectroscopy is very useful to detect biomolecules. This type of biosensor uses aptamers or antibodies to identify specific biomarkers. For instance, this technique was used to evaluate a MOoC breast cancer-heart platform [63]. On the other hand, TEER is widely used to evaluate the integrity of biological barriers such as brain-blood-barrier, endothelial and epithelial barriers, Figure 6A [53]. Evaluation of biomolecular parameters of multiorgan models is more difficult to achieve. However, a study by Lee et al., (2021), has shown the application of EC impedance spectroscopy in a Heart and breast-on-a-chip, to measure multi-biomarkers, such as. Troponin T, CK-MB, HER-2, Figure 6B [63]. Also, other studies have shown the use of amperometry to measure biomarkers released in a muscle-on-a-chip platform that evaluates Tumor Necrosis Factor-α (TNF-α) and Interleukin-6 (IL6), Figure 6C [64]. An example of an enzymatic-based biosensor is given in Figure 6D [65], which was developed to measure glucose and lactate on a colon-on-a-chip device.

Optical sensors use colorimetry and surface plasmon resonance (SPR) [60]. Optical (bio)sensors use light absorption, reflectance, fluorescence, and luminescence to monitor chemical and biological processes. An advantage of the optical (bio)sensors, both colorimetric and SPR, is the possibility to be integrated into an OoC and perform simultaneous detection of multiple analytes [66], [67]. Some examples of these sensors applied to OoC are a microfluidic optical platform for real-time monitoring of pH and oxygen using light absorbed and luminescence, respectively, Figure 6F [52]. Particularly, the study of Khalid et al., 2020, describes a pH optical sensor based on the light intensity that was integrated into a lung-cancer-on-a-chip device [58], Figure 6E.

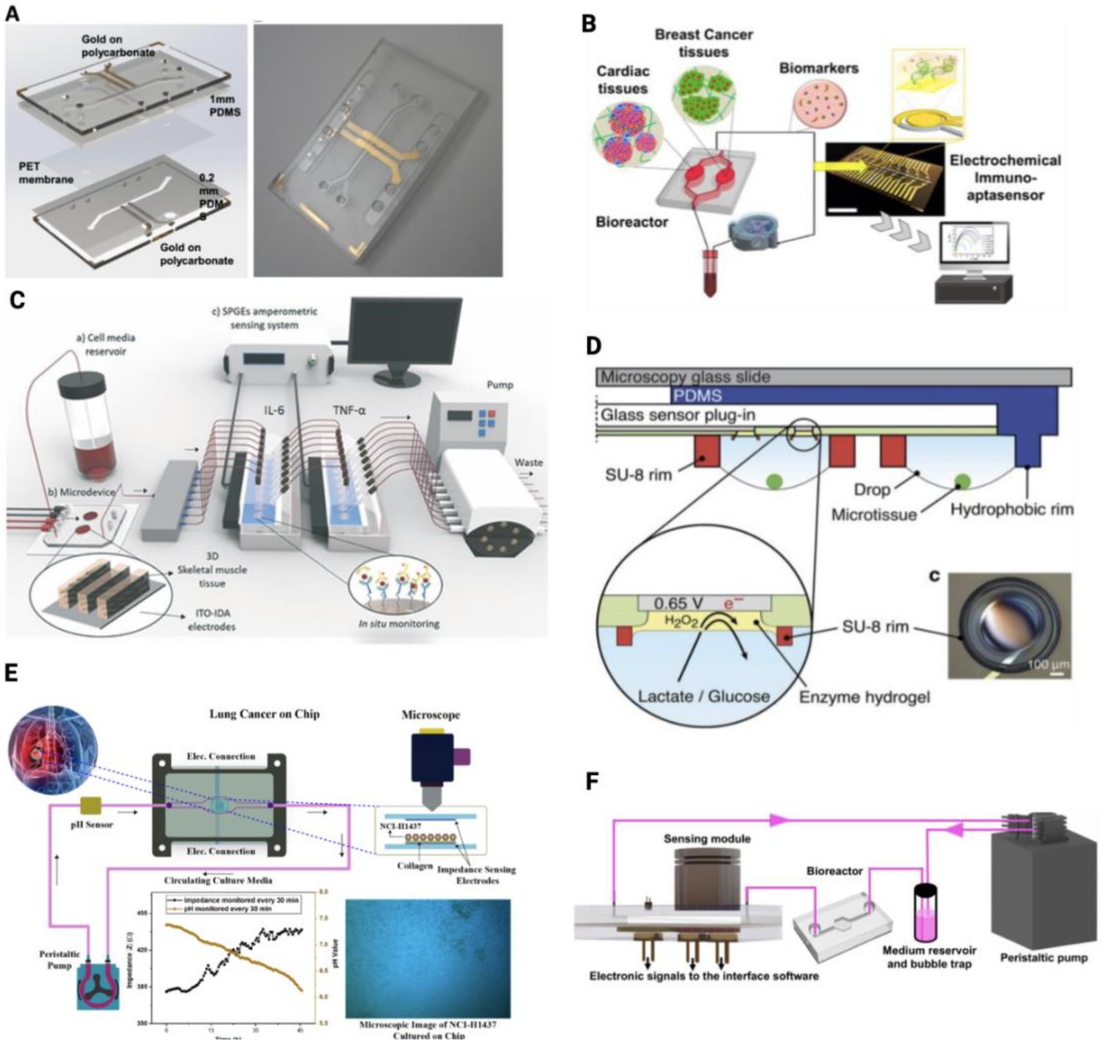

Figure 6: Integrated biosensors in OoC devices. **A** TEER-based biosensor on brain-on-a-chip [53]**, B** EC-based biosensor on a heart-breast-cancer-on-a-chip [63], **C** Amperometry sensing system for muscle-on-a-chip [64], **D** Colon-on-a-chip device with enzymatic biosensor [65], **E** Lung-on-a-chip with pH optical sensor [58], **F** Microfluidic platform to evaluate oxygen and pH through optical sensor [52].

Physical parameters are also important parameters that should be monitored to guarantee similar conditions between studies. pH, temperature, shear stress, flow rate, mechanical strain, humidity, and osmolarity, are some of the physical parameters studied and monitored in OoC.

To accomplish a robust and end-use OoC platform, it is envisioned that a single multisensory platform is needed to accomplish physical and biological sensing operations at once. For that, researchers have been working on integrating more than one type of sensor into the same platform. Khalid et al., 2020, described a lung-on-a-chip platform with optical, TEER, and pH sensors for physiological monitoring and toxicity assessment [58]. Zhang et al., 2017, developed a MOoC device connected with an automatic multisensing module with optical, and electrochemical sensors for organ monitoring [48]. Until now, this last work still is considered the reference for the most completed platforms for OoC monitoring, although the integration between the sensing platform within the microfluidic platform was not fully achieved.

Overall, a multisensory platform is expected to enhance the way for automated, and high-performance *in situ* monitoring. Although these biosensors offer various advantages, making them compact enough to be integrated is a challenge. Besides the fabrication challenge, the assessment of OoC requires real-time and continuous monitoring, which is an issue for electrochemical biosensors, due to the sensor saturation and regeneration. For this reason, optical sensors are in general preferred. Recently, 3D printing has emerged as a technique that can simplify the integration of biosensors into OoC [68], by allowing the direct printing of sensors into the OoC device during fabrication.

Overall, to accomplish the requirements for the sensing integration, some technological improvements are still needed to be achieved, in order to meet the high degree of complexity and engineering. A strategy to simplify these modulations is based on the split of some of the feeding media from the OoC chamber and driving it into the biosensor module system. For this purpose, a physical mechanism has to be integrated into the perfusion biochamber to collect the fluid. With this strategy in mind, the solution envisioned in this master project is to design, fabricate and optimize PDMS porous microneedles, which will be further inserted into the biochamber to directly collect the feeding media and redirect it into the biosensing system for biomarkers analysis.

1.3 Microneedles

Microneedles (MNs) are a biomedical technology with the ability to access biological information with minimal invasion by micrometer-scale downsizing a single or an array of needles, which is in general used as a strategy to deliver drugs [69], or biomolecules such as proteins [70], RNA, DNA [71] into cells, with temporal and spatial precision [72].

The dimensions of MNs may vary depending on the application. The most common dimensions find in literature have height ranges between 150 to 1500 μm, with a base width of 50 to 250 μm and a tip diameter of 1 to 25 μm [73]. In terms of shape, needle tips come in a variety of shapes, including triangular, cylindrical, and pentagonal [74]. MNs design and size have been identified as the primer characteristic to be modified for optimal performance of the MNs system. To maximize efficiency, the length of the MN can be customized to achieve a desired depth of penetration.

The shape, the number of needles in the array, the height, the aspect ratio (the ratio of the base to the height of the needle), the material, and the thickness of the backing block, are all criteria that define MN design. Also, the volume that can be collected and loaded by the patch is determined by these criteria. The volume, in turn, contributes to determining the type of MN that best suits the desired application [75]. The design of the MNs device is crucial for the efficient performance of the system and different materials can be used in MNs fabrication.

MNs, which were first designed as a painless alternative to a hypodermic needle, have since then been investigated for many other biomedical applications. For instance, MNs have emerged as a tool to interact with the cell's environment with minimal invasion and with the potential to be used as a direct platform to sense the biological system. Intracellular, MNs can be used to detect the electrical activity of complex excitable networks, as well as the concentration, function, and interaction of biomolecules *in situ* [76].

For OoC, MNs can be combined with biosensors to continuously measure biomarkers that are released by the organ models. Therefore, the development of biocompatible MNs can provide access to the inner and outer environment of the biomodel and collect the medium for analysis without disturbing their biological function and structure. Their ability to interact with cells to extract fluid has been already demonstrated by MNs patches, successfully used to extract skin interstitial fluid (ISF) [77].

In this way, MNs can solve the technological challenge to integrate a biosensor system into an OoC platform, by avoiding the disturbance of the organ models and, at the same time, simplifying their engineering complexity for integration.

Due to the numerous nanostructures and variety of strategies for the delivery of drugs, MNs can be divided into traditional needles (solid, coated, or hollow) or emerged needles (dissolving, hydrogel-forming) [78]. Figure 7 represents these six approaches. Concerning the type of material used, MNs can be divided into degradable and non-degradable, and polymeric and non-polymeric materials, such as metal, silicon, ceramic, and carbon, among others [79]. Traditional solid MNs are commonly developed from metal or other rigid material [80].

Traditional coated MNs consist of a base of solid MNs containing drugs or other molecules absorbed on their surface (solutions or dispersions). Several techniques were developed to coat the surface such as spray coating and dip coating, but this strategy typically loses efficiency over time and requires high temperatures [81]. Another problem is the limited surface area that is available [82].

Hollow MNs have an empty cavity inside each needle, a bore on the tip, and a pressure-driven flow through the needle. Compared with the solid, coated, hollow MNs can load higher quantities of drugs or fluids. Several materials and methods are used to produce hollow MNs such as silicon, metals, ceramics, carbon, and others. The disadvantage of hollow MNs is that require an external pump device or application of pressure to collect fluid or release drugs from the cavity [83].

Dissolving MNs are easy to manufacture and use, due to being made with biodegradable materials, such as polymers and compounds that can be loaded with therapeutic agents. After being applied and in contact with a watery environment, MNs dissolve [84].

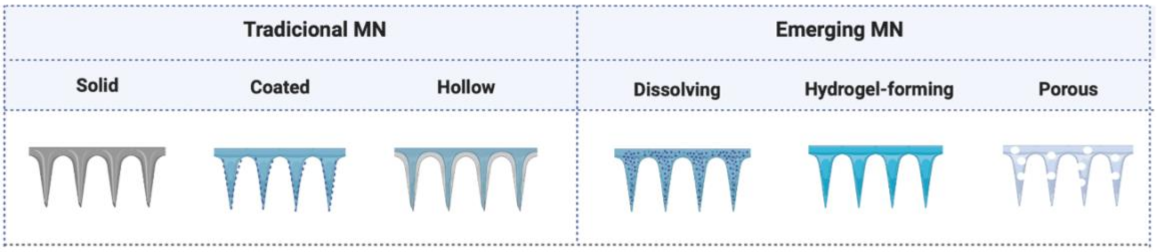

Figure 7: Traditional and emerging MNs approaches.

Hydrogel-forming MNs have been considered a separate group of MNs. The technique to produce hydrogel-forming MNs uses swelling polymers to dissolve the substance after MNs placement, which represents a bio-responsive system. The MNs, for instance, enable the disruption of the skin upon implantation. When the polymers come into touch with interstitial fluid, they expand and open the channels. This method enables a controlled rate of medication release. The overall structure of the MNs is preserved after the device is removed [85].

Recently, porous MNs have been developed and described as a new approach by Maaden et al., [86] due to being a more recent technique. Since this last MNs approach is the one selected to be developed in this work, a separated sub-chapter will be further presented (please see sub-chapter 1.3.2.).

1.3.1 MICRONEEDLES FABRICATION

Concerning the fabrication methods, several have been described in the literature, but the most commonly used are micro-molding, microelectromechanical systems (e.g., lithography, laser, etching), additive manufacturing (i.e., 3D printing), and layer-by-layer assembly [87].

Micro-molding is used to fabricate various polymeric MNs using cutting tools to sculpt the mold. Then, the polymeric material that makes up the MN is poured into the micro-mold in a liquid or semi-liquid state and then solidified to achieve the desired shape. It is a simple, low-cost, versatile process with high-resolution [88].

Microelectromechanical systems are divided into three main processes: deposition, patterning, and etching. Deposition includes film formation by physical vapor deposition or chemical vapor deposition. The patterning technique shapes the desired geometry on a film, substrate, or wafer. Lithography is a common technique used for patterning which consists in transferring the mask into a coated photosensitive film using light to develop the exposed photoresist. MNs microfabrication with lithography allows the production of smaller feature sizes but is considered a more complex process [89]. Etching is a technique that involves removing the unprotected sections of the substrate with a strong caustic chemical to create a microneedle design of interest. A wet and dry etching technique can be used, but a higher amount of chemicals is required [90]. Laser ablation and laser cutting were also reported to be used to fabricate metal and polymeric MNs. Laser ablation removes material from a solid surface by irradiating it with a laser beam [91]. Laser cutting uses an infra-red laser to cut metallic sheets in the shape of MNs [92]. Both techniques are simple, quick, and precise, with no contaminations, but required higher power consumption.

Other techniques are reported in the literature, such as Droplet-born Air Blowing (DAB). The DAB approach allows for delicate manufacturing conditions without the need for UV irradiation or heat since the polymer droplet is molded to the microneedle by air blowing. Furthermore, using a single polymer drop per MN allows for direct droplet size and concentration control. This technique can be combined with drug loads, resulting in drug loading with little drug losses [93].

Other processes have emerged depending on the type of MNs. For example, coated MNs used dip coating and spraying approaches. More recently, 3D printing emerged as a process to produce MNs. The MNs are designed using the CAD model, then the material is deposited, or solidified under specific conditions to create it [94].

1.3.2 POROUS MICRONEEDLES

Porous MNs have great potential due to the 3D porous structure and high surface area caused by their porosity. Therefore, porous MNs are a promising type to access information through OoC platforms and be used as a tool for aid biosensing. To overcome the gap between extracting interstitial fluid and further analysis, some authors described solutions that incorporate the biosensor on the patch of porous MNs [95]. For example, Kusama et al. 2021, described a porous microneedles patch combined with anodes and cathodes for efficient drug delivery (penetration) and analysis (extraction) [96]. Although the potential of porous MN and the several types of MNs have been thoroughly described in the literature, porous MN arrays are one of those that received less attention. One of the reasons behind this lack of interest can be the usual loss of material strength and the common laborious and time-consuming fabrication steps.

Thus, the purpose of this master project's is to overcome these identified problems, mainly the integration of biosensors in the vicinity of the organ models, turning the analysis process as simple as possible. By so, the chosen approach relies on the employment of porous MNs to remove fluid/media from the organ model chambers and deliver it to the biosensor system via microfluidic channels. For that, a simple and reproducible fabrication technique based on cast/removal of nano- or microscale materials into PDMS will be investigated.

Porous MNs have a substantial percentage of randomly distributed pores, making them attractive for quick wetting inside the MN body. Absorption of the interstitial fluid can occur via capillary forces of the pores, where the interconnecting porous enables the swelling of the fluid by the MNs [97]. However, they are in general intrinsically fragile due to the vast volume of the porous [97]. Strengthening the mechanical properties of the porous MNs material without compromising sample rating and volume is, therefore, a goal of this project.

Current methods for producing porous polymer MNs are complicated and only applicable to limited types of materials. In a review done by Bao et al., 2022, [98], electrochemical anodization, wet etching, mild micro-molding, sintering process, porogen leaching [99], hot embossing [100], phase separation, and emulsion and bolding were described as the main fabrication processes to achieve porous MNs. However, several limitations were described such as the porosity created, which is relatively low, and a large portion of the pores are not interconnected, limiting them from actively transporting molecules and fluids [101]. Also, this work reported that the vast majority of MNs were created through casting micro-molding techniques, using a prefabricated mold to obtain the porous MNs after casting and leaching soluble materials on them. This is one of the simplest approaches to obtaining porous MNs and thus, allowing mass production economically and simply.

Recently, polymer-based porous MNs were described using polymers such as polylactic-co-glycolic acid (PLGA) [100] and PDMS [99]. PDMS is widely used in various scientific fields such as microfluidic, medicine, energy, optics, electronics, mechanical, and others. As abovementioned, the versatile applications of PDMS are due to its favorable properties such as good elastic, transparent, biocompatible, gas-permeable, hydrophobic, and easy-to-surface modifications [102]. Due to its unique properties, this material was selected in this master project as the material to develop biocompatible porous microneedles. Additionally, PDMS allows easy bonding to other materials, such as glass or other PDMS structures, permanently or temporarily, depending on the bonding process selected, which is desirable for the application that is been foreseen. Therefore, the next sub-chapter will be focused on the strategies to create porous PDMS structures, such as MNs.

1.4 POROUS PDMS STRUCTURES

In this chapter, current fabrication methods for porous PDMS structures, as well as porous PDMS MNs are described. Porous PDMS fabrication techniques have been reported in the literature as direct templating, emulsion templating, gas foaming, phase separation, and 3D printing [103].

Direct templating involves the use of porogens in the form of solid templates that may be selectively dissolved or removed to leave a PDMS skeleton with interconnecting cavities. This technique requires sacrificial templates, such as sugar [104], [105], salt [106], nanomaterials [107], nickel foam [108], and other particles. This technique is also called as leaching method, and it is represented in Figure 8. Among all the techniques to produce porous PDMS structures, the particle/porogen leaching method is the most used, due to its low cost and ease of fabrication, where water or other solution can be used to dissolve soluble materials. However, the time for the leaching process is relatively long and after the porogen has been removed, functionalization with suitable materials is required to maintain sufficient mechanical strength [109]. For example, Lin et al., 2022, used the leaching method to create a 3D interconnected nanosheet of boron nitride in a PDMS matrix. In this work, sucrose particles were used as a sacrificial template where a mechanical stir was used to uniformly disperse the particles, followed by deionized water as a dissolving agent [104]. In another work, Nikpour et al., 2022, described a different technique to produce PDMS sponges loaded with curcumin. The citric acid in a solid state was directly added into the PDMS as a porogen material and after being cured was removed with hot ethanol [107]. Yung et al., 2019, presented an elastic and wearable piezoresistive strain sensor based on a 3D micro-porous graphene-coated PDMS sponge suitable for being attached to human skin, using a sugar cube as a sacrificial template [110].

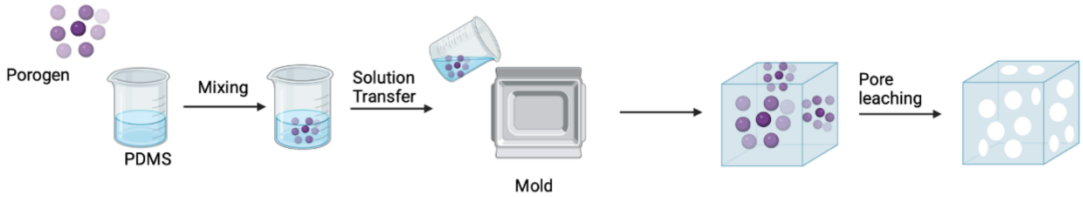

Figure 8: Schematic illustration of the leaching/porogen method to create PDMS porous MNs.

The emulsion has also been utilized to prepare hierarchically porous materials, as a soft templating method. Emulsion templating consists of polymerizing the continuous phase of an emulsion and using the emulsion droplets as pore templates. An emulsion can be formed by dispersing water droplets in an oil phase, known as a water-in-oil emulsion, or dispersing oil droplets in water. Monomer polymerization and subsequent removal of the droplet phase results in the formation of a porous polymer, usually, removing the droplet phase by evaporation [111]. Figure 9 illustrates the emulsion technique. Understanding and controlling the stability of the liquid emulsion template, such as droplet coalescence, is critical for achieving the appropriate porosity structures. As replicas of monodisperse emulsion droplets, this approach can produce both interconnected and isolated pores with a narrow pore size distribution. The product can also be simply scaled up. A disadvantage of this method is the surfactant used, which remains in the polymer and influences its performance and qualities after synthesis. Thus, in general, the surfactant must also be removed, which is laborious and time-consuming [112]. Thurgood et al., 2017, described the fabrication of a PDMS sponge by emulsion technique on a microfluidic system [113]. The microfluidic system generates water droplets into uncured PDMS using a T-junction structure. After a slow cure of the PDMS composite, the sponge is squeezed to retire the water droplets trapped in it.

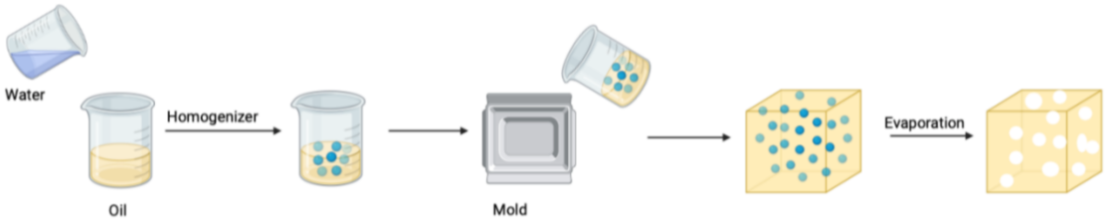

Figure 9: Schematic illustration of the emulsion templating to create PDMS porous MNs.

Gas foaming is another technique well-used to fabricate polymer foams. For example, Wang et al., 2020, described a fabrication technique inspired by gas-foaming to produce Cu_7S_4-MoS_2-Au nanoparticles in porous PDMS matrix [114]. The concept relies on the fact that when a polymer is plasticized by saturation in a supercritical fluid it is rapidly depressurized at a constant temperature, leading to the formation of polymer foams (cf. Figure 10). Then, pockets of gas nucleate and expand in the polymer, while pressure is removed. The procedure is simple and cost-effective. However, a drawback of this approach is the difficulty in managing the size and interconnectivity of the pores [115].

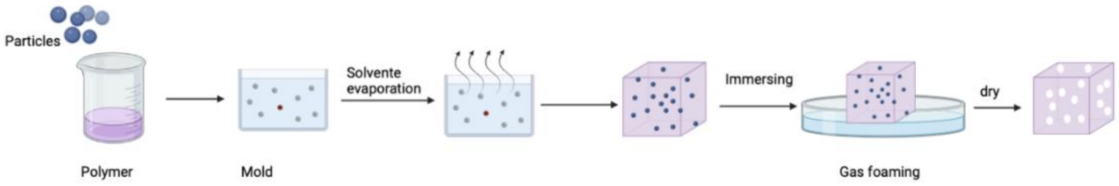

Figure 10: Schematic illustration of the gas foaming technique to create PDMS porous MNs.

Phase separation via the hydrolysis and condensation of inorganic precursors in the aqueous domain of a microphase-separated medium is a straightforward method for synthesizing porous monoliths. Thermally-induced phase separation, nonsolvent-induced phase separation, vapor-induced phase separation, and solvent evaporation-induced phase separation, are all methodologies for producing porous materials via phase separation technologies [103]. Abshirini et al., 2021, described the use of toluene and tetrahydrofuran as solvents for inducing two-step phase separation, and deionized water was used as a non-solvent phase [116]. In this work, the process used is a thermally induced phase separation. The first step consists of the preparation for phase separation at 50 °C. Then, in the second step, the temperature is raised to evaporate tetrahydrofuran and due to nucleation and growth, droplets of water are formed into the polymer phase. Afterward, three additional steps progressively raise the temperature, first to ensure all tetrahydrofuran is evaporated, then to evaporate toluene and create a second phase separation, and lastly to remove the water droplets.

Advances in additive manufacturing have received great attention during the last few years. It has the potential to generate porous substrates with various pore sizes, porosity rates, and patterns, as well as the construction of a 3D gradient with a porous appearance. For example, Pere et al., 2018, described a process to fabricate 3D printed patches, featuring MN with cone and pyramid geometries [94]. However, due to the low elastic modulus of the liquid prepolymer, direct 3D printing of PDMS to construct complicated structures is still challenging. At the moment, this procedure is slow and complex. As a result, significant upscaling is not an option and further studies are needed to improve its precision, economic viability, and reliability [103].

Based on the fabrication characteristics described above, the particle leaching method was selected to produce the porous PDMS MNs, since the pore size and porosity can be easily controlled via the selection of the casting particle size and the mixing ratio of the PDMS and particles in use. Therefore, particle size will depend on the selected material, and it is expected that increasing the concentration of particles in the PDMS substrate will lead to a higher density of interconnected pores. On the other hand, the mechanical resistance of the MNs is expected to decrease [117], which can be improved by further functionalization with strengthening molecules (such as HA). Some other factors with a direct impact on the porous structures are temperature, porogenity of the casting material, crosslink monomer, polymerization time, and chemistry of the surface. Exploring all these parameters during fabrication is very important to achieve the optimal material for the envisioned application. Therefore, a full characterization (i.e., mechanical, optical, and physicochemical) of the developed porous PDMS MNs is required.

2. MATERIAL AND METHODS

2.1. FABRICATION OF THE MOLD FOR A MICRONEEDLE ARRAY

A simple strategy to fabricate porous MNs capable of extracting medium in OoC can be achieved by combining PDMS molding with particle incorporation/leaching procedures. For that, the mold of the MN array was firstly designed using CAD software, and secondly fabricated by using a laser beam light (Miracle lasergravyrmaskin equipment) on PMMA, which served as the mold material for the MN ablated with the laser. The parameters used to produce the master mold of MNs are listed in Table 1, and an illustration of the PMMA master mold is shown in Figure 11.

Table 1: Parameter of the laser equipment used to produce the PMMA MNs mold

Parameter	Value
Intensity	10 mA
Cutting speed	5 mm/s

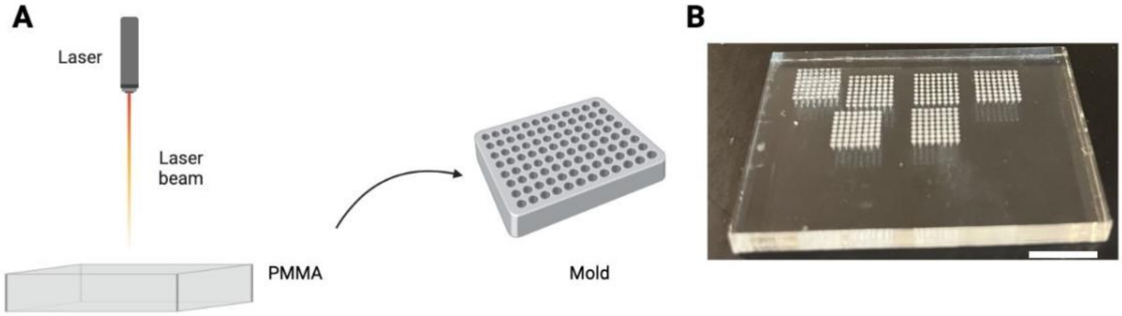

Figure 11: A: Representation of the fabrication step of the mold of MN array using a laser beam. **B:** PMMA Mold. Scale bar corresponding to 10 mm.

Afterward, the PMMA mold served as a mask to fabricate the PDMS MNs microarrays. Briefly, SYLGARD 184 elastomer kit (base elastomer and curing agent) was used to produce PDMS. To create porosity, different concentrations of organic and inorganic materials, namely glucose and silica nanoparticles, were mixed with PDMS prepolymer prepared by mixing the elastomer and curing agent at a mass ratio of 10:1 (w/w). After degassing in a vacuum system to remove bubbles, PDMS was poured into the PMMA mold and placed in an oven at 80 ˚C for 30 min. The cured PDMS MNs were then carefully peeled off from the PMMA molds. The casted compounds were removed by etching and subsequently dried with absorbent paper and left at room temperature (RT) for several days (Figure 12). The same procedure without casting material was performed to obtain non-porous MNs, which served as control (i.e., pure PDMS MNs) throughout the work.

Figure 12: Schematic diagram representing the preparation of porous microneedle array.

2.2. PREPARATION AND OPTIMIZATION OF PDMS MNS

To prepare the porous MNs patches and to investigate the effect of particle size, different PDMS mixtures were prepared with glucose, homogeneous silica nanoparticles, and heterogeneous silica nanoparticles. Homogeneous silica (Glantreo) and heterogeneous silica (Sigma Aldrich) were used as inorganic casting nanomaterial, while glucose, one of the most porogen-used materials to cast PDMS, was used as the organic casting material. It is reported that in general heterogeneous materials, with a wide range of size distribution, make the control of pore distribution hard to achieve. Nevertheless, for interconnectivity of pores and swelling, a network of connected pores is desired, so both strategies with heterogeneous and homogeneous size distribution materials (organic and inorganic), using different concentrations, were investigated in this work. Table 2 lists the casting material used, main physicochemical properties, size distribution, and leaching method required.

Table 2: Casting materials, main physicochemical properties, size distribution, and leaching method.

	Homogeneous Silica	***Heterogeneous Silica***	***Glucose***
Company	Glantreo	Sigma Aldrich	Copan
Medium particle size	Microspheres in nominal diameters of approx..150 nm	Microspheres in diameters between 150 - 1000 nm	Microspheres in diameters between 1000 - 3000 nm
Composition	SiO_2, nonporous	SiO_2, nonporous	$C_6H_{12}O_6$, nonporous
Chemical origin	Inorganic	Inorganic	Organic
Density	2.00 g/cm^3	2.56 g/cm^3	1.56 g/cm^3
Leaching method	Chemical etching with NaOH	Chemical etching with NaOH	Etching with H_2O

2.2.1. GLUCOSE-PDMS MATERIAL

Glucose was used as porogenic material at concentrations of 1%, 5%, and 10% wt. First, the corresponding amount of glucose to each %wt in the test was weighted on a scale and mixed with the PDMS elastomer. The bubbles were removed using a vacuum system and then, the curing agent was mixed (10:1, w/w), and a vacuum was performed again. Lastly, glucose-PDMS was poured into the PMMA mold and cured in an oven at 80 ˚C for 30 min. The MNs were then peeled off from the mold and maintained in a petri dish with water for 10 days to completely dissolve the glucose. During this time, the water was changed several times. Lastly, glucose-modified-PDMS MNs were dried and characterized (cf. sub-section 2.3).

2.2.2. SILICA NANOPARTICLES-PDMS MATERIAL

Silica nanoparticles were used at different concentrations: 0.5%, 1%, 5%, 10% wt. Firstly, the corresponding amount of silica to each %wt in the test was weighted on a scale and mixed with 1 mL of absolute ethanol, except for the case of concentrations with 5% wt or higher, where using 1mL of ethanol was not enough to prevent the aggregation. In this case, 2 mL of absolute ethanol was used instead. Since aggregation of nanoparticles is natural during the fabrication of PDMS-silica nanostructured materials, sonication was applied to disperse the nanomaterial into the PDMS.

Sonication was optimized for each type and concentration of silica, as listed in Table 3. The dispersed nanoparticles and ethanol were then mixed with the PDMS base, followed by a new step of sonication. The ethanol in the mixture was thoroughly evaporated overnight at RT. The PDMS base and curing agent were then mixed at a weight ratio of 10:1. The mixture was stirred uniformly and then put into a vacuum system to remove bubbles for 4 h. The mixture was poured into a mold and cured at 80 °C for 30 min. Then, the PDMS-silica MNS were peeled off.

NaOH was used as a chemical agent to dissolve the silica nanoparticles and created porous MNs. MNs were maintained in a petri dish with 0.1 M of NaOH for 72 h, in an incubator (RT with slow agitation). Additionally, to investigate the possible effect of the etching solution NaOH on the PDMS material, two other molar concentrations of the basic solution NaOH (0.5 M and 1 M) were tested in the sample PDMS-Homogeneous Silica at the highest concentration, i.e., 10%. Lastly, all silica-modified-PDMS samples were washed, dried, and characterized (cf. sub-section 2.3).

Table 3: Time of sonication per type and concentration of Silica Nanoparticles

Silica Nanoparticles (wt%)	***Time of sonication (h)***
Homogeneous Silica 0.5%	2
Homogeneous Silica 1%	2
Homogeneous Silica 5%	4
Homogeneous Silica 10%	4
Heterogeneous Silica 0.5%	2
Heterogeneous Silica 1%	2
Heterogeneous Silica 5%	4

2.2.3 Improving mechanical properties of MNs

To improve the mechanical strength of the produced PDMS porous MNs, hyaluronic acid (HA) was selected as a good candidate due to its inherent characteristics, such as high mechanical strength when solidified due to its natural high viscosity, and rapid dissolution in the presence of water, hydrophilicity, and biocompatibility [118]. To accomplish that, the PDMS modified-MNs were immersed into HA solutions with a concentration of 2 mg/mL, at RT for 48 h, as reported elsewhere [119].

2.3. PHYSICOCHEMICAL CHARACTERIZATION OF PDMS-MODIFIED MNS

2.3.1 IMAGING

Optical microscopy images of the MNs arrays, surface, and cross-sectional were obtained using an optical microscope Nikon Digital Sight DS FI1, with objectives of 4x, 10x, and 20x. Additionally, scanning electron microscopy (NanoSEM, FEI NOVA 200 FEG/SEM) was also performed to assess the pore size distribution of samples in more detail. ImageJ software was used as an imaging analysis software to obtain the average pore size, pore distribution, and dimensions of the MNs.

2.3.2 *AIR PERMEABILITY*

PDMS is naturally permeable to organic solvents, hydrophobic molecules, O_2, CO_2, and air. In this master project, the air permeability of all the produced PDMS-porous samples was experimentally determined through PDMS membranes with 2 mm of thickness. The air permeability is determined by measuring the velocity of the airflow perpendicularly crossing a membrane under specified conditions (surface area, thickness, and pressure). The air permeability of the porous PDMS membranes was measured using an air permeability tester (FX3300 LabAir-IV, TEXTEST AG, Schwerzenbach, Switzerland).

In this study, the test was performed with a surface area of 20 cm^2 and a pressure of 2000 Pa and was carried out based on the standard "NP EN 9237-1997 - Determination of the air permeability of textile" [120]. Measurements were performed for each material at least three times (n=3).

2.3.3 *WETTABILITY*

Wettability was evaluated by measuring the contact angle formed between water drops and the surface of the pure PDMS vs. PDMS-modified samples, using a video-based contact angle optical measurement device, OCA 15 plus, provided with an electronic syringe unit (Dataphysics Instruments GmbH, Germany, Figure 13). Contact angle refers to a method of calculating surface free energy by evaluating the interface of a liquid and a solid surface.

The measurements were carried out at RT. Static contact angles were measured by the sessile drop method, on droplets of 4 μL of water deposited on the surface. Results are shown as the mean value of ten measurements per sample (n=10), photos of water drops on samples were also acquired, and some videos as well.

Figure 13: Dataphysics Instruments GmbH, Germany used to determine the wettability of the porous PDMS samples.

2.3.4 Surface chemistry

The chemical elemental composition of PDMS-modified MNs was determined using an ultra-high-resolution Scanning Electron Microscope with field emission, with an integrated X-ray microanalysis system (EDS - energy dispersive spectrometer), (SEM-EDS, NanoSEM, FEI NOVA 200 /FEG/SEM - Pegasus X4M). In order to permit or enhance the imaging of samples during electron microscopy, coating of the samples with a conductive layer of metal is usually necessary, which will inhibit charging, minimize heat damage, and enhance the secondary electron signal necessary for topographic analysis in SEM. For that, gold (Au) was used to coat MNs. The given EDS results were calculated as average over three measurements per sample (n=3).

2.3.5 MECHANICAL PROPERTIES

Dynamic mechanical analysis (DMA) was used to evaluate the viscoelastic behavior of the PDMS-modified MNs materials. Rectangular samples (length = 10 mm, width = 6 mm, and thickness = 2 mm) were tested in *ss* control mode to generate stress plots, which allow the calculation of Young's Modulus. *ss* control mode, at an oscillatory frequency of 1 Hz, RT temperature (25 ˚C), and 100 μm/min displacement, was applied using a dynamic-mechanical analyzer (DMA7100 thermal analysis system, Figure 14). Stress *versus* strain curves was generated by measuring force and displacement, while the test station pressed the sample. The value of the Young's Modulus (E) was determined by fitting the experimental force (F) versus displacement (δ), via linear regression (n=3).

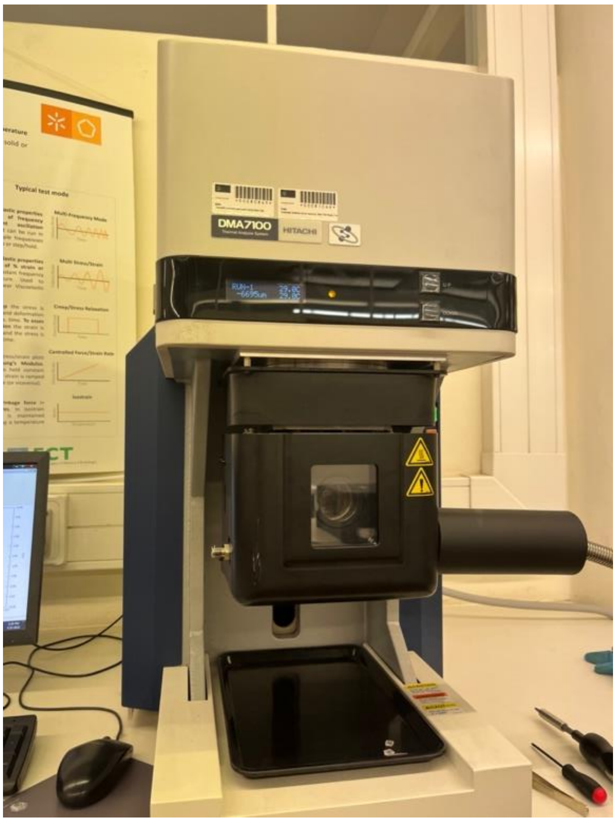

Figure 14: DMA7100 thermal analysis system used to determine the mechanical properties of porous-PDMS samples.

2.3.6 POROSITY

The porosity is an important factor directly related to the amount of fluid that can be loaded into the porous MNs arrays. To determine the porosity of the modified-PDMS samples (after etching and functionalized with HA), samples were dried for 30 minutes in an oven at 80˚C and weighed. After 12 h immersed in water, MNs were gently dried with non-absorbent paper to remove excess water and weighed. Then, the porosity percentage of the samples was determined as Equation 1:

$$Porosity\ (\%) = \frac{\frac{wi-wf}{pWater}}{\frac{wi}{\rho PDMS}+\frac{wi-wf}{\rho Water}} \times 100 \tag{1}$$

where w_f and w_i are the final and initial weight of the MNs samples, respectively. ρ_{Water} is the density of water, and ρ_{PDMS} is the density of PDMS [121].

The given values of swelling were calculated as average over three measurements per sample (n=3).

2.3.7. SWELLING

The swelling capacity of the porous MN was determined using water as a swelling fluid. The swelling capacity was calculated as the volume difference between the porous MN sample after swelling and the dried state (before swelling). MNs swelling was studied by immersing a dried and pre-weighed sample in water at different time points: 5, 10, 15, 30, 60, and 120 min. The MNs were removed, gently dried with non-absorbent paper, and weight at different time points (5, 10, 15, 30, 60, and 120 min). Swelling of samples was determined by using Equation 2, and expressed in %:

$$Swelling\ (\%) = \frac{wi-wf}{wi} \times\ 100 \qquad (2)$$

where w_f and w_i are the final and initial weight of the used MNs, respectively [122]. The given values of swelling were calculated as average over three measurements per sample (n=3).

2.3.8 STATISTICAL ANALYSIS

All data were treated with GraphPad software (version 9.3.1), and the values were presented as mean ± standard deviation (SD). Significance was assessed with the student's *t*-test using a significance of 5% (p=0.05).

3. RESULTS AND DISCUSSION

3.1 MICRONEEDLES

Figure 15 represents some examples of the macroscopic differences observed in digital photos. Overall, all the MN samples were well-defined and flexible enough to withstand the pressure from a finger. Some curvatures in the tip were also observed, due to the lack of mechanical strength of pure PDMS or modified-PDMS MNs. Figure 15A and Figure 15B show PDMS-glucose 5% (w/w) MNs, where it is possible to observe the glucose particles with the naked eye, just by observing the MN-array, which correlates to the µm size of these particles and possible agglomerations (cf. Table 2). On the other hand, PDMS-Homogeneous silica 5% (w/w) (Figure 15C) seems whiter than control pure PDMS MNs (Figure 15D), which are translucent. In this case, due to their nano size (cf. Table 2), the observation of the particles requires size amplification using electron microscopy tools, which will be shown in the next sub-chapter 3.2.

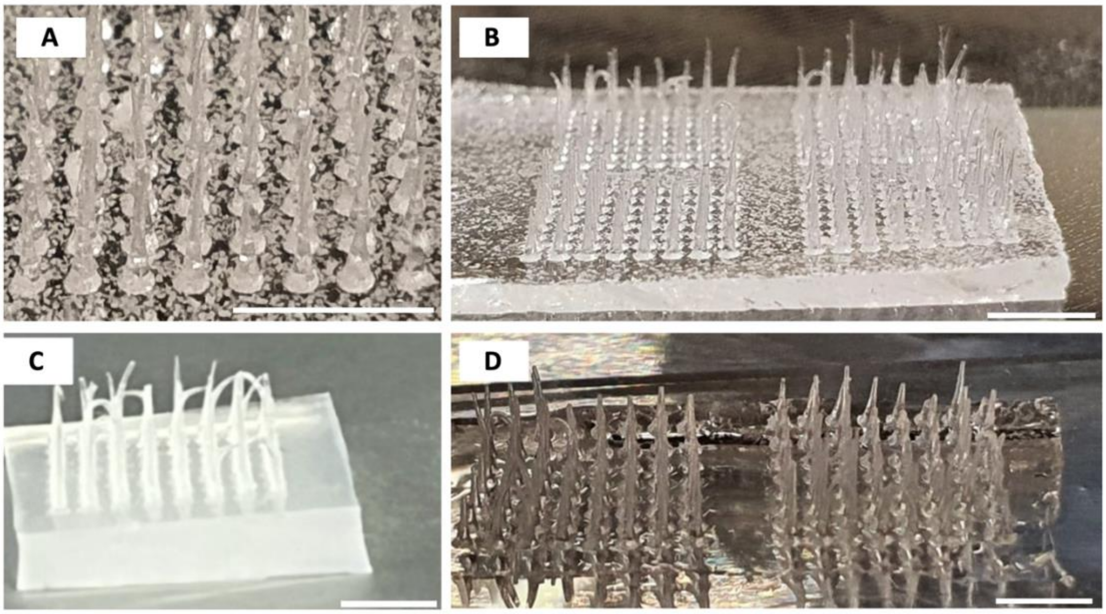

Figure 15: Digital photos of PDMS MNs. **A** PDMS-Glucose 5% (w/w) MNs with 2x Zoom, **B** PDMS-Glucose 5% (w/w) MNs, **C** PDMS-Homogeneous Silica 5% (w/w) MNs, **D** Pure PDMS MNs. Scale bars corresponding to 3000 µm.

In these arrays (Figure 15D), the 64 cone-shaped MNs are orderly arranged on the PDMS substrate. Based on microscopy images, the tip diameter of each microneedle is approximately 200 µm, the base diameter of each microneedle is approximately 666 µm and the distance between the microneedle bases is around 980 µm. The height of the resultant microneedles ranges from 332 µm to 1442 µm. This height difference is intentional and desired for the final purpose – the fabrication of microneedles with different heights to access different regions within an organoid model.

Pure PDMS MNs (Figure 16A), PDMS MN at the highest concentration of glucose (Figure 16B), homogeneous silica (Figure 16C), and heterogeneous silica (Figure 16D) are represented in Figure 16. Although the definition of these images is not ideal, some porous (dark spots) can be noticed in Figure 16, proving the accomplishment to cast porous using the selected materials.

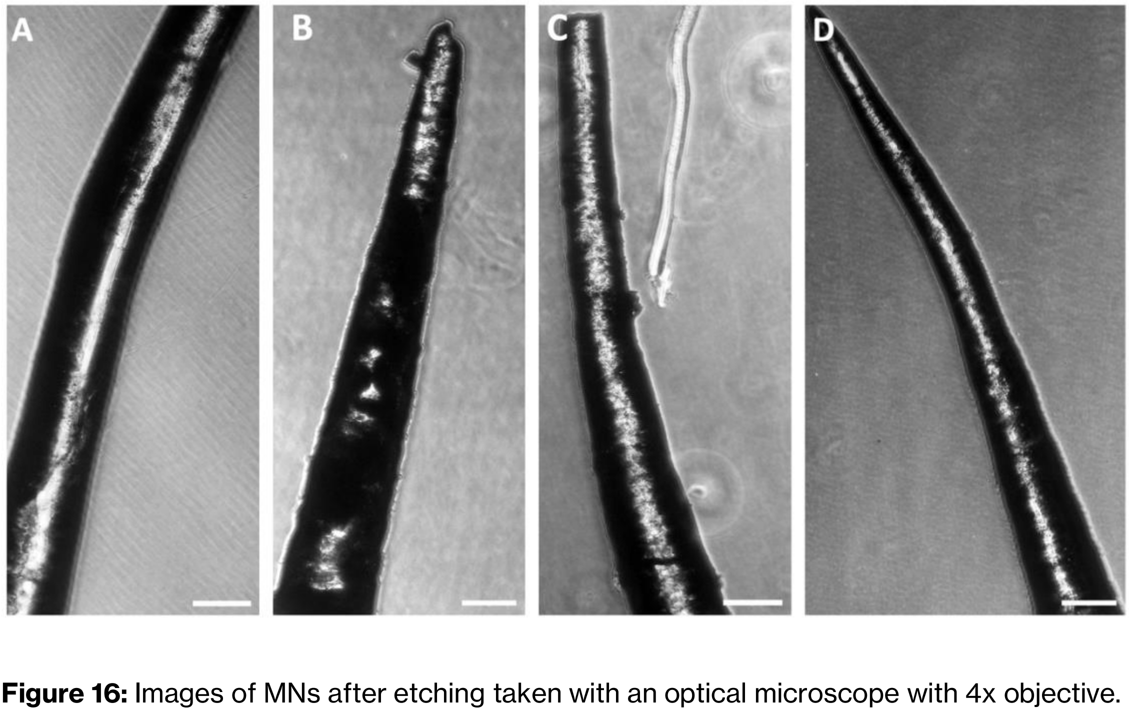

Figure 16: Images of MNs after etching taken with an optical microscope with 4x objective. **A** pure PDMS, **B** PDMS-Glucose 10% (w/w) MNs, **C** PDMS-Homogeneous Silica 10%, **D** PDMS-Heterogeneous Silica 5% (w/w) MNs. Scale bars corresponding to 100 µm.

Figure 17 shows the pure PDMS MNs in detail, without observation of porosity in the MNs. Due to the viscoelastic properties of PDMS, it is possible to observe some irregular textures in the needle.

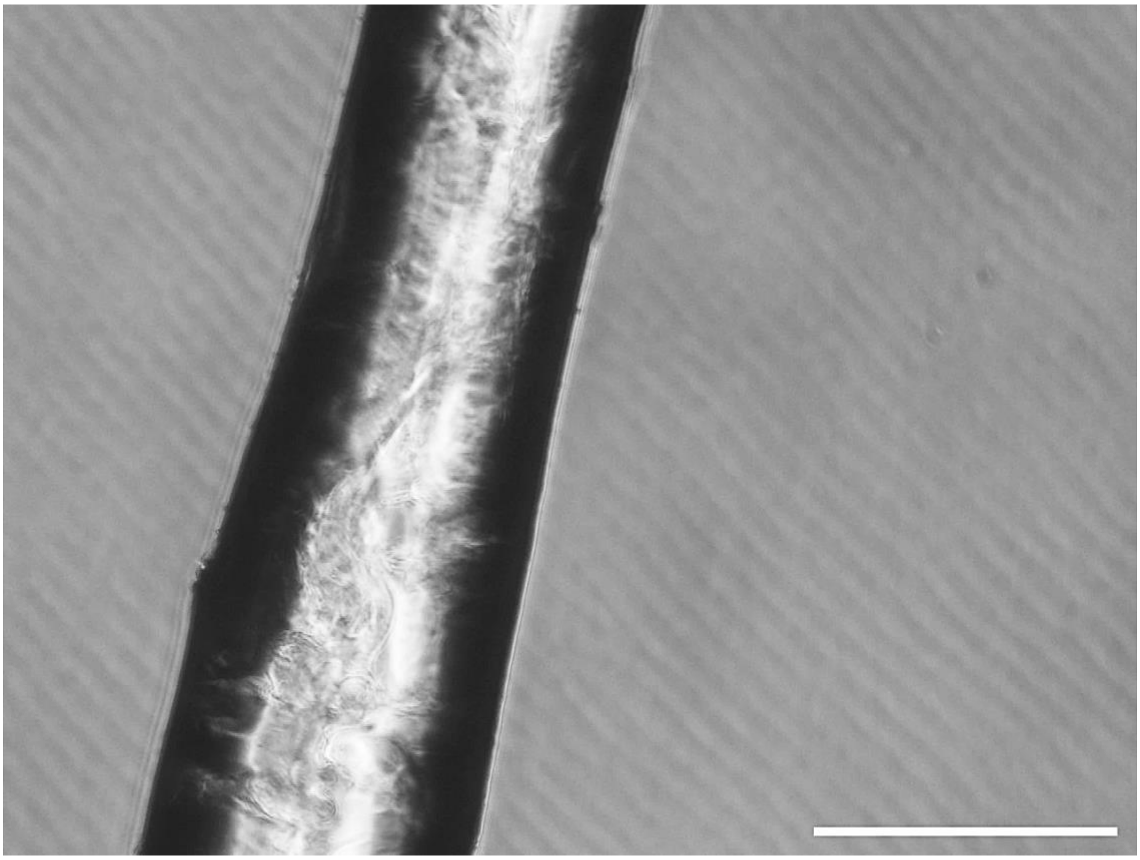

Figure 17: Microscopic image of pure PDMS MNs (middle zone) with 10x objective. Scale bars corresponding to 500 µm.

PDMS-Glucose MNs before and after etching are represented in Figure 18. From Figure 18, it is observable the wide range in size of the glucose particles and their heterogeneity on the final porous network. For example, in low concentration glucose-PDMS MNs (Glucose 1% (w/w) before etching, it seems that only the smallest particles are observed in the MNs (Figure 18A), which after etching reveals the formation of the best outcome for PDMS-Glucose MNs (Figure 18D). Increasing the concentration to Glucose 5% (w/w) apparently shows big pores but in a low number. (Figure 18B, Figure 18E). However, the biggest pores come with Glucose 10% (w/w), with fewer particles being cast into MNs that become porous after etching (Figure 18C, Figure 18F).

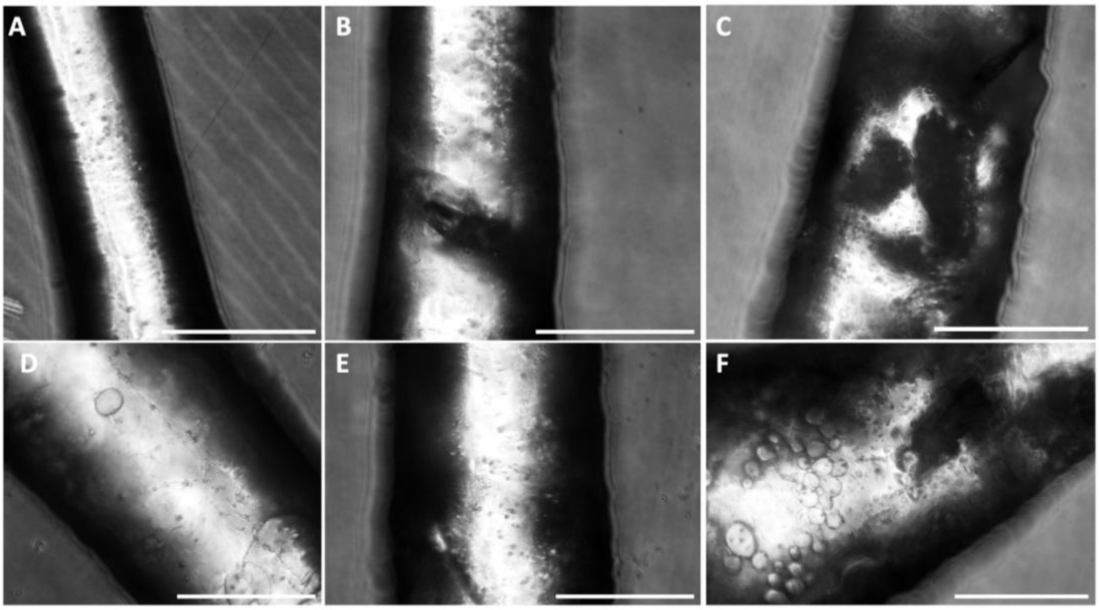

Figure 18: Microscopic images of PDMS-Glucose MNs with 20x objective. **A-C** PDMS-Glucose MNs before etching, **D-F** PDMS-Glucose MNs after etching, **A, D** PDMS-Glucose 1% (w/w), **B, E** PDMS-Glucose 5% (w/w), **C, F** PDMS-Glucose 10% (w/w). Scale bars corresponding to 500 µm.

As aforementioned, glucose has a wide range of particle sizes (1000-3000 nm), which can be a challenge to the biggest glucose particles in solution with PDMS to penetrate the MN mold. This statement can be observed in Figure 19A.2, which shows the casting of a big pore (approx. 250 µm) in the PDMS, possibly due to an agglomeration of glucose particles into this spot. Also, the cone shape of the MN design can promote some difficulties for the biggest glucose particles achieving the tip of MNs, which creates a more heterogeneous porous network in the PDMS-Glucose MNs, where only the smallest glucose particles are cast, as observed in Figure 19.

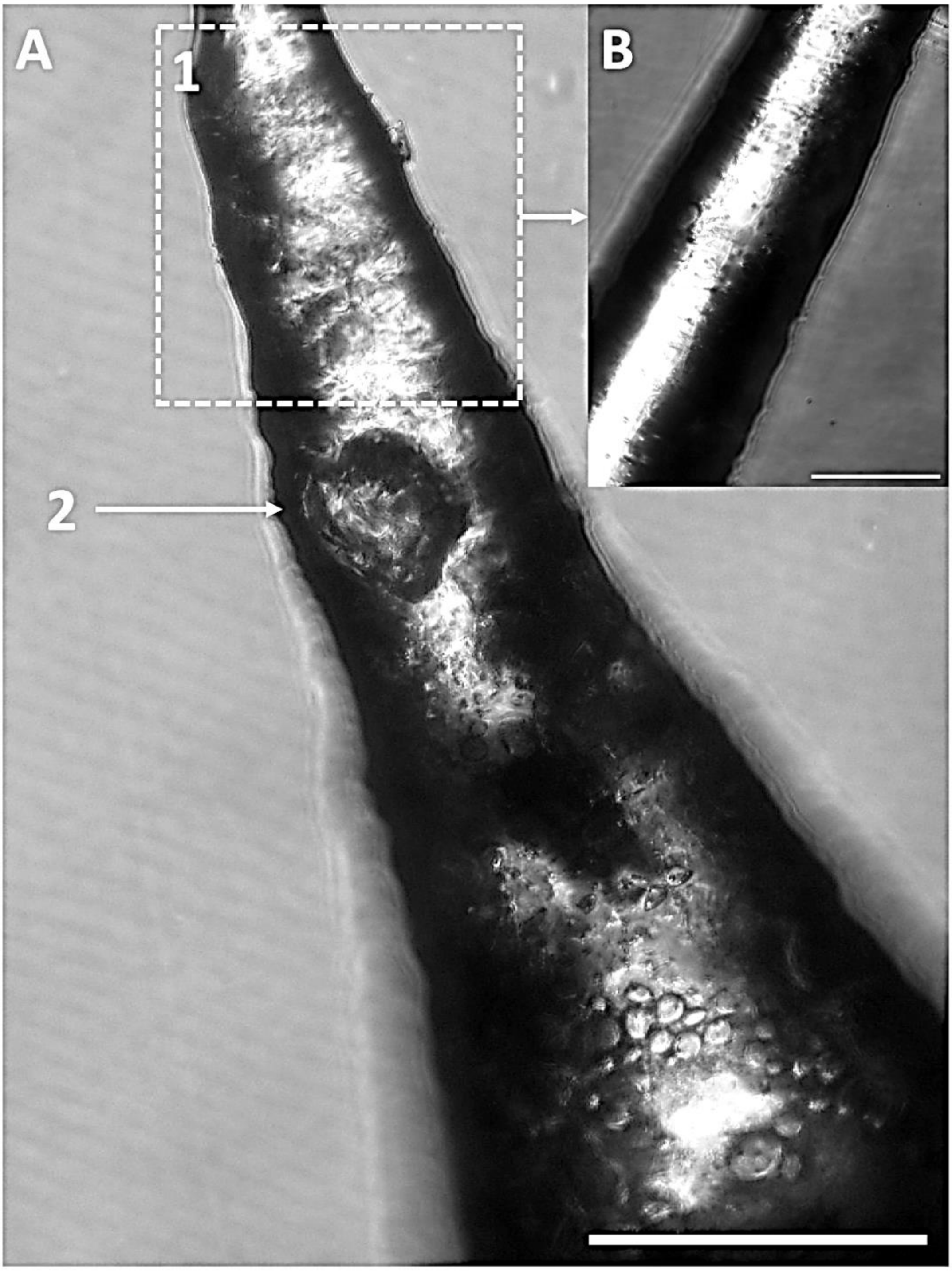

Figure 19: Microscopic images of PDMS-Glucose 10% (w/w) MNs after etching. **A** 10x objective with, **1.** Tip of MN and **2.** Porous, **B** 20x objective on tip zone. Scale bars corresponding to 500 µm.

By comparing heterogeneous glucose with heterogeneous silica, it is possible to observe at comparable lower concentrations, 0.5 and 1% (w/w), that PDMS-Heterogeneous Silica presents a higher concentration of porous (Figure 20A, Figure 20D and Figure 20B, Figure 20E). This can be explained due to the lower particle range size of the heterogeneous silica (150-1000 nm), compared to glucose (1000-3000 nm), which can facilitate the penetration of the porogenic material into the MN mold. Apparently, by increasing the concentration of porogenic silica material, the porous concentration in the PDMS MNs also increased. However, additional characterization is needed to confirm these first observations due to the low size of the porogenic material (nm) and low resolution of the microscopic images.

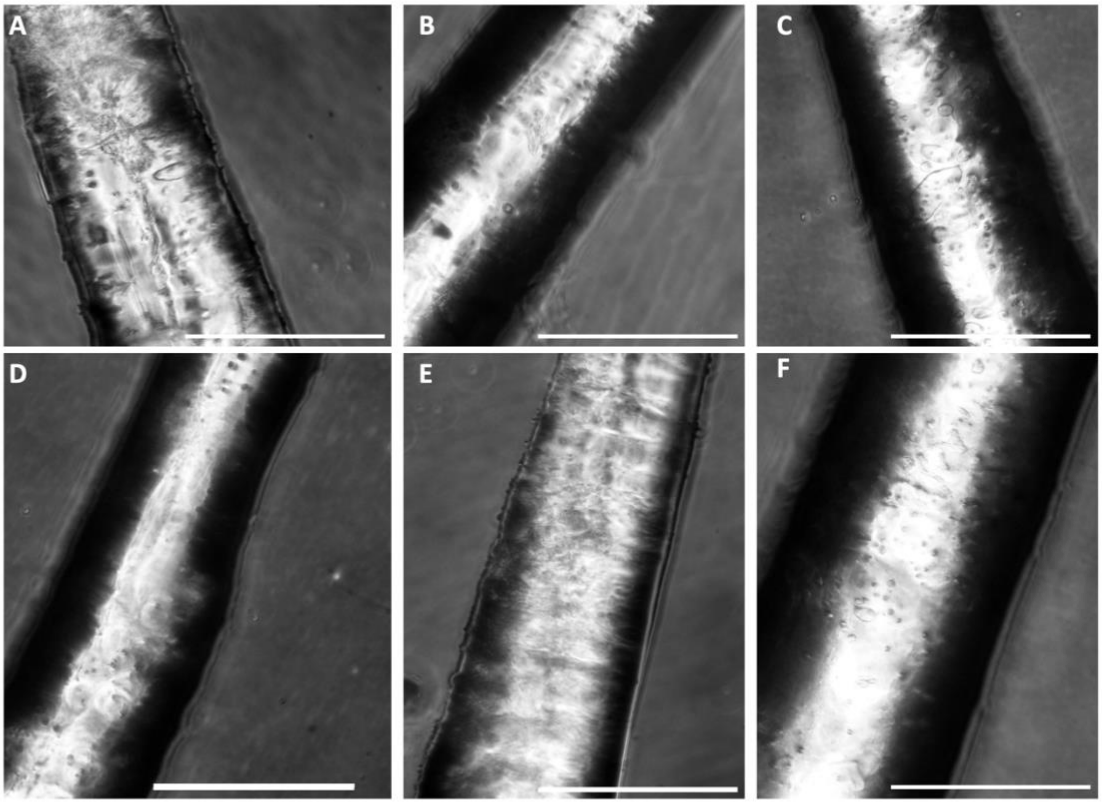

Figure 20: Microscopic images of PDMS-heterogeneous Silica MNs with 20x objective. **A-C** PDMS-Heterogeneous Silica MNs**, D-F** PDMS-Heterogeneous Silica MNs after etching, **A, D** PDMS-Heterogeneous Silica 0.5% (w/w), **B, E** PDMS-Heterogeneous Silica 1% (w/w), **C, F** PDMS-Heterogeneous Silica 5% (w/w). Scale bars corresponding to 500 µm.

Lastly, PDMS-Homogeneous Silica MNs were evaluated. Compared with previous images of MNs, the results for all concentrations seem more consistent, which can be explained by the particles' smaller and narrow size range (approx. 150 nm), Figure 21. Comparing the porous matrix created at similar concentrations (0.5%, 1%, and 5%) with the previous porogenic materials, the number of casted nanoparticles (Figure 21A to Figure 21D) on PDMS-Homogeneous Silica MNs is apparently higher than on the MNs with other materials, as well as the number of porous created after etching (Figure 21E to Figure 21H). Once again, the higher concentration of PDMS-Homogeneous Silica 5% (w/w) MNs and PDMS-Homogeneous Silica 10% (w/w) MNs, appear to show a higher presence of porous in the MN surface matrix. Overall, these last results indicate that homogeneous silica seems to have a greater potential to create (at least on the MN surface) a high and uniformed interconnected network of porous when compared to the other porogenic samples.

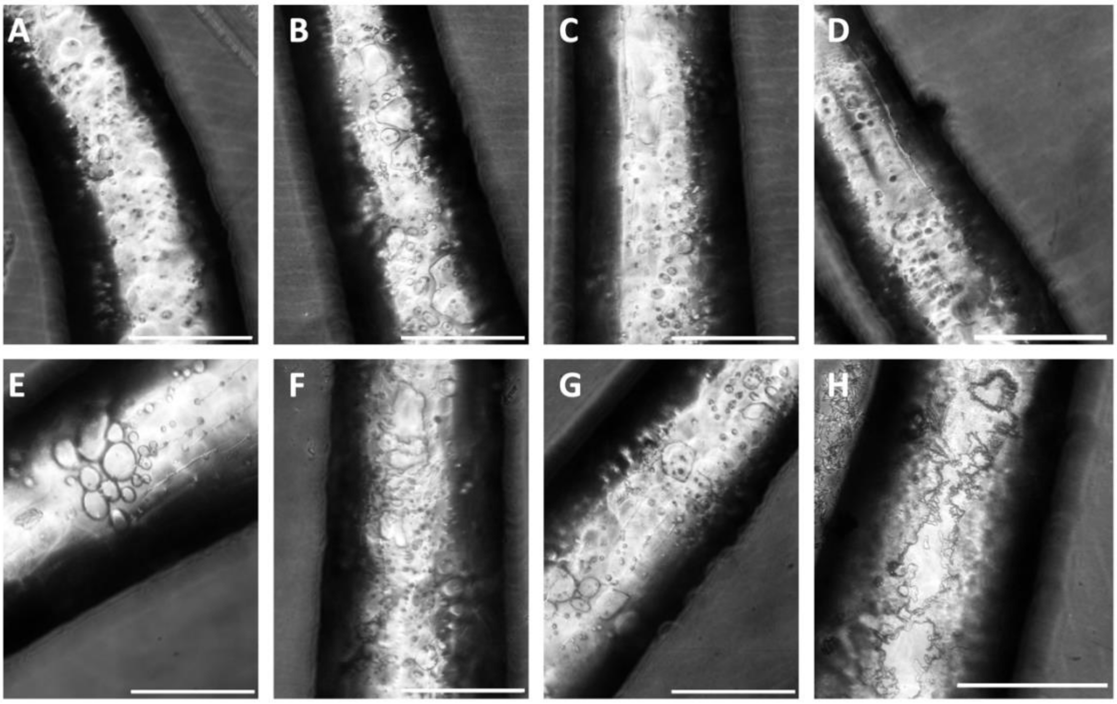

Figure 21: Microscopic images of PDMS-Homogeneous Silica MNs with 20x objective, **A-D** PDMS-Homogeneous Silica MNs, **E-H** PDMS-Homogeneous Silica MNs after etching, **A, E** PDMS-Homogeneous Silica 0.5% (w/w), **B, F** PDMS-Homogeneous Silica 1% (w/w), **C, G** PDMS-Homogeneous Silica 5% (w/w), **D, H** PDMS-Homogeneous Silica 10% (w/w). Scale bars corresponding to 500 μm.

As referred before, due to the low resolution of the optical microscope (max. 20x objective), and difficulty to observe pores and their interconnectivity, SEM imaging was performed to complement the morphologic characterization of the porous MNs samples.

3.2 SEM ANALYSIS

Based on the previous imaging results, the samples that showed the most promising porous MN arrays were selected for SEM analysis. Therefore, samples obtained with higher concentrations of porogenic materials were selected, namely, (1) PDMS-Glucose 5% (w/w), (2) PDMS-Glucose 10% (w/w), (3) PDMS-Homogeneous Silica 5% (w/w), (4) PDMS-Heterogeneous Silica 5% (w/w), and (5) PDMS-Homogeneous Silica 10% (w/w) after etching and also after HA treatment. Additionally, PDMS-Homogeneous Silica 10% (w/w) treated with different concentrations of NaOH (0.5 and 1.0 M), as an etching solution, were analyzed to predict the effect of the basic solution in dissolving the silica nanoparticles and its possible effect on the PDMS matrix. Pure PDMS MN array was used as control.

Figure 22 represents the pure PDMS MN arrays (group control, Figure 22A). Instead of a smooth surface observed under the optical microscope (Figure 17), in Figure 22 pure PDMS MN presents some roughness (in more detail in Figure 22B and Figure 22C). The apparent roughness can be explained due to the mold imperfections caused by the laser beam and the surface damage caused by the PDMS peeling from the PMMA MN mold. This last observation is visible along several MNs images, independently from the sample, where MN tips are often cut off.

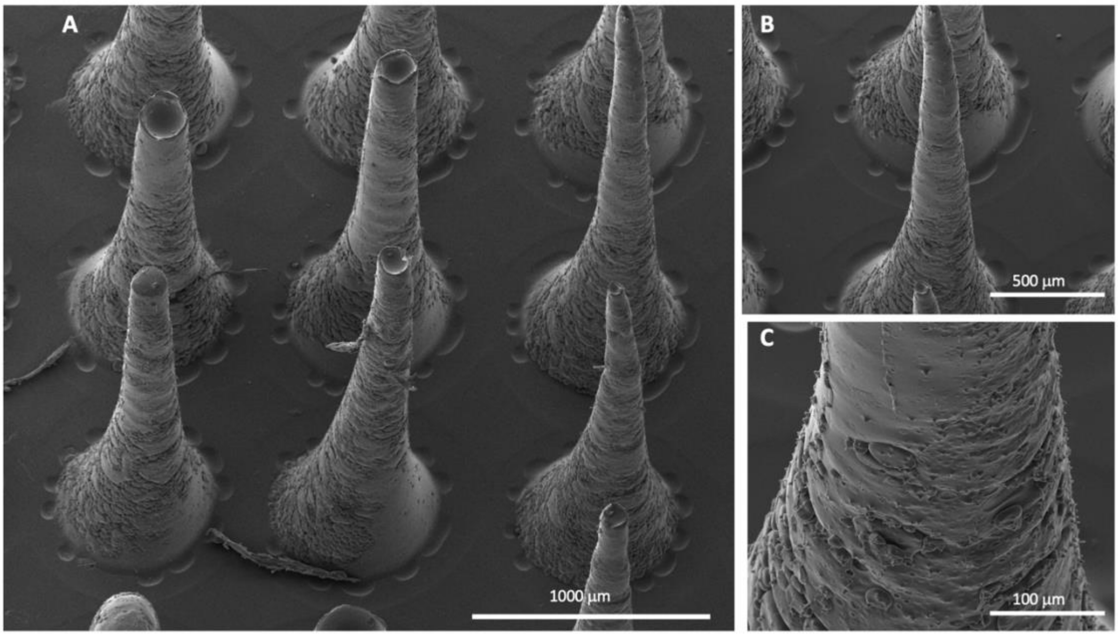

Figure 22: SEM images of pure PDMS MNs. **A:** MN array, **B:** Zoom image of a single MN, **C:** Detail of the base of a single MN.

By using ImageJ, SEM images were analyzed to determine MNs dimensions. Due to the higher optical resolution of SEM, the measurement and analysis of porous samples were possible. Figure 23 represents the number of porous per type of MNs analyzed. Overall, at 5% of concentration, the number of porous is higher with PDMS-Homogeneous Silica than with PDMS-Glucose. By increasing the homogeneous silica concentration to 10%, the number of pores reaches a maximum of 28±5 pores per MN section (considering pores with sizes higher than 5.8 μm).

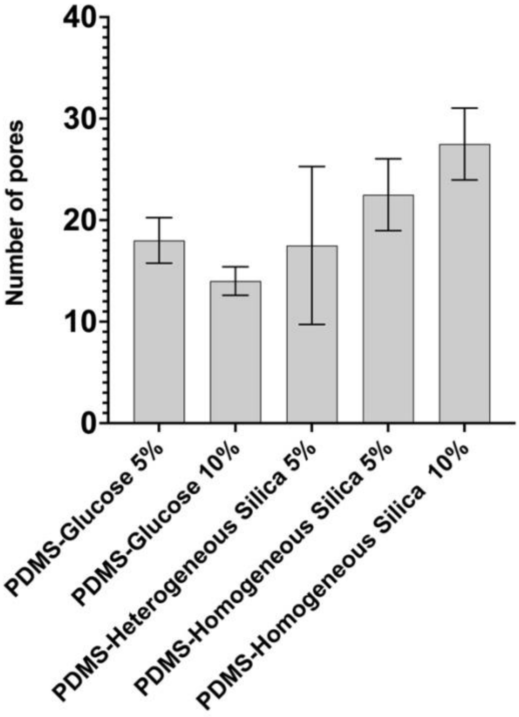

Figure 23: Number of pores in MNs. Error bars represent SD (n=3).

Figure 24 shows the pore dimension for each kind of MN that was examined. In this case, the PDMS-Glucose MNs exhibit larger pores dimensions than PDMS-Homogeneous Silica MNs, which exhibit smaller pores. Despite having few pores, the pore size is large on PDMS-Glucose MNs, leading to a higher volume of pores. However, for the intended application of the PDMS porous MNs, a more important parameter than the pore percentage is their density and interconnectivity. Which is expected to allow the swelling and flow of the fluid captured. Therefore, it is crucial to consider besides pores percentage, other parameters, such as homogeneous distribution, interconnectivity, and density.

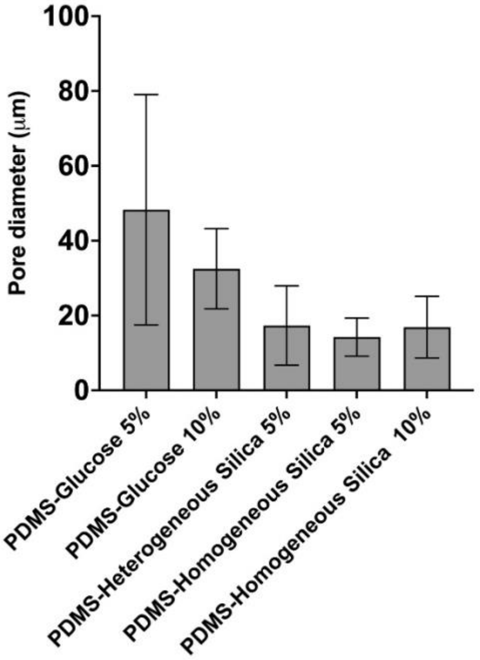

Figure 24: Pore dimensions of MNs. Error bars represent SD (n=20).

Figure 25 and Figure 26 present SEM images from PDMS-Glucose. Overall, PDMS-Glucose 5% (w/w) after etching (Figure 25A and Figure 25B) and PDMS-Glucose 10% (w/w) after etching (Figure 26A and Figure 26B), show the presence of porosity created by the casting materials (cf Figure 23 and Figure 24). In comparison with pure PDMS (Figure 22), it is noticed that glucose is also cast into the flat base of the MNs. Although some pores resulting from microbubbles are shown as well. PDMS-Glucose 5% (w/w) after etching and treated with HA solution (Figure 25C and Figure 25D) and PDMS-Glucose 10% (w/w) after etching and treated with HA solution (Figure 26C and Figure 26D) demonstrate resemblance to samples without HA solution, without a significant difference between them (results presented in Annex 1, where it lists the number and size of pores for each MN).

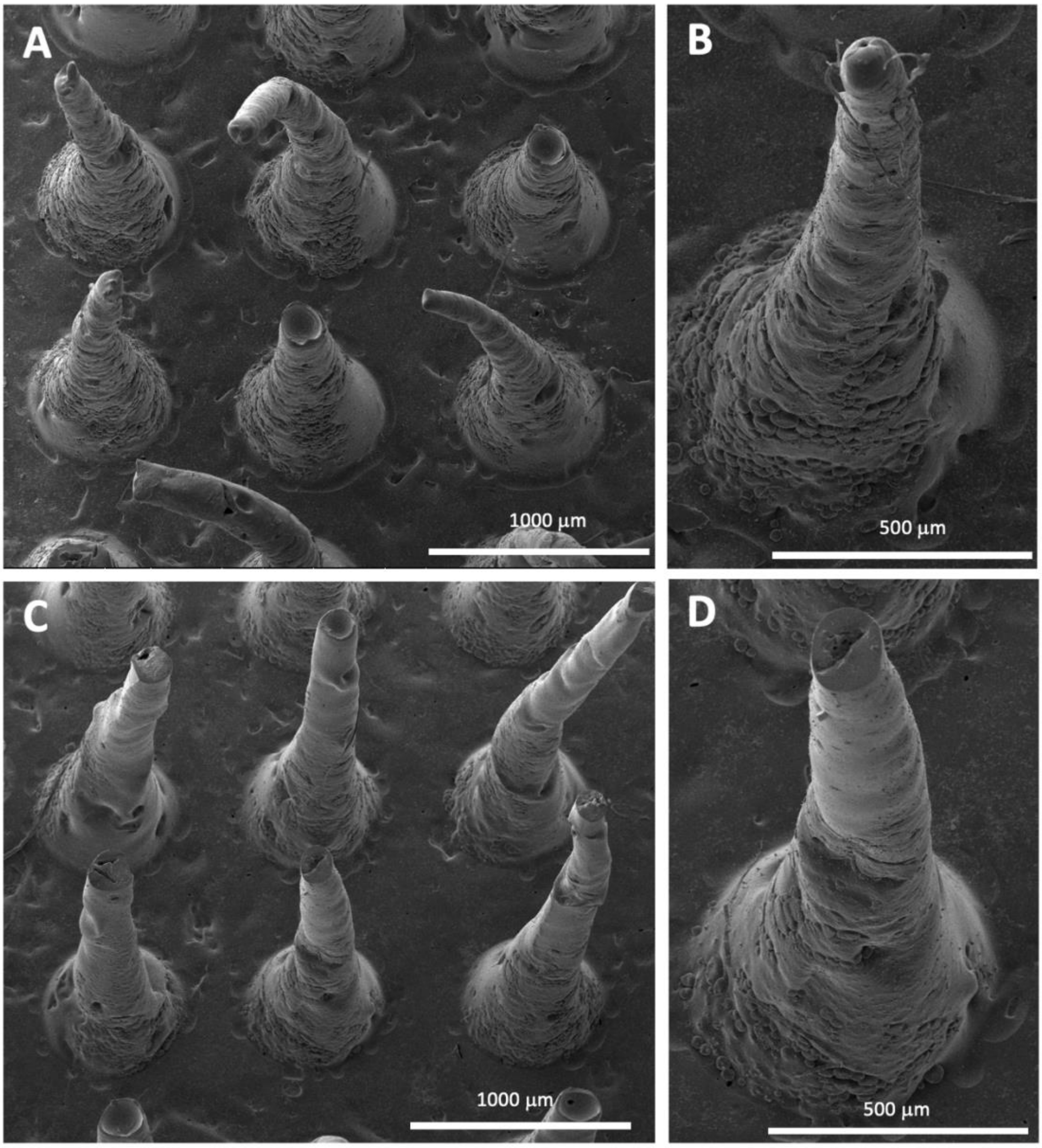

Figure 25: PDMS-Glucose 5% (w/w). **A, B** PDMS-Glucose 5% (w/w) after etching, **C, D** PDMS-Glucose 5% (w/w) after etching and treated with HA solution.

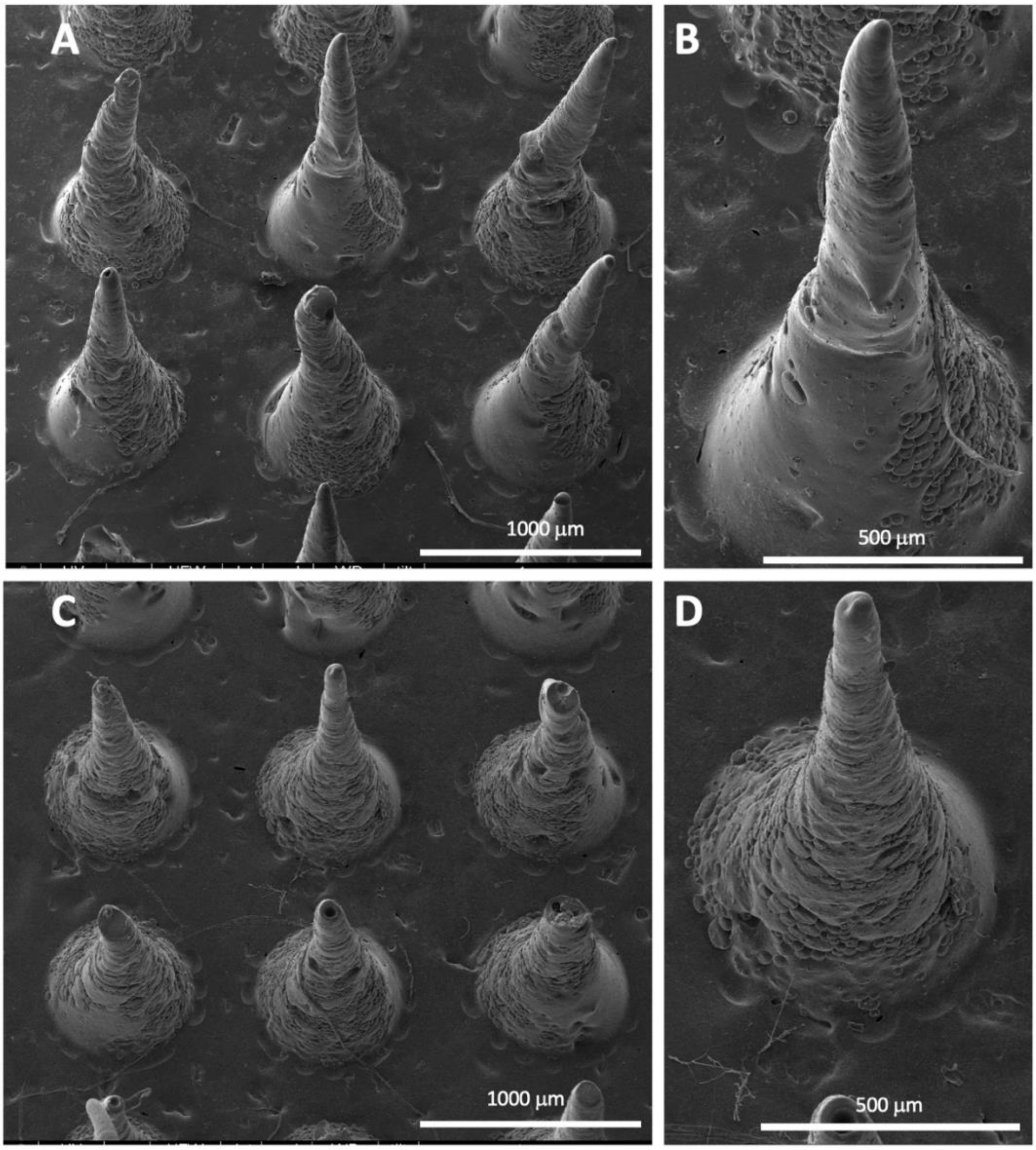

Figure 26: PDMS-Glucose 10% (w/w). **A, B** PDMS-Glucose 10% (w/w) after etching, **C, D** PDMS-Glucose 10% (w/w) after etching and treated with HA solution.

Comparing the PDMS-Glucose 5% MNs with the PDMS-Silica 5% (w/w) MNs, both homogeneous (Figure 27) and heterogeneous (Figure 28), it seems that the porosity density on the modified-silica MN's surface increases, although the size dimension decreases. This observation can also be observed in the smoother flat base of the MN. However, it is important to have in mind that these SEM images show the MN surface porous density, but not the inner part of MNs, which can differ from the inner zone. This analysis will be further investigated based on other characterizations, such as swelling and air permeability, presented in the following sub-chapters.

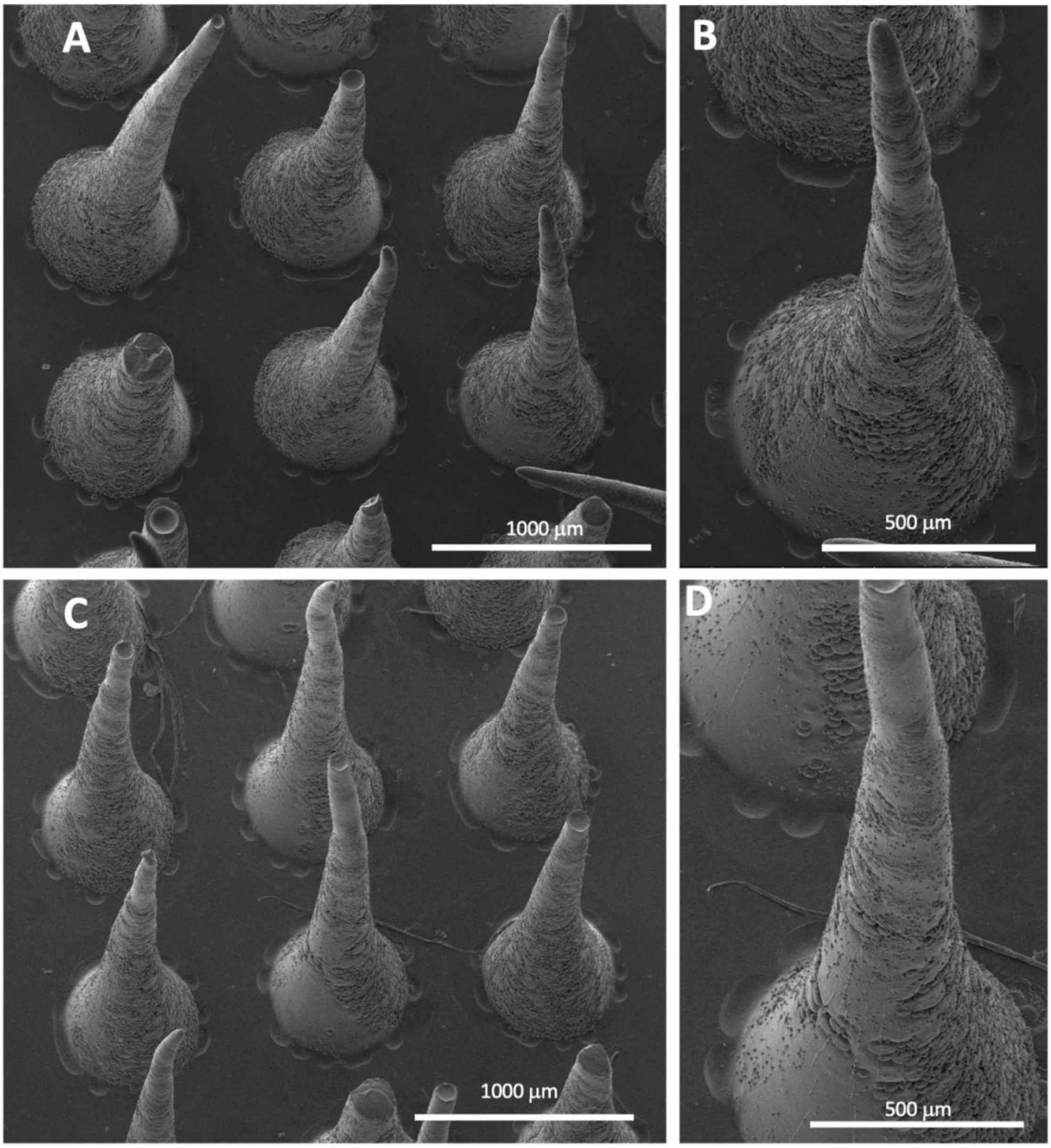

Figure 27: PDMS-Homogeneous Silica 5% (w/w). **A, B** PDMS-Homogeneous Silica 5% (w/w) after etching, **C, D** PDMS-Homogeneous Silica 5% (w/w) after etching and treated with HA solution.

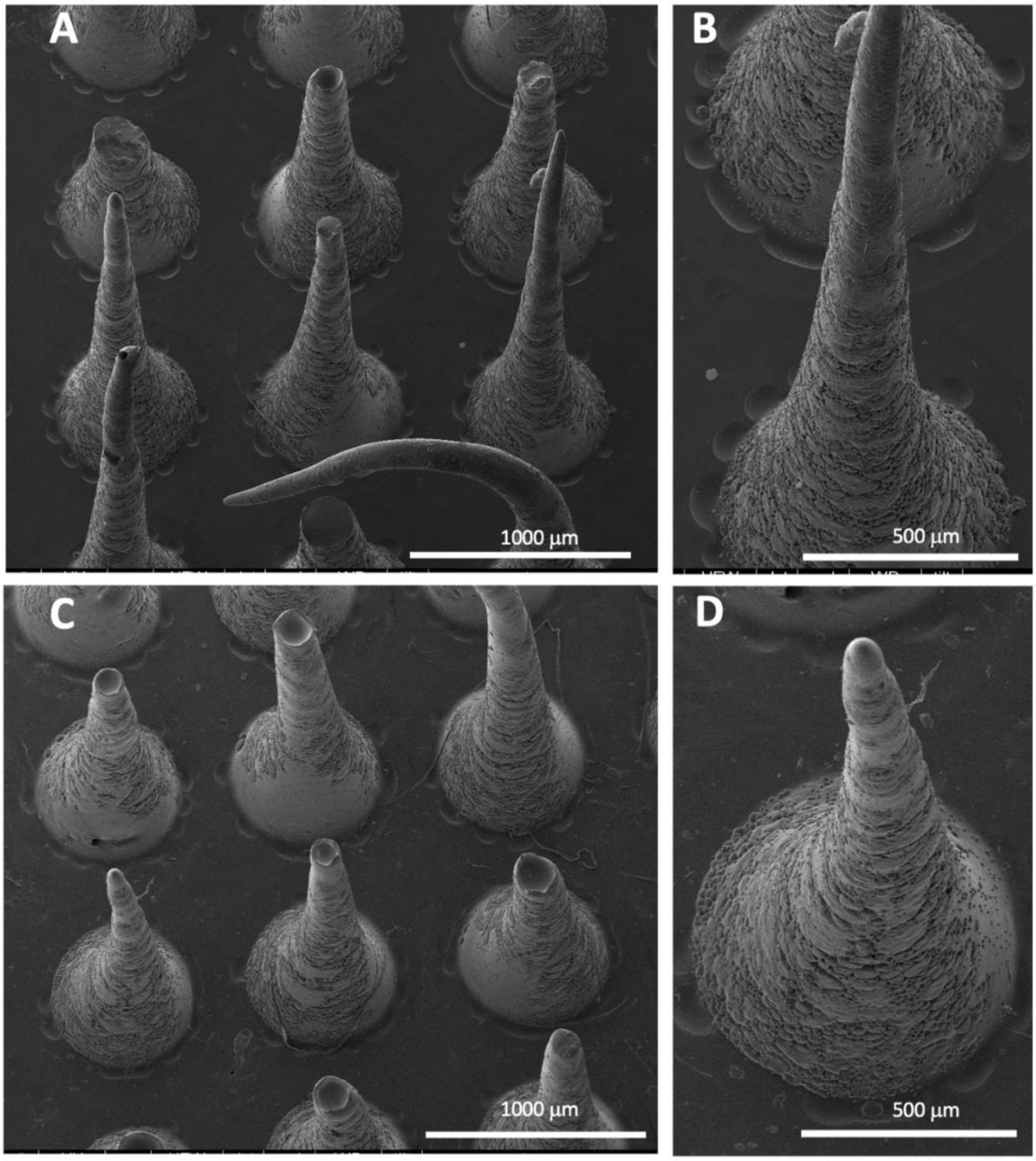

Figure 28: PDMS-Heterogeneous Silica 5% (w/w). **A,B** PDMS-Heterogeneous Silica 5% (w/w) after etching, **C,D** PDMS-Heterogeneous Silica 5% (w/w) after etching and treated with HA solution.

PDMS-Homogeneous Silica 10% (w/w) with different concentrations of etching solution (Figure 29) was studied to understand the impact of the NaOH etching treatment on the PDMS surface, i.e. porosity. In contrast with PDMS-Homogeneous Silica 5% (w/w) (Figure 27A, Figure 27B), PDMS-Homogeneous Silica 10% (w/w) (Figure 29A and Figure 29B) treated with normal etching solution (0.1 M) shows higher porosity density, has confirmed in Figure 24. Comparing the increment in etching solution concentration and fixing Homogeneous Silica at 10% (W/W) in PDMS, it is possible to observe that porosity increases as well. Although, apparently at 0.5 or 1 M NaOH the size of pores is similar. This can also be observed by analyzing : Figure 29A, B (etching with 0.1 M) Figure 29C, D (etching with 0.5 M), and Figure 29E, F (etching with 1 M). Figure 30, shows the quantitative analysis of these samples where the number of pores and mean diameter of pores are compared between samples PDMS-Homogeneous Silica at 10% at different NaOH etching concentrations. Although the size of the pores is similar (Figure 30B), the increase in the etching solution causes an increase in the number of pores (Figure 30A). Proving that the etching solution has an impact on the porous network, possibly due to better removal of Si nanoparticles, but also due to the attack on the Si structure of the PDMS matrix [123]**.** Overall, PDMS-Homogeneous Silica 10% (w/w) with NaOH etching solution between 0.5 and 1 M shows the best condition to promote a higher density and homogeneous network of porous in the MN PDMS matrix, compared to the other modified-PDMS samples.

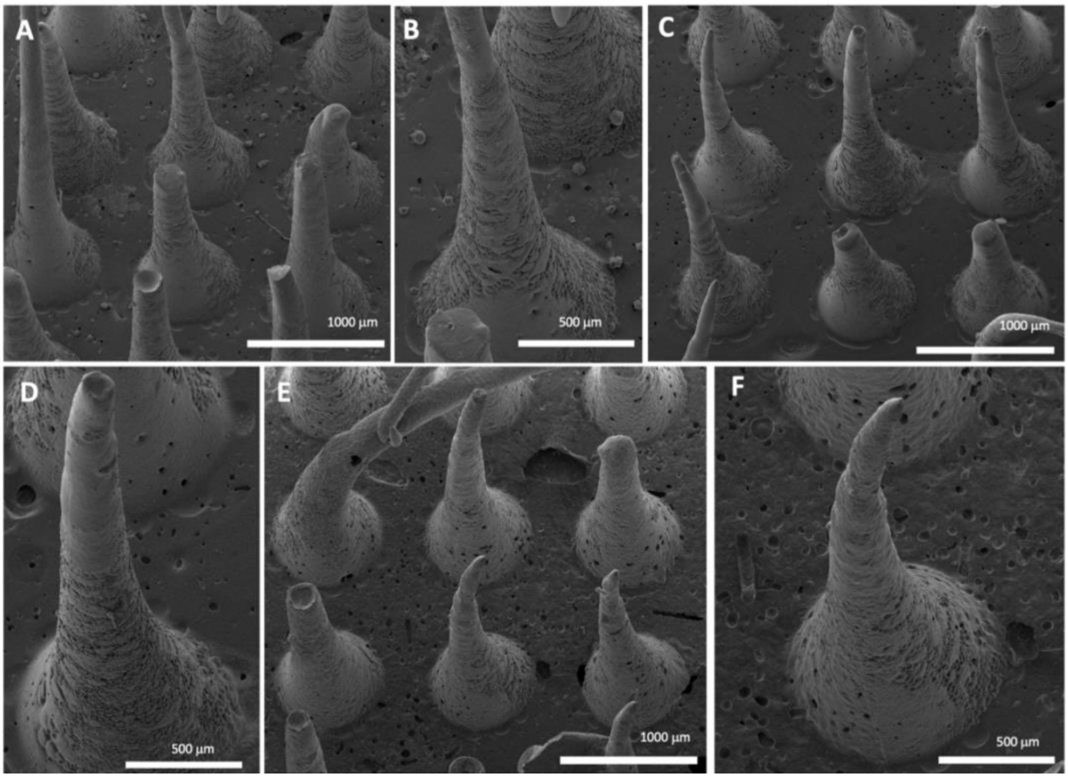

Figure 29: PDMS-Homogeneous Silica 10% (w/w). **A, B** PDMS-Homogeneous Silica 10% (w/w) after etching 0.1 M, **C,D** PDMS-Homogeneous Silica 10% (w/w) after etching - 0.5 M solution, **E,F** PDMS-homogeneous Silica 10% (w/w) after etching – 1 M solution.

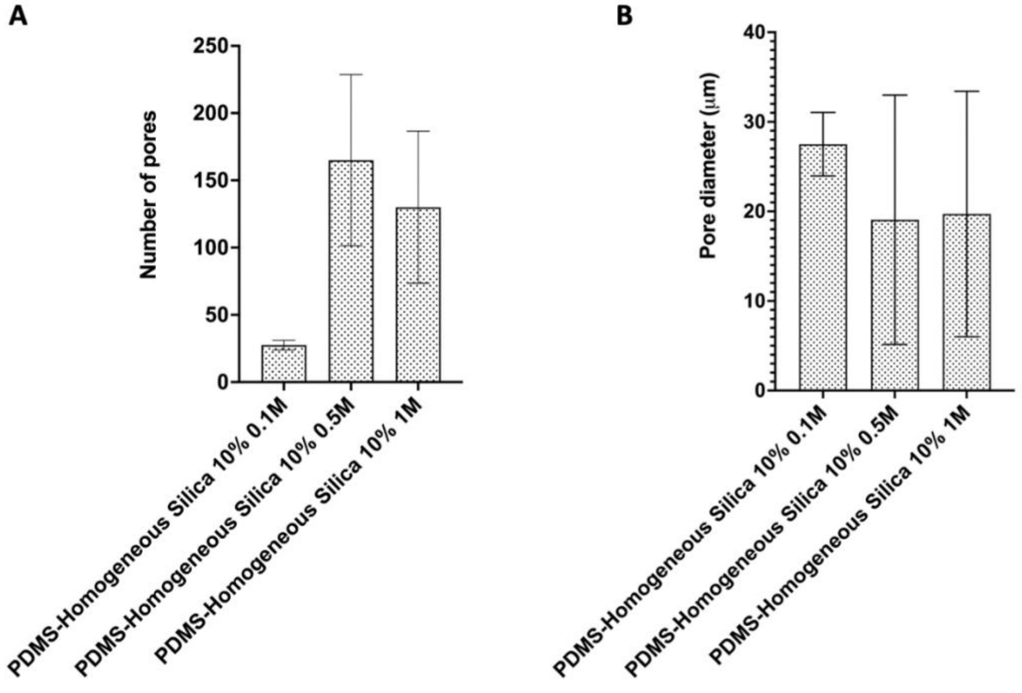

Figure 30: Pore analysis of PDMS-Homogeneous Silica 10% MNs after NaOH etching treatment (0.1, 0.5, and 1 M). **A.** Number of pores (n=3), **B.** Pore dimension (n=20). Error bars represent SD.

3.3 PERMEABILITY

The air permeability of the porous membranes, according to the membrane thickness of 2 mm, was measured to evaluate the effect of porosity on the modified-PDMS sample membranes, namely; before and after etching MNs, as well as MNs after etching and treated with HA solution.

It is important to retain that air permeability refers to the ability of a membrane to be crossed by the air through the existing pores network. Therefore, the higher the air permeability in a sample, the better network of interconnecting pores is expected to be observed.

For comparison basis, pure PDMS air permeability was acquired as control, revealing an experimental value of (4,76 l/m^2/s, at 2000 Pa). Based on the air permeability results shown in Figure 31, Figure 32, and Figure 33, the air permeability value of pure PDMS is approximability the same as all the modified-PDMS samples membranes before etching. Thus, before etching, and as expected, Glucose membranes Figure 31, and Silica membranes (Figure 32 and Figure 33) have similar results, independently of the concentration and size of the porogen material applied. These results are an indication of the non-existing porous networks in the membranes, caused by the clogging of the porogenic material in the PDMS membrane, which causes the resistance for the air to flow through the PDMS.

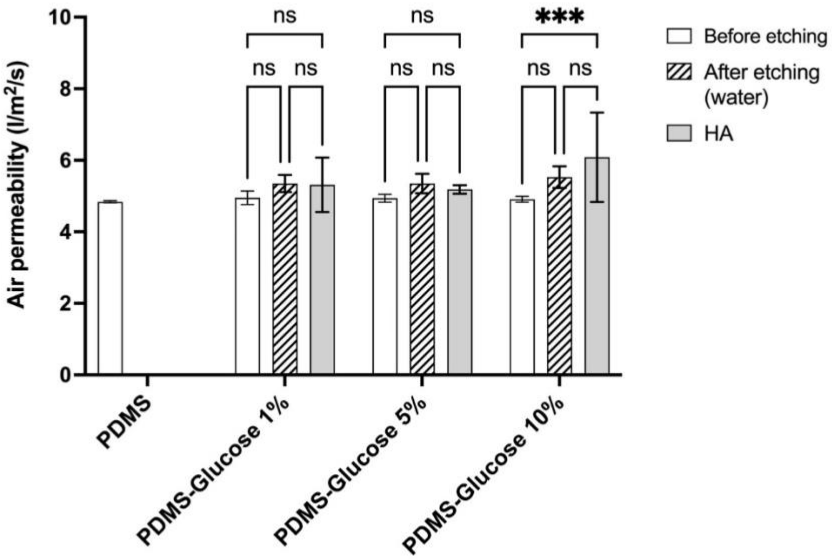

Figure 31: Air permeability of pure PDMS versus PDMS-Glucose membranes. Error bars represent SD. Symbology: * indicates significant differences between different treatment conditions in the same sample and *ns* means non-significant (n=5). 0.1234 (ns); 0.0332 (*), 0.0021 (**), 0.0002 (***), <0.0001 (****).

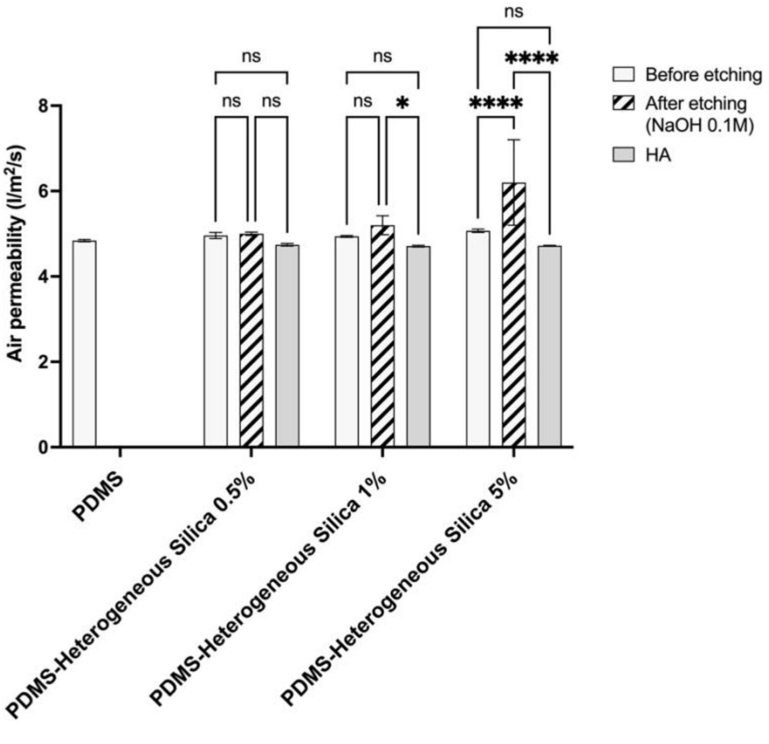

Figure 32: Air permeability of pure PDMS versus PDMS-Heterogeneous Silica membranes. Error bars represent SD. Symbology: * indicates significant differences between different treatment conditions in the same sample and *ns* means non-significant (n=3). 0.1234 (ns); 0.0332 (*), 0.0021 (**), 0.0002 (***), <0.0001 (****).

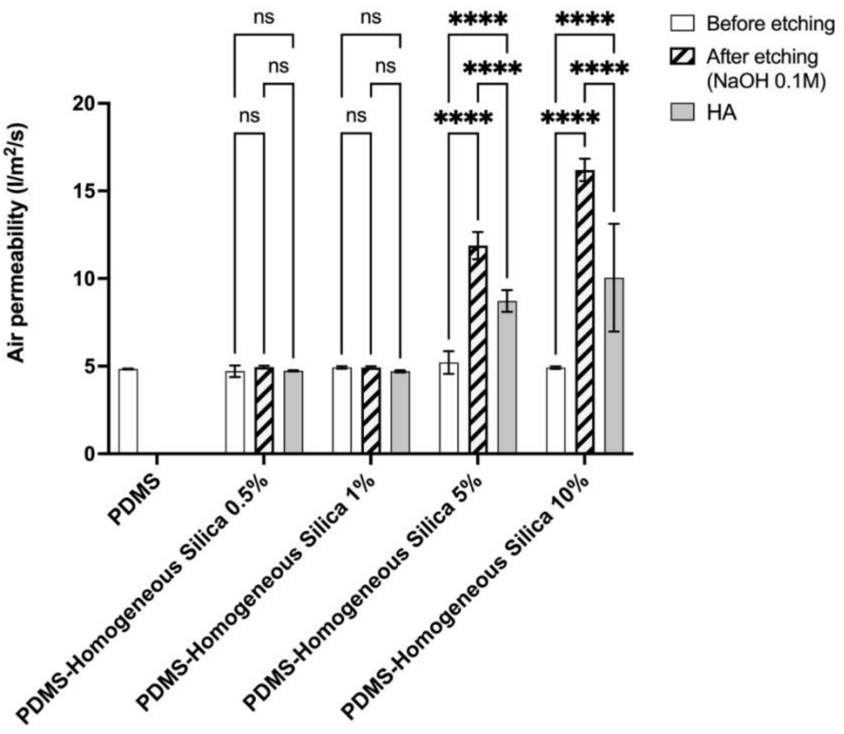

Figure 33: Air permeability of pure PDMS versus PDMS-Homogeneous Silica membranes. Error bars represent SD. Symbology: * indicates significant differences between different treatment conditions in the same sample and *ns* means non-significant (n=3). 0.1234 (ns); 0.0332 (*), 0.0021 (**), 0.0002 (***), <0.0001 (****).

After etching, the porogenic material is removed, so it is expected to leave exposed the porous network. Thus, leading to an increment in permeability in some membranes. Nevertheless, this phenomenon did not happen to the majority of the samples (Figure 31, Figure 32, and Figure 33). As can be observed, for instance, in glucose modified-PDMS samples, where there are no significant differences before and after etching, independently of the concentration of the porogenic material (Figure 31). The exceptions occurred to the membrane samples treated with Heterogeneous-Silica at concentrations of 5%, and Homogeneous-Silica at concentrations of 5% and 10%. However, when those samples are treated with HA, the air permeability of the PDMS membrane modified with Heterogeneous-Silica 5%, reaches a similar value to pure PDMS. Since the value of air permeability is expected to be proportional to the porous network, if the value is high, then the porosity of the sample is indicated to be high as well.

Thus, the PDMS membranes with higher porous density are the ones treated with Homogeneous-Silica at 5% and 10%, where even after HA treatment the air permeability shows a significant difference compared to pure PDMS.

This observation is also corroborated by the optical microscopy and SEM images, where these two samples showed a higher presence of porous in the PDMS MNs. Relatively to the effect of the HA solution on the air permeability, the majority of the results showed a non-significant difference before or after the HA treatment. However, due to the high viscosity of the HA solution, it was expected that in air experiments a slow decrease in permeability could be observed mainly caused by the obstruction of some porous with dried HA molecules.

3.4 WETTABILITY

The contact angles were measured in all the developed MNs samples before and after etching, and after treatment with HA.

The value of the contact angle varies from 0˚ to 180˚. Low contact angle (0˚ to 90˚) traduces on high surface energy, which means that the surface is hydrophilic. On the other hand, hydrophobic surfaces (90˚ to 180˚) have low surface energy [124]. As mentioned before, pure PDMS has in general a hydrophobic behavior.

Figure 34 illustrates the typical hydrophobic behavior observed during the contact angle experiments that were performed in this work. Also, it represents the challenge of measuring the contact angle onto the microneedles site (Figure 34A), due to the difficulty of establishing a good baseline on non-horizontal samples. Thus, the surface base of MNs arrays, which had the same treatment that the MN, was selected to perform these tests (Figure 34B).

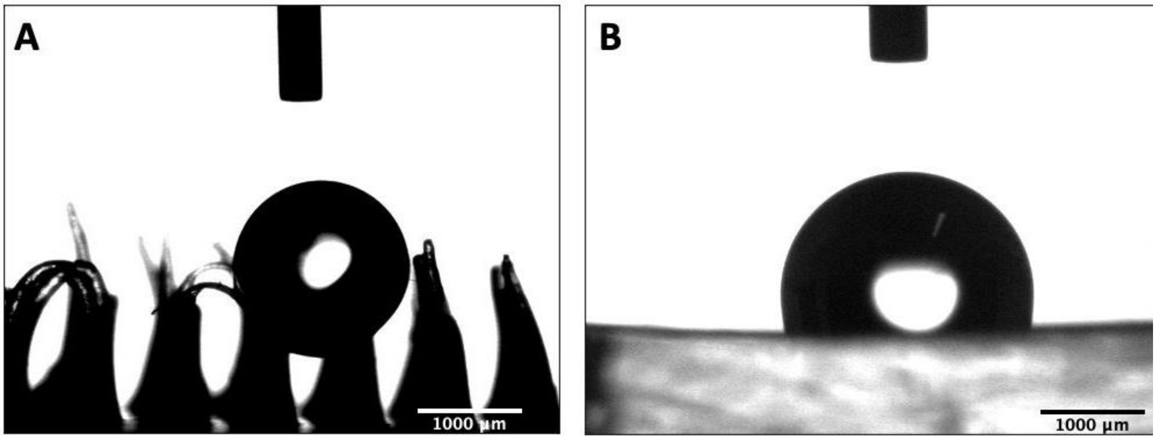

Figure 34: Contact angle of PDMS-Heterogeneous Si 0.5% (w/w) after etching. **A** MNs – tip surface, **B** MNs – base surface.

Typically, as aforementioned, PDMS exhibits hydrophobic behavior and poor wettability. The experimental contact angle of the pure PDMS (control) was calculated to be approximately 109.5˚, which is validated by the values found in the literature [125].

Figure 35 represents the measurements on PDMS-Glucose MNs. Before etching, the hydrophilic behavior of all PDMS-Glucose MNs is very similar in all tested concentrations, representing hydrophobicity (i.e., values higher than 90˚). Observing these results, the wettability values, before etching, are slightly higher than for pure PDMS, showing that adding glucose keeps the hydrophobic behavior. Then, after etching the contact angle decreases some 20˚, but still is in the hydrophobic range. Lastly, after treatment with HA solution, the contact angle decreases to values that indicate a behavior change to hydrophilic. From these samples, the most hydrophilic MNs are PDMS-Glucose 5% (w/w) after treatment with HA (i.e., 38.9˚± 8.1˚).

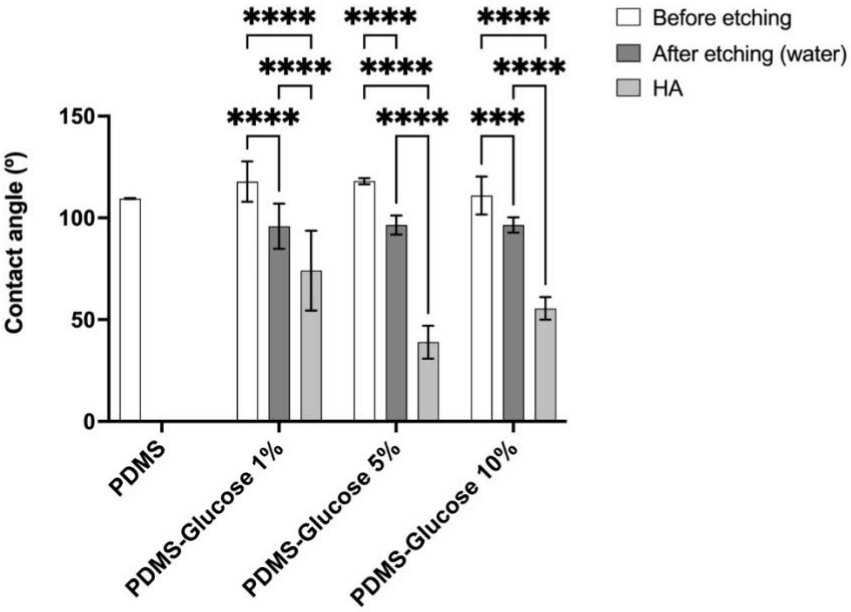

Figure 35: Wettability of pure PDMS versus PDMS-Glucose MNs. Error bars represent SD. Symbology: * indicates significant differences between different treatment conditions in the same sample (n=10). 0.1234 (ns); 0.0332 (*), 0.0021 (**), 0.0002 (***), <0.0001 (****).

Overall, all the samples, independently of the porogenic material tested, show before etching a hydrophobic behavior with a contact angle higher than 97° (Figure 35, Figure 36, and Figure 37), and therefore hydrophobicity. Particularly, PDMS-Glucose shows that hydrophobicity decreased after etching, which was also observed in samples of PDMS-Heterogeneous Silica (Figure 36). Similarly, with PDMS-Glucose MNs, the contact angle of PDMS-Heterogeneous Silica MNs decreases more after HA solution. Comparing the wettability results from PDMS-Glucose and PDMS-Heterogeneous Silica after HA treatment, the PDMS-Glucose MNs are more hydrophilic than PDMS-heterogeneous Silica MNs, but PDMS-Heterogeneous Silica MNs still are hydrophilic. The most hydrophilic PDMS-Heterogeneous Silica MNs are PDMS-Heterogeneous Silica 5 % (w/w) MNs, with a contact angle around 74°.

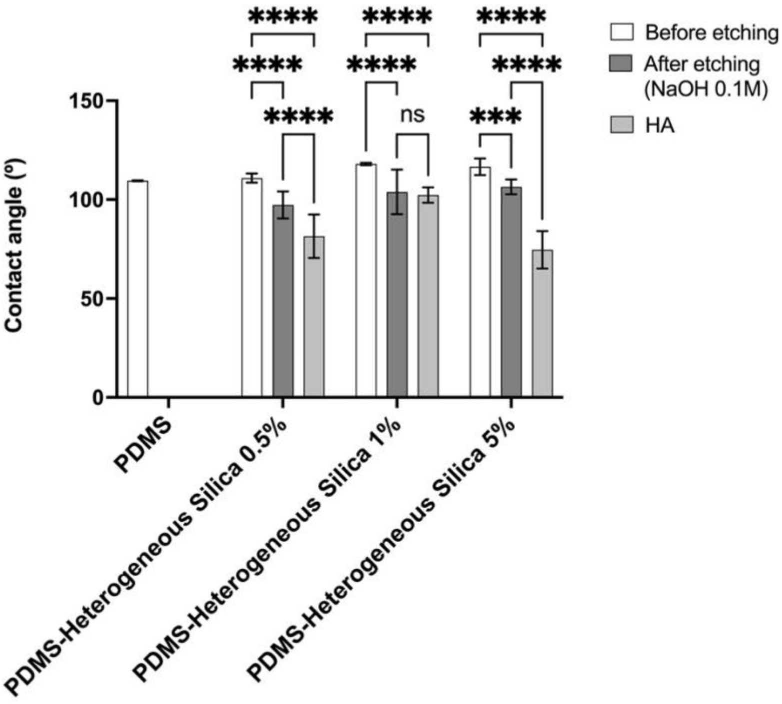

Figure 36: Wettability of pure PDMS versus PDMS-Heterogeneous Silica MNs**.** Error bars represent SD. Symbology: * indicates significant differences between different treatment conditions in the same sample (n=10). 0.1234 (ns); 0.0332 (*), 0.0021 (**), 0.0002 (***), <0.0001 (****).

On other hand, PDMS-Homogeneous Silica MNs increased hydrophobicity after etching, which was not expected (Figure 37). Ideally, to MNs be capable to collect cell culture media from the organ model, it is theorized that MNs need to be in a hydrophilic behavior with a contact angle no greater than 90˚. This is theorized since if MNs are too hydrophobic, biomarkers can be sequestered by PDMS, disallowing its detection, and monitoring downstream on the biosensing system.

However, after treatment with HA solution the PDMS-Homogeneous Silica MNs decreased their contact angle, a similar observation to the other modified-PDMS samples of MNs. However, for all the concentrations the value is around 90˚, which is borderline to what the minimum desired. Compared with all the other modified-PDMS MNs, PDMS-Homogeneous Silica MNs have a lower value of hydrophilicity even after HA solution, which means that an additional coating with HA or increment in the HA concentration treatment should be applied to achieve a better hydrophilic behavior.

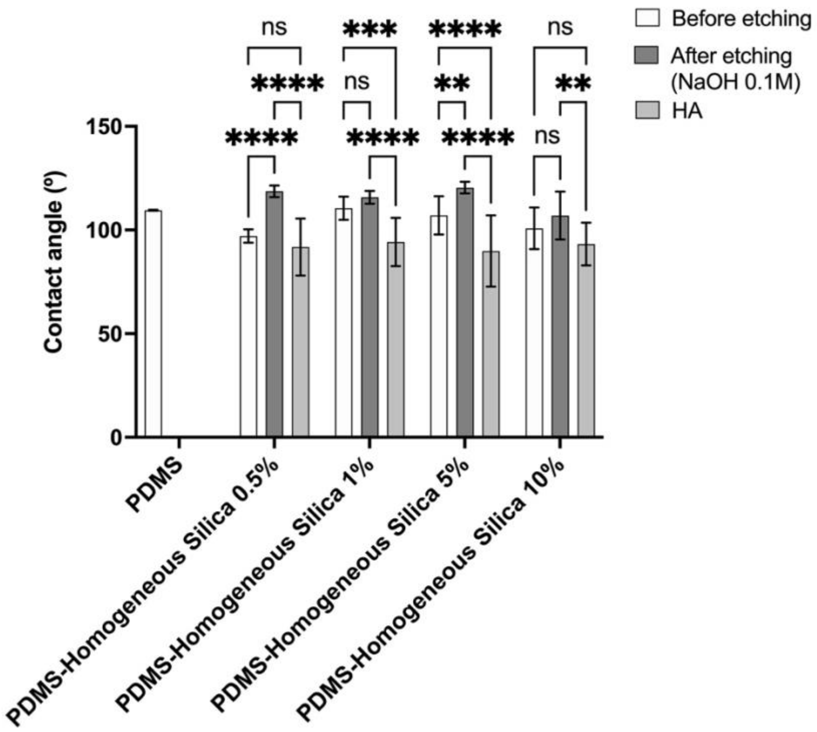

Figure 37: Wettability of pure PDMS versus PDMS-Homogeneous Silica MNs. Error bars represent SD. Symbology: * indicates significant differences between different treatment conditions in the same sample (n=10). 0.1234 (ns); 0.0332 (*), 0.0021 (**), 0.0002 (***), <0.0001 (****).

However, and surprisingly, during wettability measurements, an interesting phenomenon was observed on PDMS-Homogeneous Silica at 5% and 10% (w/w) after etching with NaOH, where the water drops showed a high attraction to the PDMS-treated surface. This electromagnetic attraction that was observed in these experiments, can be related to the so-called electroosmotic flow. Electroosmotic flow refers to the movement of liquid caused by an applied voltage across a porous material, capillary tube, membrane, microchannel, or any other fluid conduit [126]. In electrokinetic transport at the micro/nanoscale, electroosmotic flow, results from an electric field being applied to an electrolyte solution in the tangential direction of a charged surface.

To demonstrate this phenomenon, Figure 38A-D shows the observed typical behavior of water drops in contact with Silica modified-PDMS surfaces (before NaOH etching). Figure 38A and Figure 38E indicate the initial position and time (t=0). The water drop´s normal behavior is illustrated in Figure 38A-D, showing their closeness to the MN surface (Figure 38B and Figure 38C) until gentle landing on the modified-PDMS surface before NaOH etching treatment (Figure 38D).

Figure 38E-H shows the electroosmotic flow effect on the droplets of water that have been attracted to the modified-PDMS surface after 0.1 M NaOH treatment. Figure 38F shows a water drop reaching the surface, but instead of contacting it, the drop falls into the surface when it is close enough to be attracted to it (Figure 38G and Figure 38H). The effect was so strong that the time frames of the recorded video were too short to capture a defined image (Figure 38G).

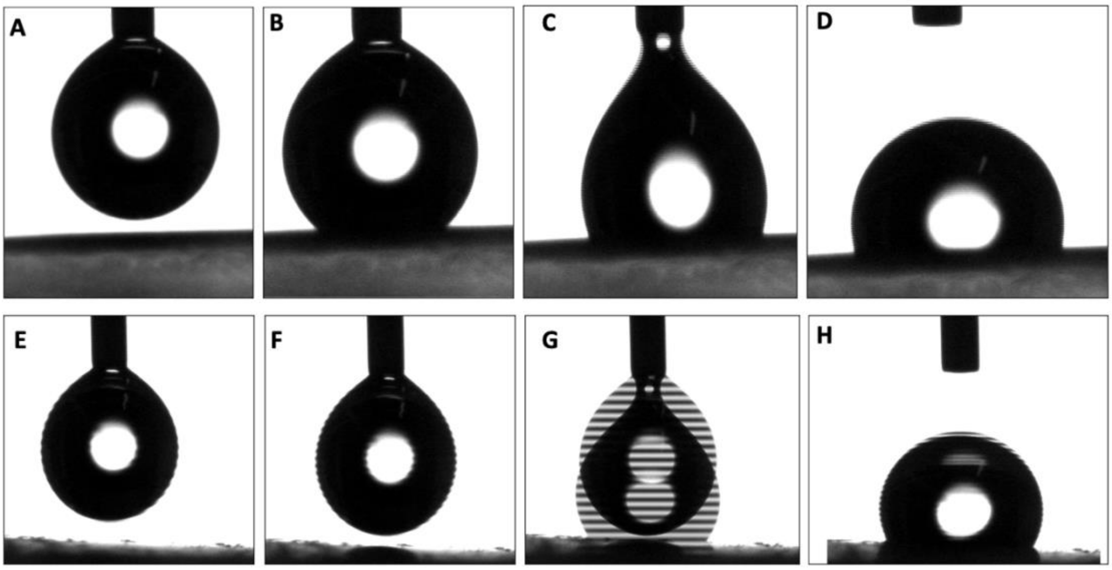

Figure 38: Behavior of water drops in contact with the Silica modified-PDMS surface before and after NaOH etching at 0.1 M. **A-D** Typical behavior in PDMS-Homogeneous Silica 5% (w/w) before etching, and verified in all the modified-PDMS MNs, **E-H** Water drops being electroosmotically attracted to the surface of PDMS-Homogeneous Silica 5% (w/w) after etching with 0.1 M NaOH.

To better understand the electroosmotic effect caused by the NaOH etching treatment on PDMS-Homogeneous Silica MNs, PDMS-Homogeneous Silica 10% (w/w) MNs with different concentrations of NaOH (i.e., 0.1 M, 0.5 M, and 1 M) were evaluated.

PDMS-Homogeneous Silica 10% (w/w) after etching with 0.5 M and 1 M of NaOH, show identical strong electroosmotic effects as described before (the same as observed with Silica at 5% after etching with 0.1 M NaOH), and illustrated in Figure 39. Interestingly, by increasing the concentration of Silica to 10% and using a NaOH solution at 0.1 M, the electroosmotic effect was weaker than the one observed with a concentration of Silica of 5%. This observation suggests that the electroosmotic effect of NaOH over the Silica modified-PDMS just happens if the NaOH concentration is in excess of the amount of Silica presented in the samples.

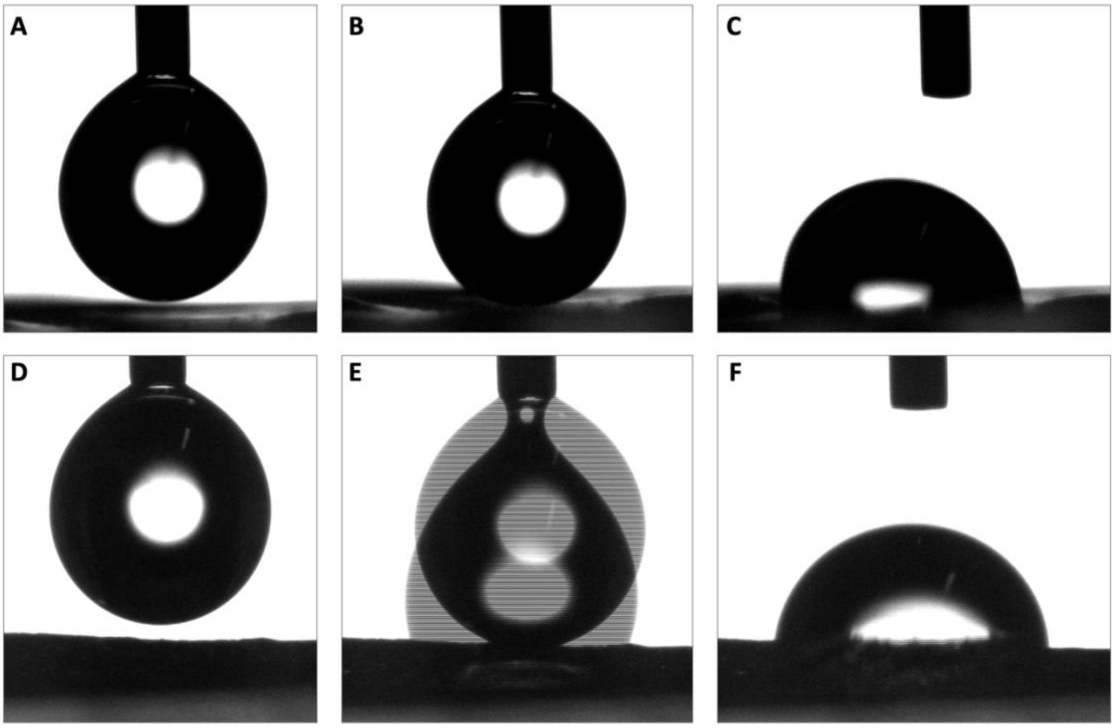

Figure 39: Behavior of water drops in contact with the PDMS-Homogeneous Silica 10% (w/w) surface after NaOH etching treatment. **A-C** PDMS-Homogeneous Silica 10% (w/w) after etching with 0.5 M of NaOH solution, **D-F** PDMS-Homogeneous Silica 10% (w/w) after etching with 1 M of NaOH solution.

Another interesting observation, illustrated in Figure 39, is that by increasing the concentration of NaOH the electroosmotic effect increase. However, the contact angle remains unaffected by the NaOH treatment as is possible to observe in Figure 40 and as previously described by Hoek et al., 2010 [127].

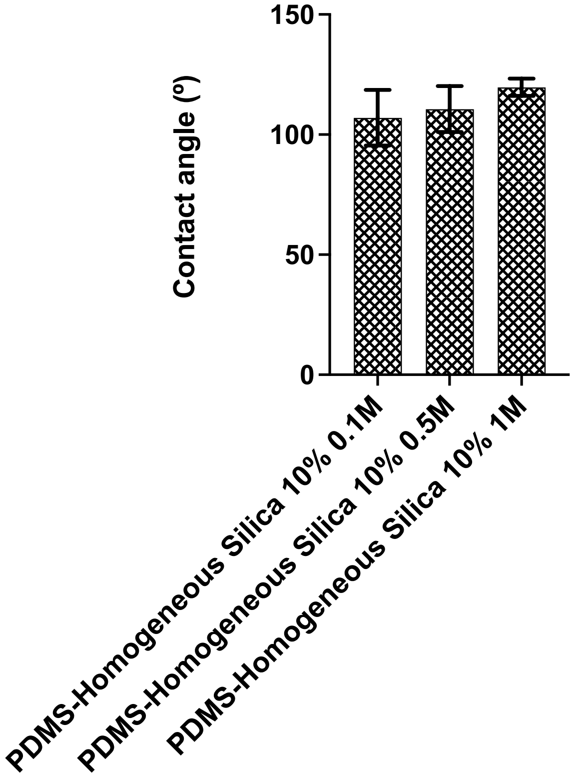

Figure 40: Wettability of PDMS-Homogeneous Silica 10% (w/w) MNs. Error bars represent SD.

For a better understanding of the effect of NaOH treatment over the Silica modified-PDMS, and its effect on the surface chemistry that leads to the electroosmotic flow phenomena, these samples were analyzed with SEM-EDS.

3.5 SEM-EDS ANALYSIS

The EDS experiments were performed to confirm the elemental composition of the modified-PDMS MNs.

Figure 41 depicts the chemical structures of pure PDMS, HA, and NaOH.

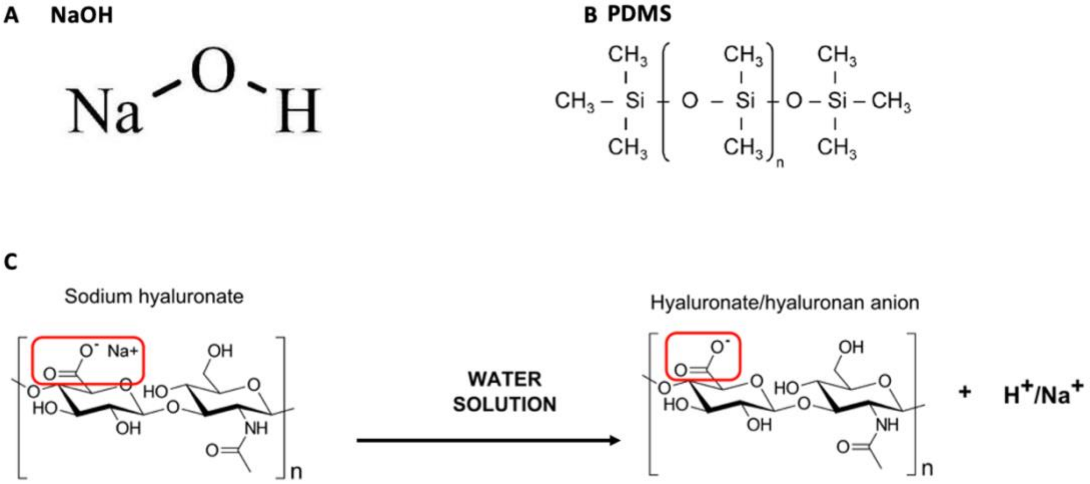

Figure 41: Chemical structures of **A.** NaOH, **B.** PDMS, and **C.** Sodium hyaluronate reaction with water.

The different EDS spectra obtained from all the MNs indicate an elemental composition of Si, C, and O (Figure 42). The specters presented in Figure 42, are a representation of the typical spectrum found in each type of porogenic sample, the rest of them are presented in Annex 2. The presence of another element as Cl, K, and Na in the sample PDMS-Glucose (Figure 42B), is mainly due to the non-deionized water used to wash the samples during etching. As a note, the presence of H cannot be evaluated within the technique used, since element H does not have a characteristic X-ray pattern. For this reason, the H element was not quantified.

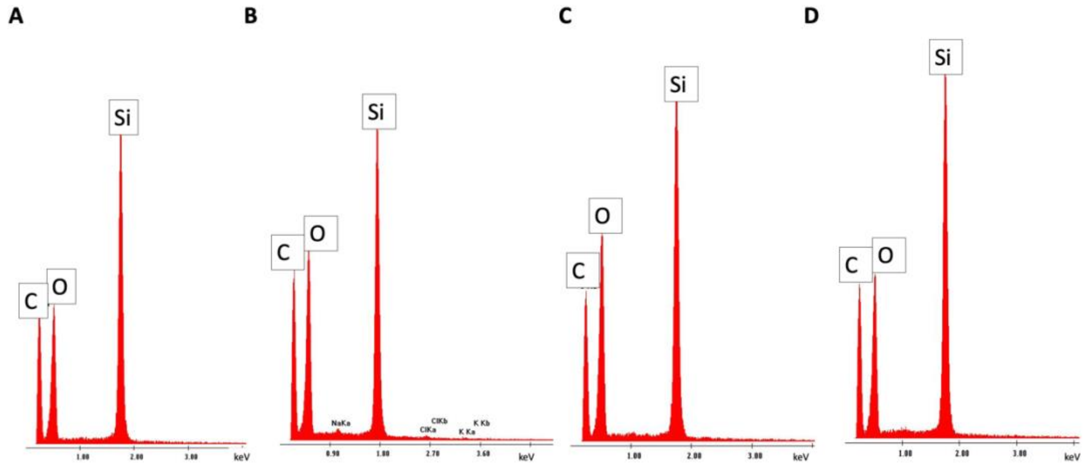

Figure 42: EDS Specters of **A** Pure PDMS MNs, **B** PDMS-Glucose 5% (w/w) MNs after etching with water, **C** PDMS-Heterogeneous Silica 5% (w/w), after etching with 0.1 M NaOH, **D** PDMS-Homogeneous Silica 5% (w/w), after etching with 0.1 M NaOH.

EDS allows a semi-quantitative analysis. The abscissa of the EDS spectrum indicates the ionization energy, and the ordinate indicates the counts. The higher the counts of a particular element, the higher will be its presence at that point or area of interest that was analyzed by EDS. Taking into consideration the Silica percentage on the studied MNs (Figure 43), it is possible to observe that after etching the samples modified with Silica particles, have a lower total Si percentage than pure PDMS-MNs. This can be partly explained by the effect that NaOH etching has on the Si group both Si -Nanoparticles and Si-PDMS [123].

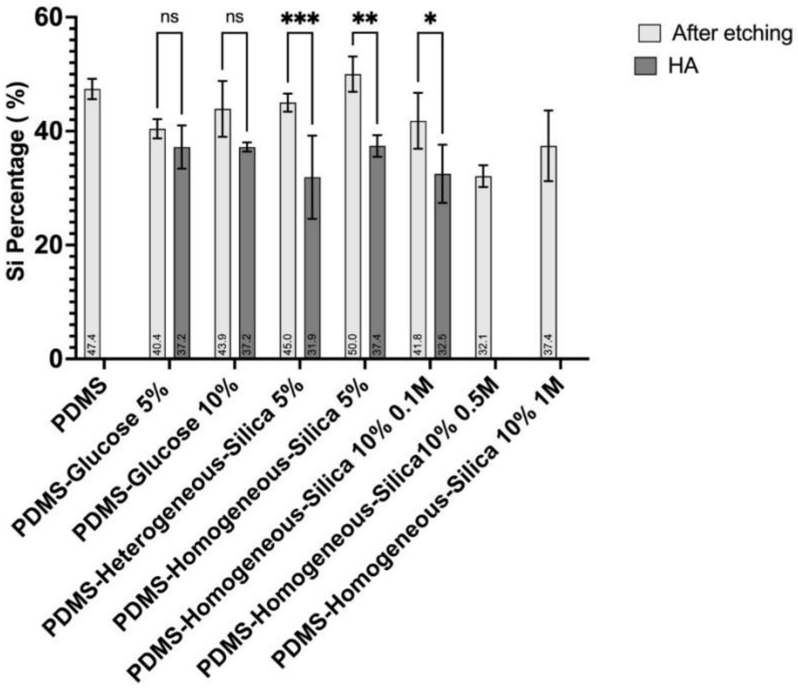

Figure 43: EDS analysis of elemental Si on MNs. Error bars represent SD (n=3). Symbology: * indicates significant differences between different treatment conditions in the same sample (n=10). 0.1234 (ns); 0.0332 (*), 0.0021 (**), 0.0002 (***), <0.0001 (****).

As discussed above, the effect of electroosmotic flow appears to be correlated with hydroxyl groups (-OH) created by the etching process with NaOH. Hence, it is expected that the MNs where the electroosmotic effect was observed will show more O in their composition than the other samples. Comparing PDMS-Homogeneous Silica 10 % (w/w) after etching at 0.1 M NaOH (Figure 44A), and after etching with 0.5 M and 1.0 M NaOH (Figure 44B), a high value of O composition is observed at these samples treated with a higher NaOH concentration (5).

This result suggests, as previously observed during the wettability experiments that increasing the concentration of NaOH will contribute not just to the removal of the incorporated Silica particles, but also to the modification of the surface chemistry of the MNs samples, meaning the Si molecules of PDMS. As observed by the lower percentage of elemental Si in the MNs treated with a higher concentration of NaOH (Figure 43). Thus, resulting in the sample with electroosmotic behavior. Also, the EDS results show that samples treated with HA have, in general, an increment in their O composition compared to the untreated, Figure 44D and Figure 45.

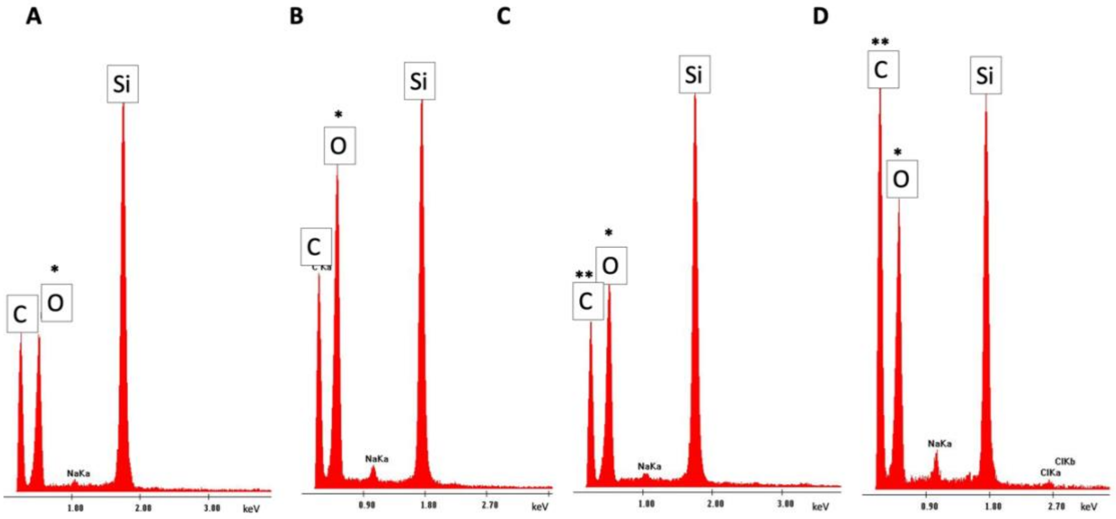

Figure 44: EDS specters of **A.** PDMS-Homogeneous Silica 10% (w/w) after etching 0.1 M NaOH, **B.** PDMS-Homogeneous Silica 10% (w/w) after etching 0.5 M NaOH, **C.** PDMS-Homogeneous Silica 5% (w/w) after etching 0.1 M NaOH **D.** PDMS-Homogeneous Silica 5% (w/w) after etching 0.1 M and treatment with HA. ***** and ****** represent the growth of carbon and oxygen pikes, respectively.

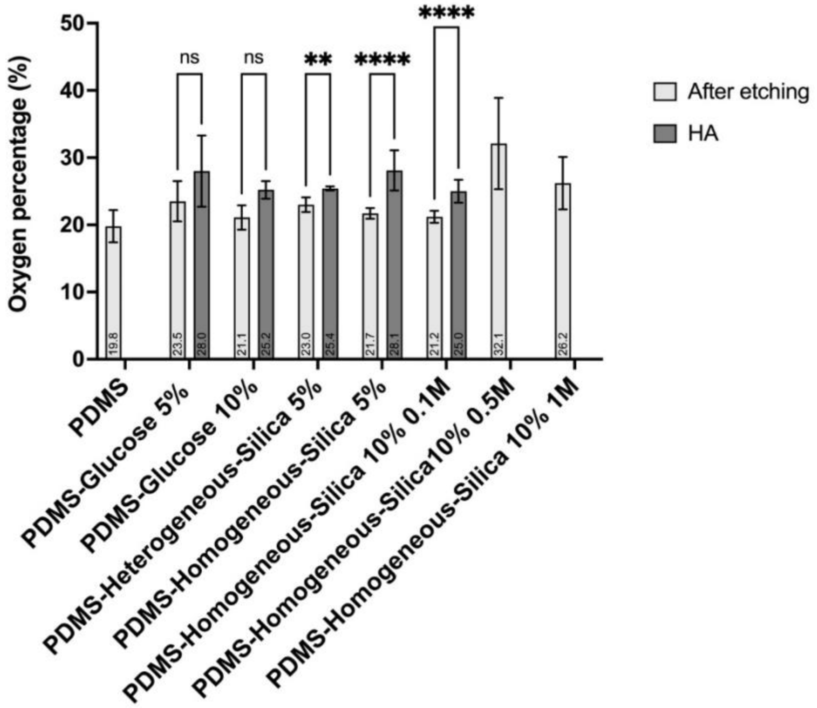

Figure 45: EDS Analysis of elemental O on MNs. Error bars represent SD (n=3). Symbology: * indicates significant differences between different treatment conditions in the same sample (n=10). 0.1234 (ns); 0.0332 (*), 0.0021 (**), 0.0002 (***), <0.0001 (****).

Overall, the main difference between before and after HA treatment is the increase in the C and O composition, as can be observed in Figure 44C and Figure 44D. Figure 46 shows that PDMS-Silica MNs after HA solution contains more C and O than MNs after etching. As a result, MNs treated with HA solution contain less Silica and more Oxygen and Carbon, resulting in a more hydrophilic surface.

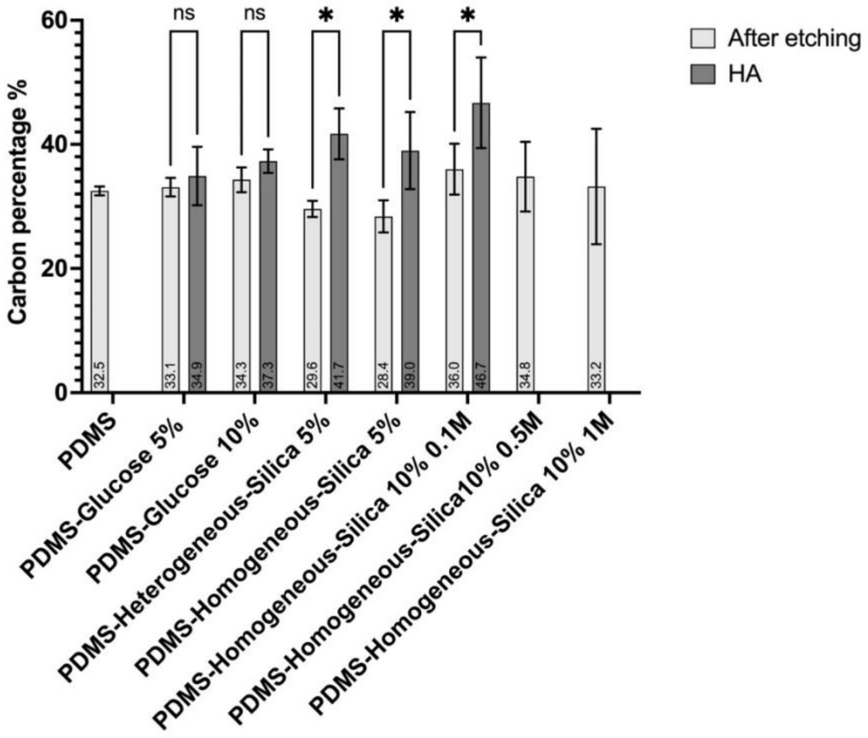

Figure 46: EDS Analysis of elemental C on MNs. Error bars represent SD (n=3). Symbology: * indicates significant differences between different treatment conditions in the same sample (n=10). 0.1234 (ns); 0.0332 (*), 0.0021 (**), 0.0002 (***), <0.0001 (****).

3.6 MECHANICAL CHARACTERIZATION

The relationship between force and displacement was found to be linear (the stress vs. strain plots are present in Annex 3). The Young's Modulus of each MNs was calculated for the linear elastic region (<20% strain). The values of the coefficient of correlation (R^2) are greater than 0.99 for all the microneedles, demonstrating the model's good accuracy.

The Young's modulus values are presented in Figure 47, Figure 48, and Figure 49. Figure 47 shows Young´s Modulus of PDMS-Glucose MNs. The experimental Young´s Modulus of PDMS was found to be 0.8 MPa, which is in line with the values found in literature [128].

However, PDMS-Glucose HA MNs failed to display the anticipated effect of HA. It was predicted that all the HA-treated samples would have a higher Young's Modulus. However, the mechanical properties of the MNs treated with HA and after etching are not significantly different or improved (Figure 47).

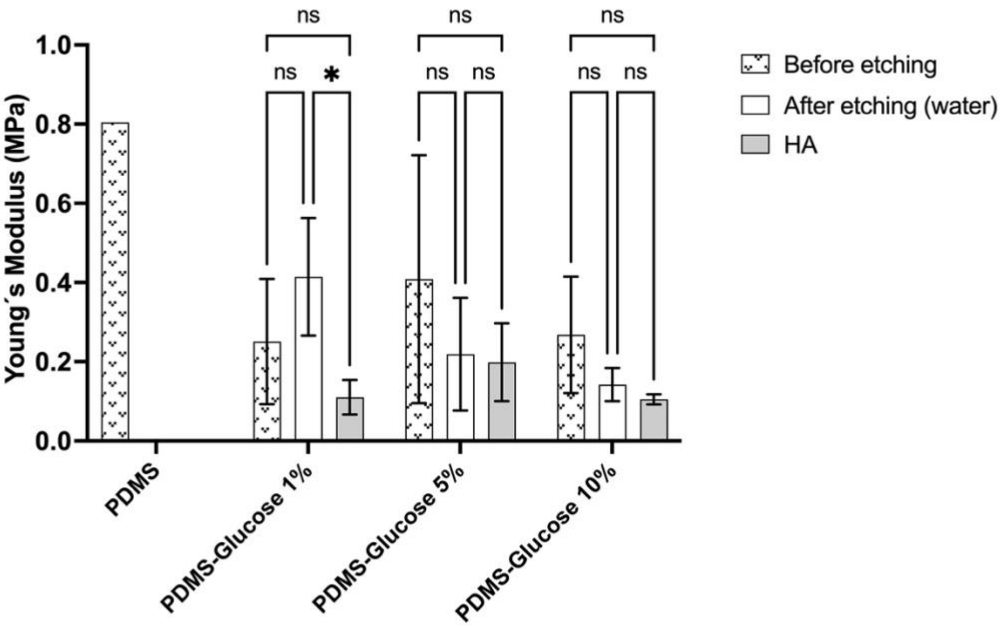

Figure 47: Young´s Modulus on PDMS-Glucose MNs. Error bars represent SD (n=3). Symbology: * indicates significant differences between different treatment conditions in the same sample (n=10). 0.1234 (ns); 0.0332 (*), 0.0021 (**), 0.0002 (***), <0.0001 (****).

Figure 48 shows the results of PDMS-Heterogeneous Silica MNs, where it is possible to observe the effect of HA, which increases the Young´s Modulus only at the PDMS-Homogeneous Silica 5% (w/w) treated with HA. In this case, the value increases almost 7 times compared to PDMS-Homogeneous Silica 5% (w/w) after NaOH etching treatment.

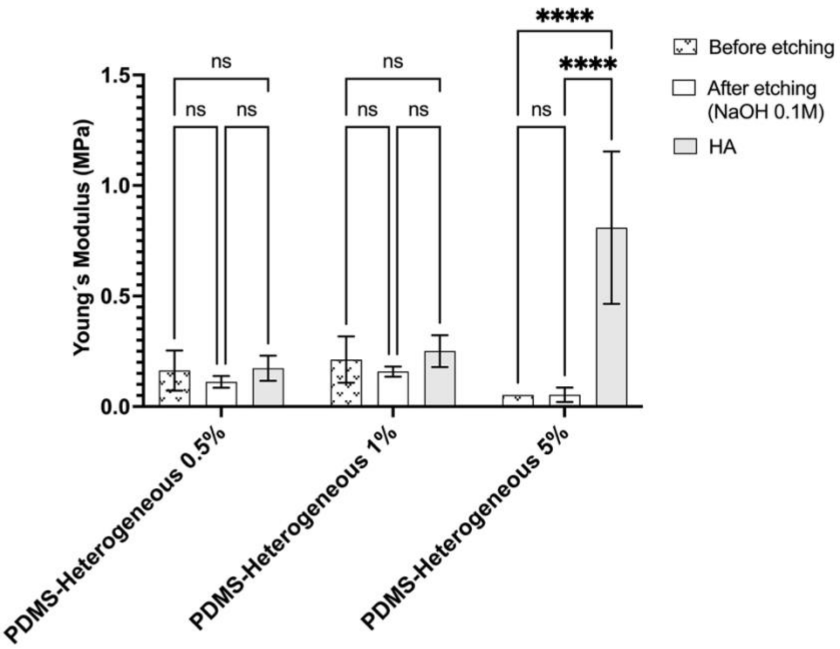

Figure 48: Young´s Modulus on PDMS-Heterogeneous Silica MNs. Error bars represent SD (n=3). Symbology: * indicates significant differences between different treatment conditions in the same sample (n=10). 0.1234 (ns); 0.0332 (*), 0.0021 (**), 0.0002 (***), <0.0001 (****).

PDMS-Homogeneous Silica MNs show the improvement in Young´s Modulus after HA treatment for PDMS-Homogeneous Silica 5% (w/w) MNs and PDMS-Homogeneous Silica 10% (w/w) MNs (Figure 49). Therefore, it appears that modified PDMS with a higher concentration of Silica nanoparticles allows better diffusion of the HA molecules into their cast porous and thus, an improvement in the strengthening of the mechanical behaviors. From these results, we theorize that samples with a higher density of pores and interconnectivity allow a better diffusion and treatment with the HA solution, which overall will improve their mechanical strength.

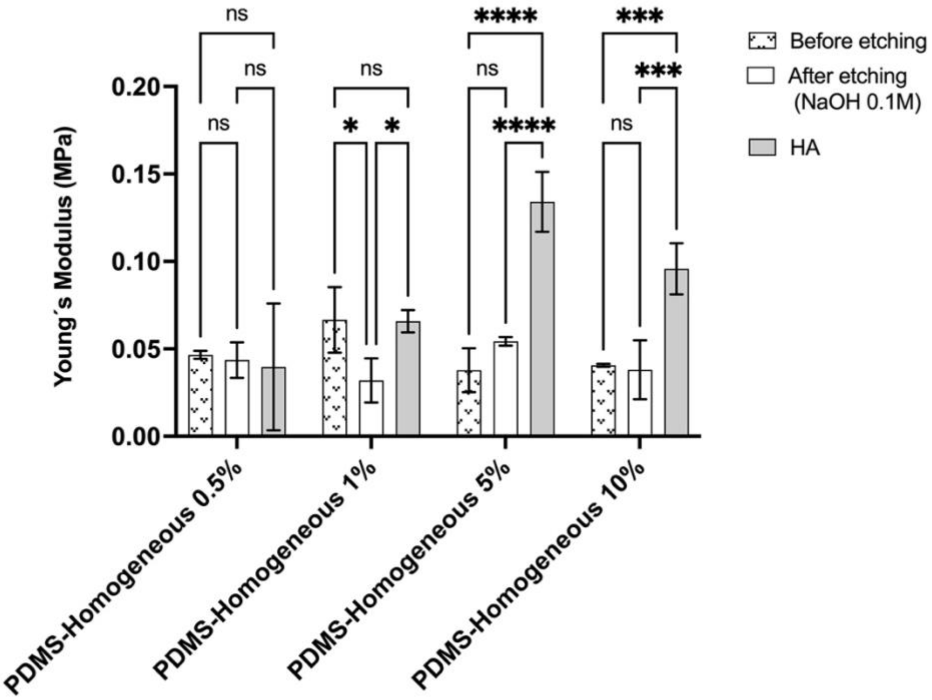

Figure 49: Young´s Modulus on PDMS-Homogeneous Silica MNs. Error bars represent SD (n=3). Symbology: * indicates significant differences between different treatment conditions in the same sample (n=10). 0.1234 (ns); 0.0332 (*), 0.0021 (**), 0.0002 (***), <0.0001 (****).

3.7 POROSITY

The porosity percentage of the MNs was assessed after etching and presented in Figure 50. In addition, to ensure that HA had no impact on porosity, MNs samples were also analyzed after HA treatment (data available in Annex 4).

As observed in Figure 50, in general, the porosity rises when the concentration of the porogen agent in PDMS MNs increases as well. The only exception happened to samples prepared with Glucose. The explanation that can be theorized is the fact that the used Glucose reagent, has a high range of particle size, which reaches sizes around 3000 nm and can block the entrance of the smaller Glucose particles into the MN mold.

Nevertheless, the obtained results show great potential when compared to some published works in the literature. For instance, Yi et al., 2021, developed aptamer-decorated porous MNs arrays with 13% of porosity that possess great potential for non-invasive extraction and detection of biomarkers in clinical applications [129]. Additionally, according to a prior report, 60% is the optimal value of porosity for ISF extraction [130]. In this work, higher values above 60% porosity were found in samples PDMS-Heterogeneous Silica 1% (w/w) MNs, PDMS-Heterogeneous Silica 5% (w/w) MNs, PDMS-Homogeneous Silica 1% (w/w) MNs, PDMS-Homogeneous Silica 5% (w/w) MNs, and PDMS-Homogeneous Silica 10% (w/w) MNs. Overall, the highest value of porosity was found in sample PDMS-Homogeneous Silica at 10% (w/w).

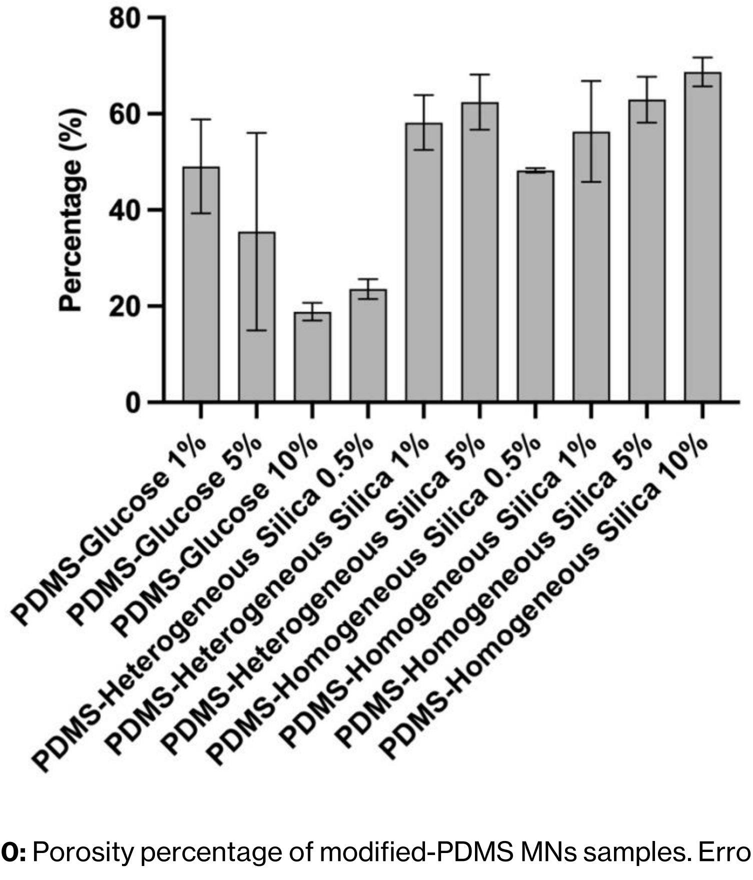

Figure 50: Porosity percentage of modified-PDMS MNs samples. Error bars represent SD (n=3).

3.8 SWELLING

The swelling and swelling profiles were examined to characterize the capacity of MNs to absorb liquids. It is well established that PDMS is mostly permeable to water, due to its hydrophobicity, Reaching only 10% of swelling capability or lower.

To analyze swelling results several time points were taken. In general, after 120 min all the samples reached a plateau, suggesting the stabilization of their swelling capability. Thus, for comparison, the results obtained for the different modified-PDMS MNs will be discussed based on this timepoint (120 min).

After etching, and as expected, the swelling capability increases for all the MNs (Figure 51A, Figure 52A, and Figure 53A), when compared to pure PDMS (approx. 10%). Excitingly, samples treated with Homogeneous Silica at 10%, reach the highest swelling value of around 75%, which is 7.5 times higher than pure PDMS (10%), Figure 53A.

However, the results were somehow unexpected, since it was theorized that by increasing the concentration of the porogenic material in the PDMS MNs, the swelling capability would be increased as well. For instance, PDMS-Glucose 1% and 5% (w/w) MNs showed equally the highest swelling values within the PDMS-Glucose MNs, which is in line with the previous results obtained for their similar pore density (Figure 51). Also, in samples treated with Heterogeneous Silica, the effect of increasing the concentration of the porogenic material had, in general, no positive effect on the improvement of the MNs swelling (Figure 52). The exception happened in the samples treated with Homogeneous Silica, where it is observed that by increasing the concentration of the nanomaterial, the swelling capability is improved in a dependent way (Figure 53).

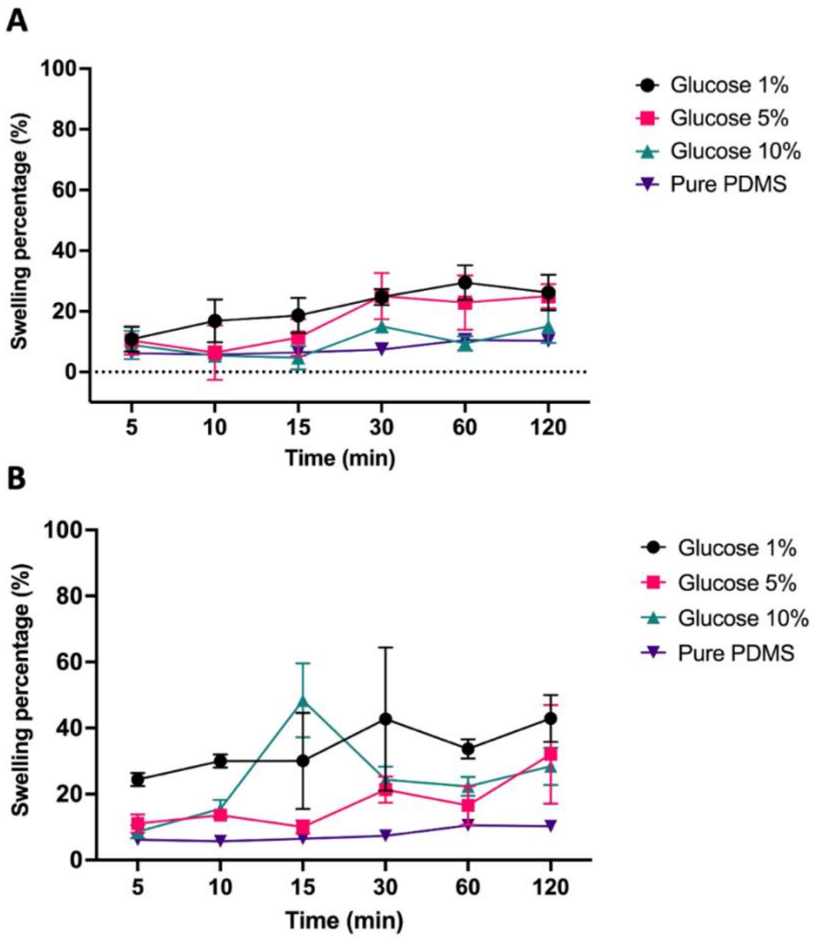

Figure 51: Swelling of PDMS-Glucose MNs and pure PDMS. **A** PDMS-Glucose MNs after etching, **B** PDMS-Glucose MNs after treatment with HA solution. Error bars represent SD (n=3).

After the HA treatment, the increment in the swelling capability is not always observed (Figure 51B, Figure 52B, and Figure 53B). Some examples are the MNs containing PDMS-Homogeneous Silica 10% (w/w), PDMS-Heterogeneous Silica 1% (w/w), and PDMS-Heterogeneous Silica 5% (w/w). In these cases, swelling is slightly lower than the one obtained after the etching treatment. Based on these results, it can be theorized that although the HA was an important effect in the strengthening of the mechanical properties of the MNs, their macromolecules can block some of the smaller porous and thus, prevent the passage of fluid (as in the cases of MNs treated with Silica vs. Glucose). To better understand this phenomenon, additional swelling tests have to be performed in a near future, where the time of incubation will be increased until a more constant swelling plateau is reached.

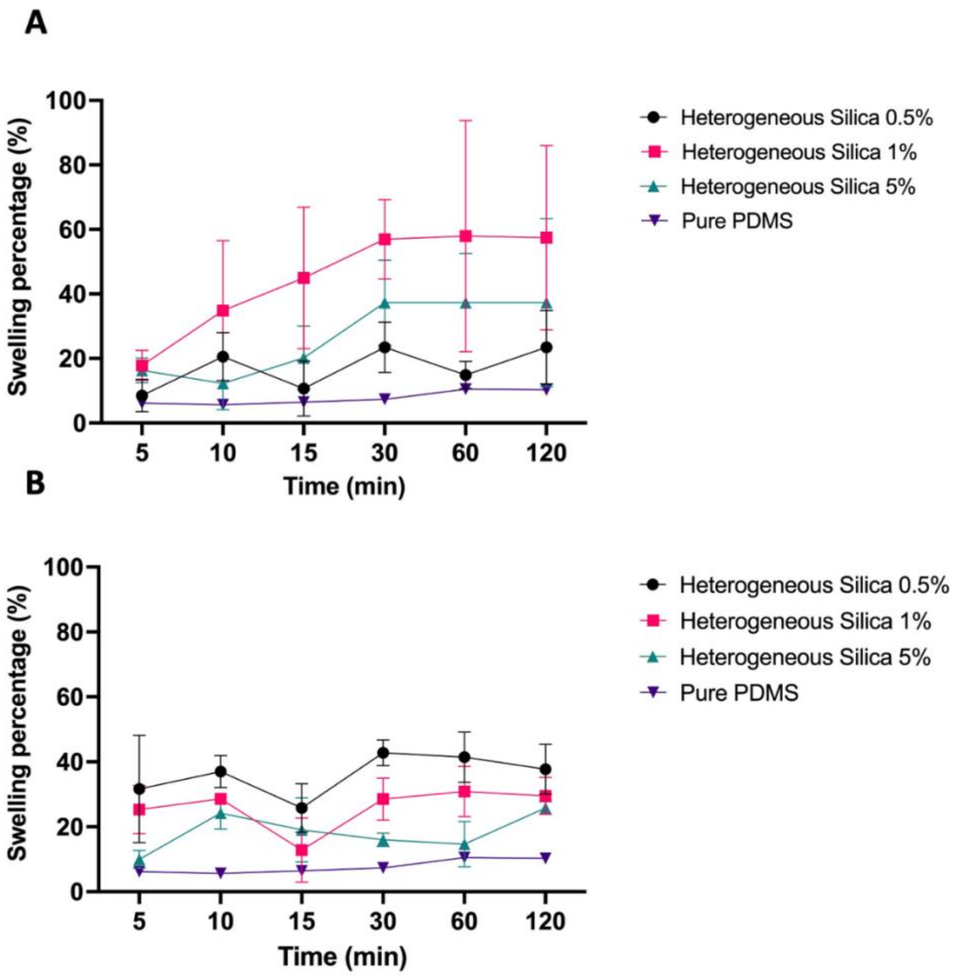

Figure 52: Swelling of PDMS-Heterogeneous Silica MNs and pure PDMS. **A:** PDMS-Heterogeneous Silica MNs after etching. **B:** PDMS-Heterogeneous Silica MNs after treatment with HA solution. Error bars represent SD (n=3).

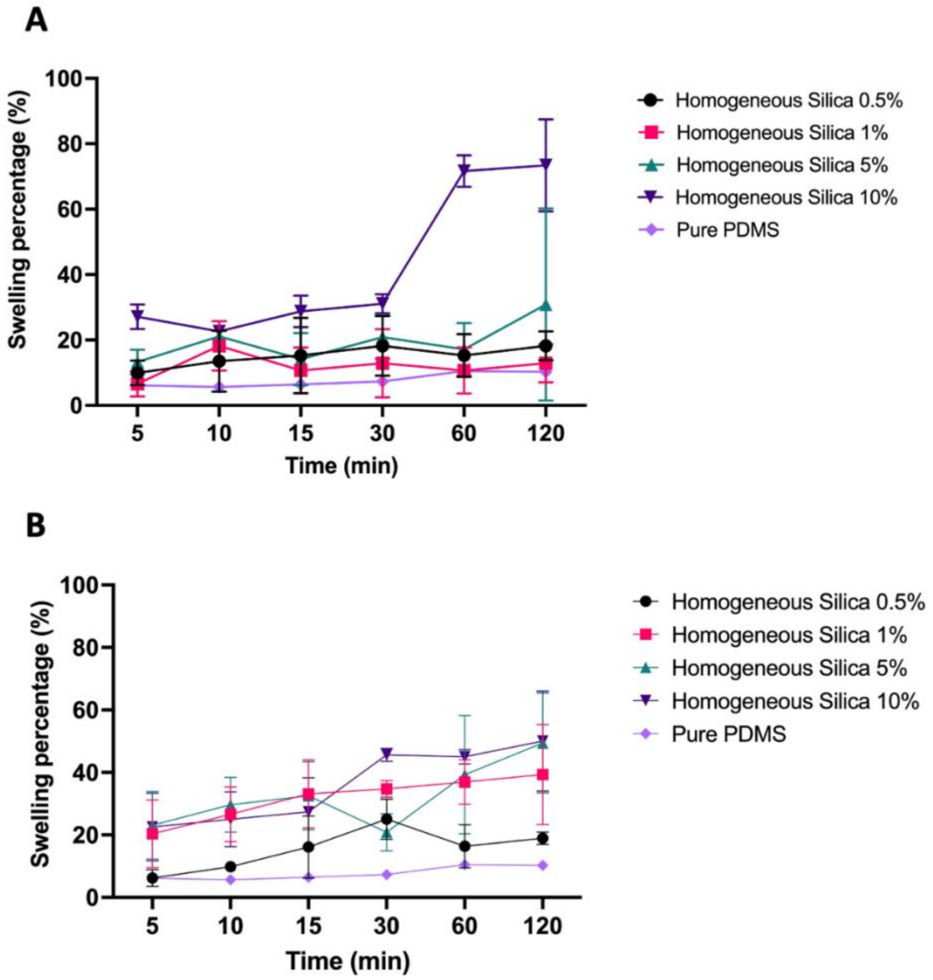

Figure 53: Swelling of PDMS-Homogeneous Silica MNs and pure PDMS. **A:** PDMS-Homogeneous Silica MNs after etching. **B:** PDMS-Homogeneous Silica MNs with HA solution. Error bars represent SD (n=3).

4. CONCLUSIONS AND FUTURE WORK

OoC are novel advanced microfluidic devices that combine the integration of engineered miniatured organ models with lab-on-a-chip technologies, with the potential to substitute what is considered gold standard models (i.e., 2D/3D static culture cells and animal models). However, to achieve end-use applicability and acceptance, these advanced microfluid devices need to improve their robustness and reproducibility, especially their ability to monitor the performance of the biomodels in real time. For that, micro(bio)sensors are being developed to be integrated, which requires new technologies and engineering solutions.

With this goal in mind, this master project aimed to develop porous MNs able to collect cell culture media, which will be in the future used to analyze the OoC performance, using micro(bio)sensors, in real-time.

For that, PDMS porous MNs with tunable porosity were envisioned to be fabricated using a low-cost casting method of porogenic materials. To create PDMS porous MNs, three porogenic materials were tested, namely organic Glucose, and inorganic Silica, with homogenic and heterogenic sizes. Using these porogenic materials, different concentrations were tested, as well as the effect of the concentration of NaOH as an etching solution, which resulted in several formulations that were deeply characterized regarding their porogenic size, density, mechanical strength, surface chemistry, and swelling, among others.

Porosity, pore size, density, air permeability (to analyze their porous network), and swelling capability, were all analyzed to determine the potential of the developed porous MNs to serve as a sponge of fluid and biomolecules released by the biomodels.

Based on these characterizations, it was found that porous MN samples created with Silica at the highest concentrations in the study (5% and/or

10%), and here denominated as PDMS-Heterogeneous 5% MNs and PDMS-Homogeneous 5% and 10% MNs, produced the best-combined results.

Comparing all the modified-PDMS MNs samples, PDMS-Homogenous Silica MNs with higher concentrations exhibit the best-combined performance (best outcomes of porosity, air permeability, mechanical proprieties, swelling capability) to work as porous MNs.

Since the mechanical strength of porous PDMS is in general too weak for the application envisioned, in this work, a treatment of HA to improve its mechanical strength was applied. Overall, after the HA treatment, the results show that mechanical strengthening was only achieved in the PDMS-Silica MNs at 5% and 10%. This can be theorized with the higher percentage and interconnectivity of porous on these samples that allow a better diffusion of these viscoelastic molecules along the porous PDMS network.

Additionally, the water contact angle was measured to evaluate the hydrophobic/hydrophilic behavior of the modified-PDMS MNs. Results show that, in general, the etching treatment (with water or NaOH) does not improve the hydrophilicity of the samples (which maintains the hydrophobic behavior of PDMS). However, those samples turn hydrophilic after being treated with HA solution, which is necessary to reduce the fouling of proteins by PDMS, which can impact the number of biomarkers that will reach the biosensor. This change in hydrophilicity caused by the HA treatment was validated by the EDS analysis, where a higher percentage of O and C were determined on the samples treated with HA.

Along this study, it was observed that samples treated with NaOH create an electroosmotic effect on the modified-PDMS samples. To better understand this phenomenon, samples of homogeneous silica at 10% were fixed to produce the porous PDMS MNs, while varying NaOH solutions between 0.1, 0.5, and 1 M, as an etching solution. The overall results show that NaOH concentration does not significantly affect the amount or dimension of micropores, but influences the surface chemistry of the samples, especially by decreasing the percentage of the elemental Si and increasing the percentage of O. This increase in O appears to be correlated with creation of surface hydroxyl groups (-OH), correlated with the observed electroosmotic effect.

In the master project's main objective was successfully achieved with the creation of a low-cost protocol to produce a porous PDMS array of MN with the characteristics necessary to work as a sponge of fluids and biomolecules. Although the interesting results, especially the one obtained with samples of homogenous silica at 10%, the results show that some improvements can be done in the future to increase the swelling capability of these samples. Therefore, the optimization steps can be achieved with the increment of the silica concentration, such as 15%, 20%, or even higher percentages. This could allow the casting of even more micropores into the MN, creating a better interconnected porous network. Thus, increasing the swelling capability. Also, some apparent clogging was observed on the samples obtained with silica nanoparticles after the HA treatment (molecular size between 1000-4000 KDa), shown by the slight decrease in swelling capability. It is theorized that if we increase the size of homogenous silica nanoparticles to values around 300-400 nm, this clogging effect will be minimized. Avoiding some trapping of biomolecules with higher molecular sizes, such as the case of HA or others. Nevertheless, in the near future, it would be interesting to start testing the integration of the developed MNs on the microfluidic device, which will serve as a vascular system holder to guide the fluids to be analyzed in the biosensing platform (also in development). Therefore, future work needs to be centered on designing and fabricating the microfluidic device and bonding it to the porous PDMS MNs, using standard techniques such as plasma bonding.

Finally, the electroosmotic effect caused by the NaOH treatment can be studied in more detail, as it appears to have advantages in the swelling, and driving of media in a non-mechanical way to the biosensing system module.

5. ANNEX

Annex 1: Number and dimensions of Pores of MNs after etching and HA solution.

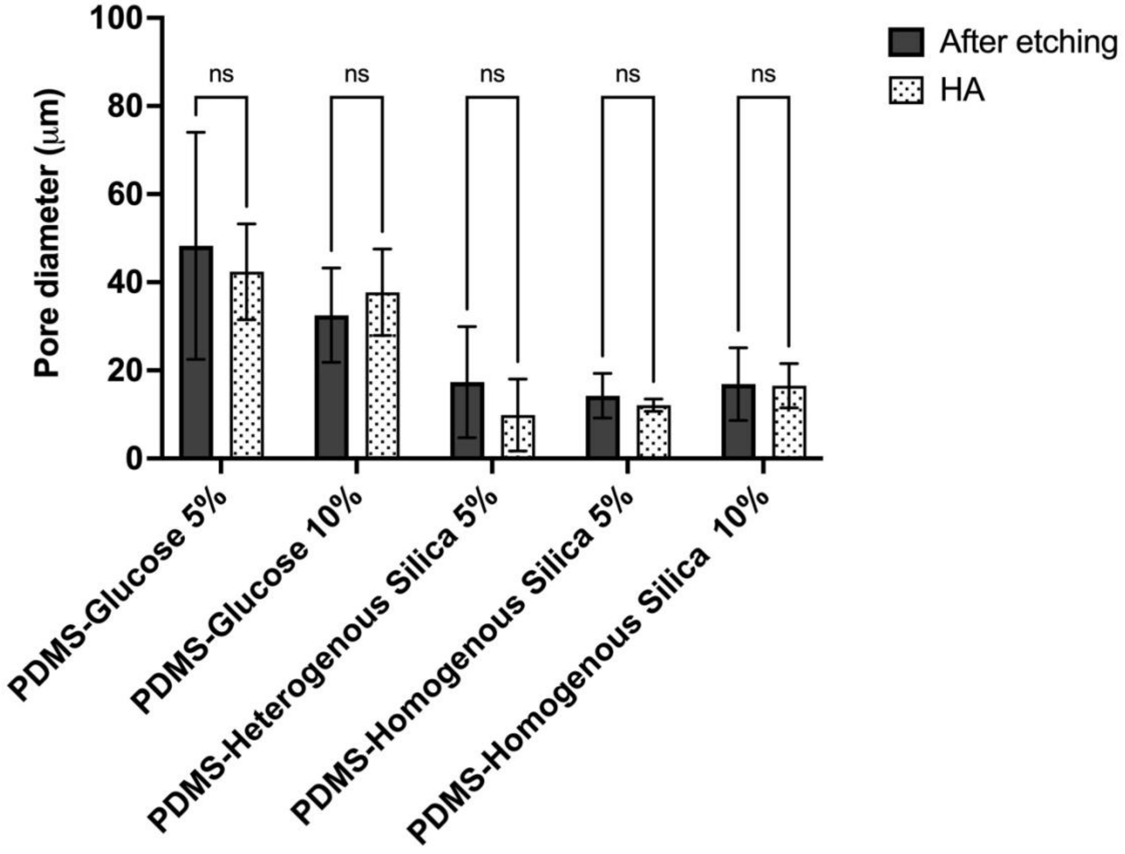

Figure A1.1: Dimension of pores in MNs. Error bars represent SD (n=3). Symbology: * indicates significant differences between different treatment conditions in the same sample and ns means non-significant (n=5). 0,1234 (ns); 0,0332 (*), 0,0021 (**), 0,0002 (***), <0,0001 (****).

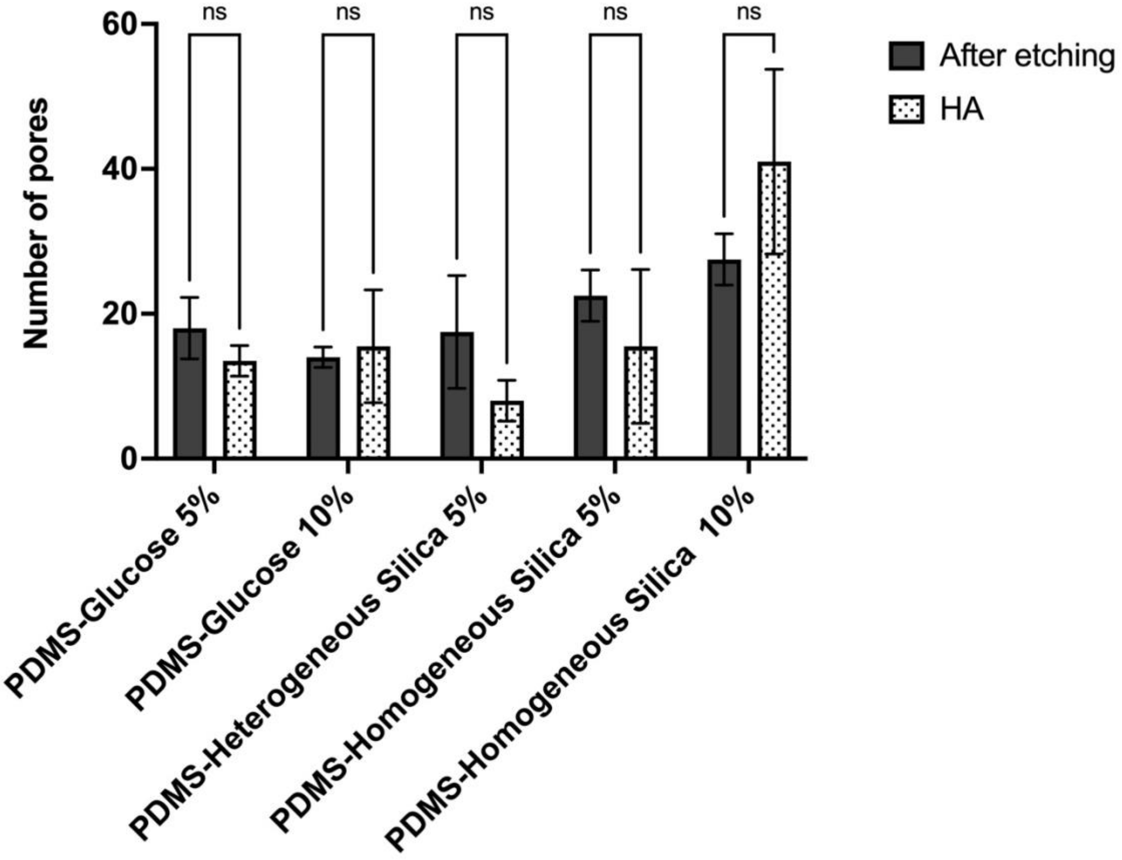

Figure A1.2: Number of pores in MNs. Error bars represent SD (n=3). Symbology: * indicates significant differences between different treatment conditions in the same sample and ns means non-significant (n=5). 0,1234 (ns); 0,0332 (*), 0,0021 (**), 0,0002 (***), <0,0001 (****).

Annex 2: EDS specters

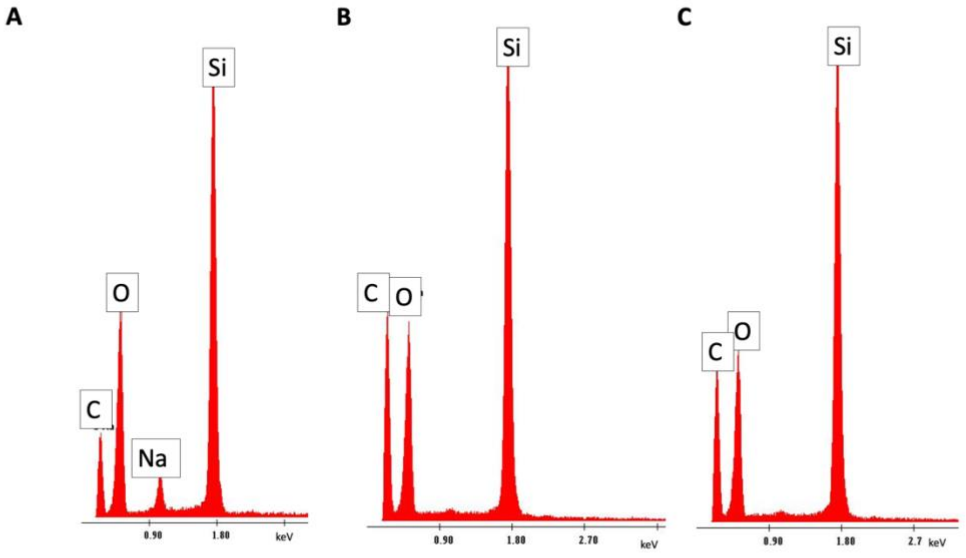

Figure A2.1: EDS Specters of **A.** PDMS-Glucose 10% (w/w) MNs after etching with 0.1M NaOH **B.** PDMS-Glucose 10% (w/w) MNs after etching with 0.1M NaOH and HA solution, **C:** PDMS-Glucose 5% (w/w) MNs after etching with 0.1M NaOH and HA solution.

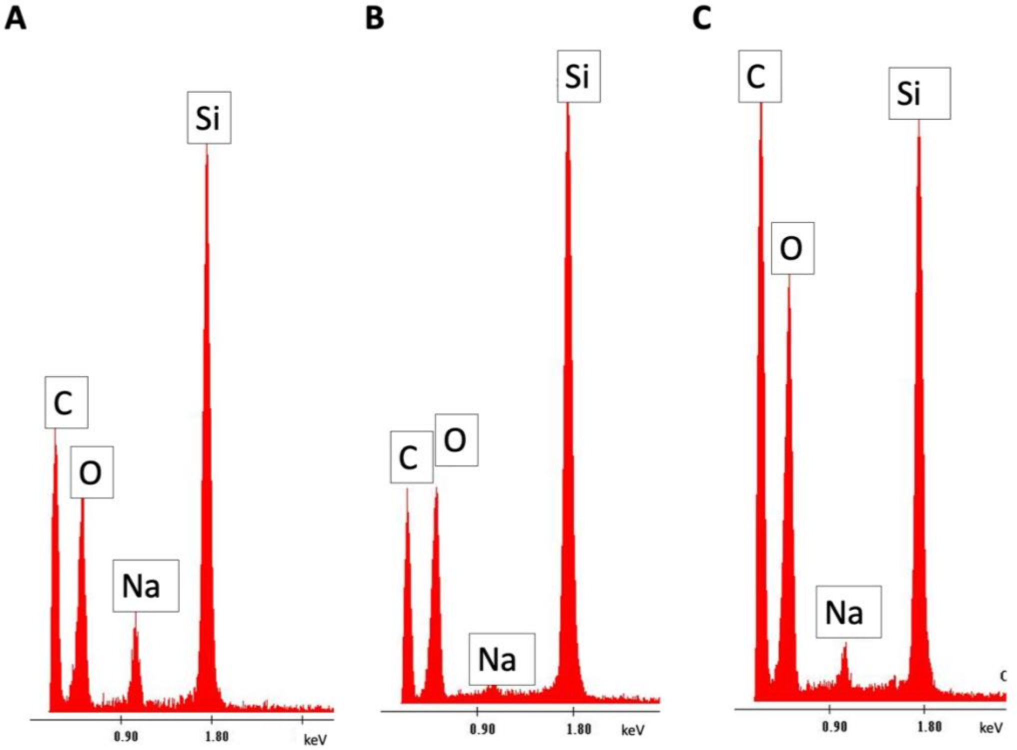

Figure A2.2: EDS Specters of **A.** PDMS-Homogeneous Silica 10% (w/w) MNs after etching with 1M NaOH **B.** PDMS-Homogeneous Silica 10% (w/w) MNs after etching with 0.1M NaOH and HA solution, **C:** PDMS-Heterogeneous Silica 5% (w/w) MNs after etching with 0.1M NaOH and HA solution.

Annex 3: Stress versus Strain plots

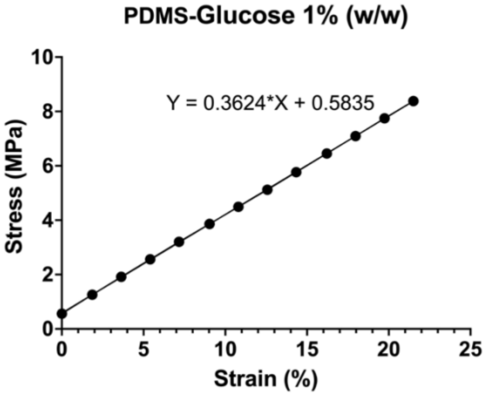
PDMS-Glucose 1% (w/w)

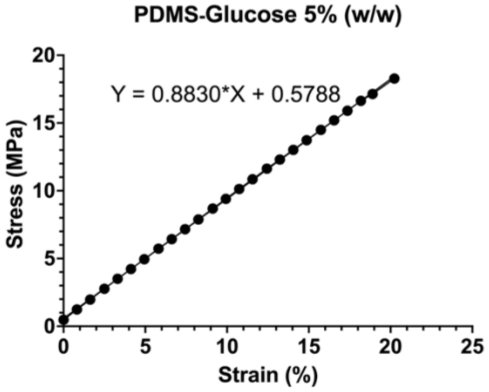
PDMS-Glucose 5% (w/w)

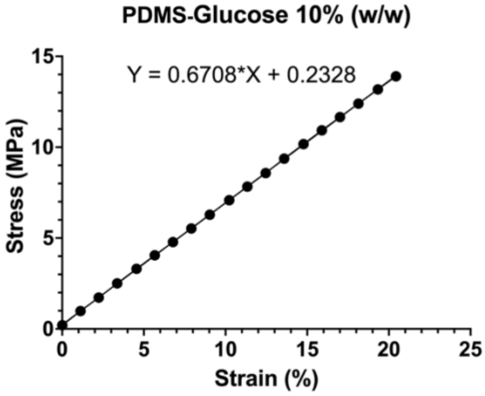
PDMS-Glucose 10% (w/w)

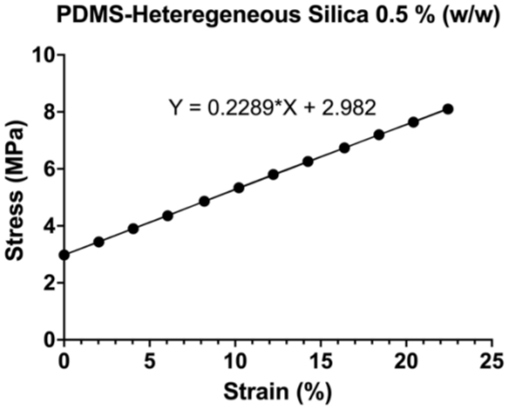
PDMS-Heteregeneous Silica 0.5 % (w/w)

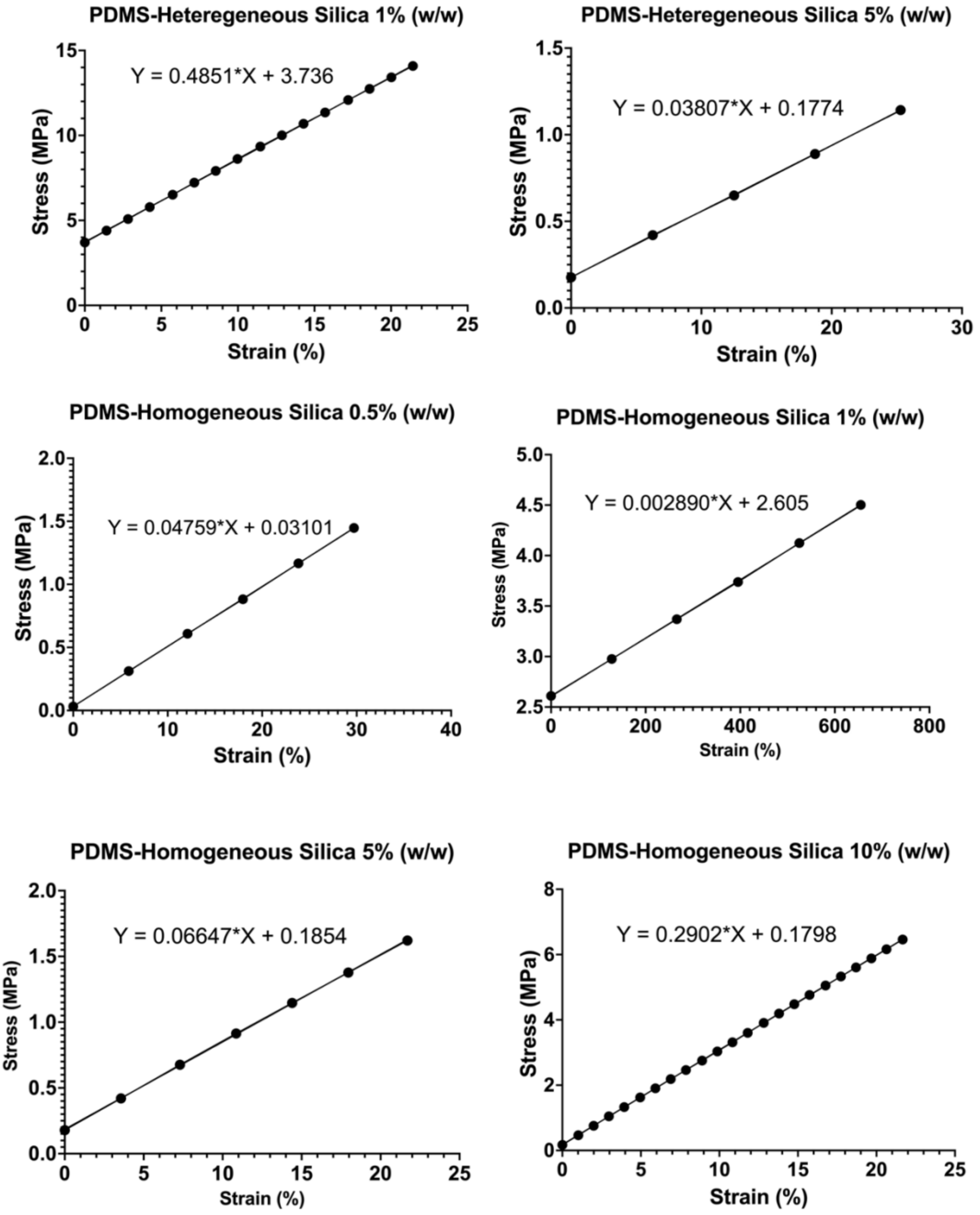

Figure A3.1: Stress versus Strain plots and trendlines (examples) before etching MNs.

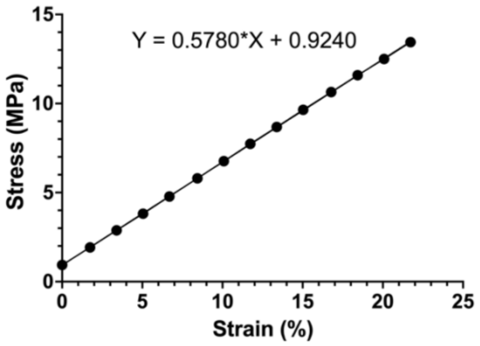

**PDMS-Glucose 1% (w/w)
After Etching**

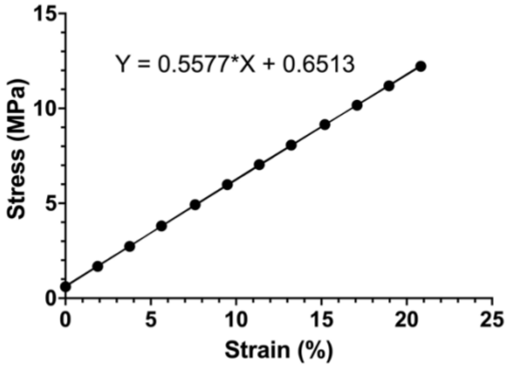

**PDMS-Glucose 5% (w/w)
After etching**

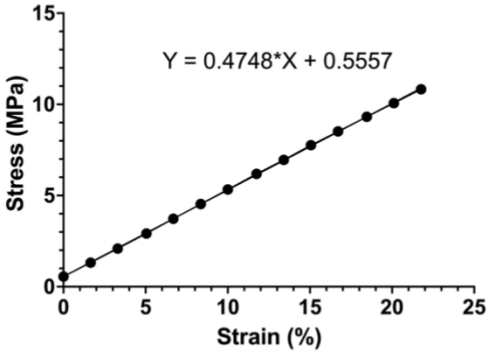

**PDMS-Glucose 10% (w/w)
After Etching**

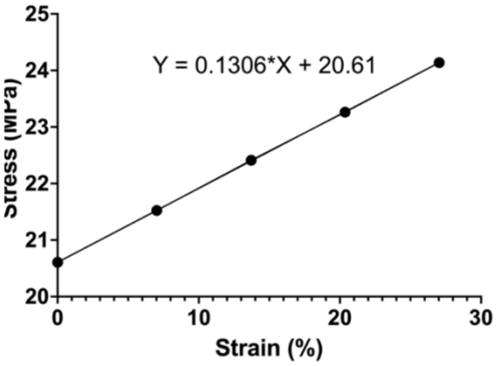

**PDMS-Heteregeneous Silica 0.5 % (w/w)
After Etching**

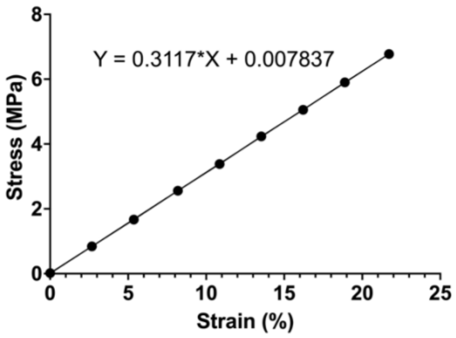

**PDMS-Heteregeneous Silica 1% (w/w)
After Etching**

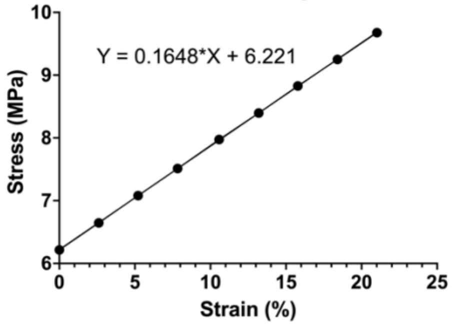

**PDMS-Heteregeneous Silica 5% (w/w)
After Etching**

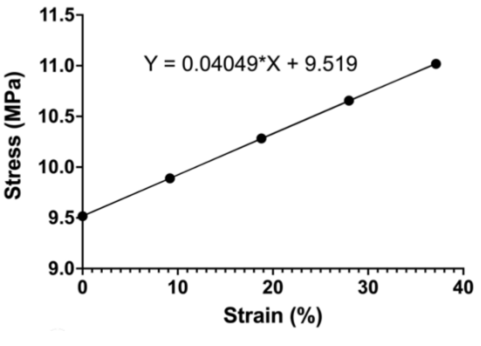

**PDMS-Homogeneous Silica 0.5% (w/w)
After Etching**

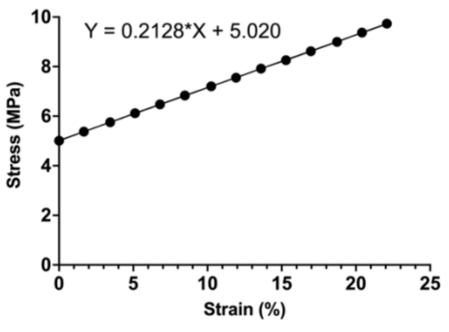

**PDMS-Homogeneous Silica 1% (w/w)
After Etching**

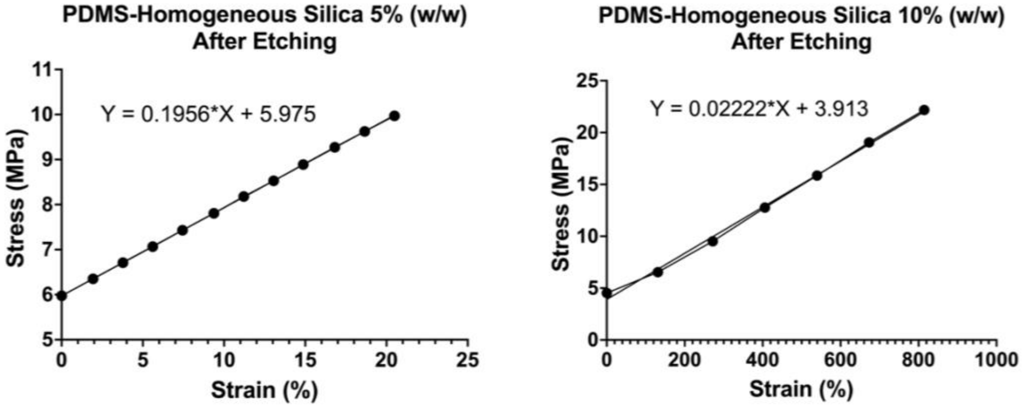

Figure A3.2: Stress versus Strain plots and trendlines (examples) for after etching MNs.

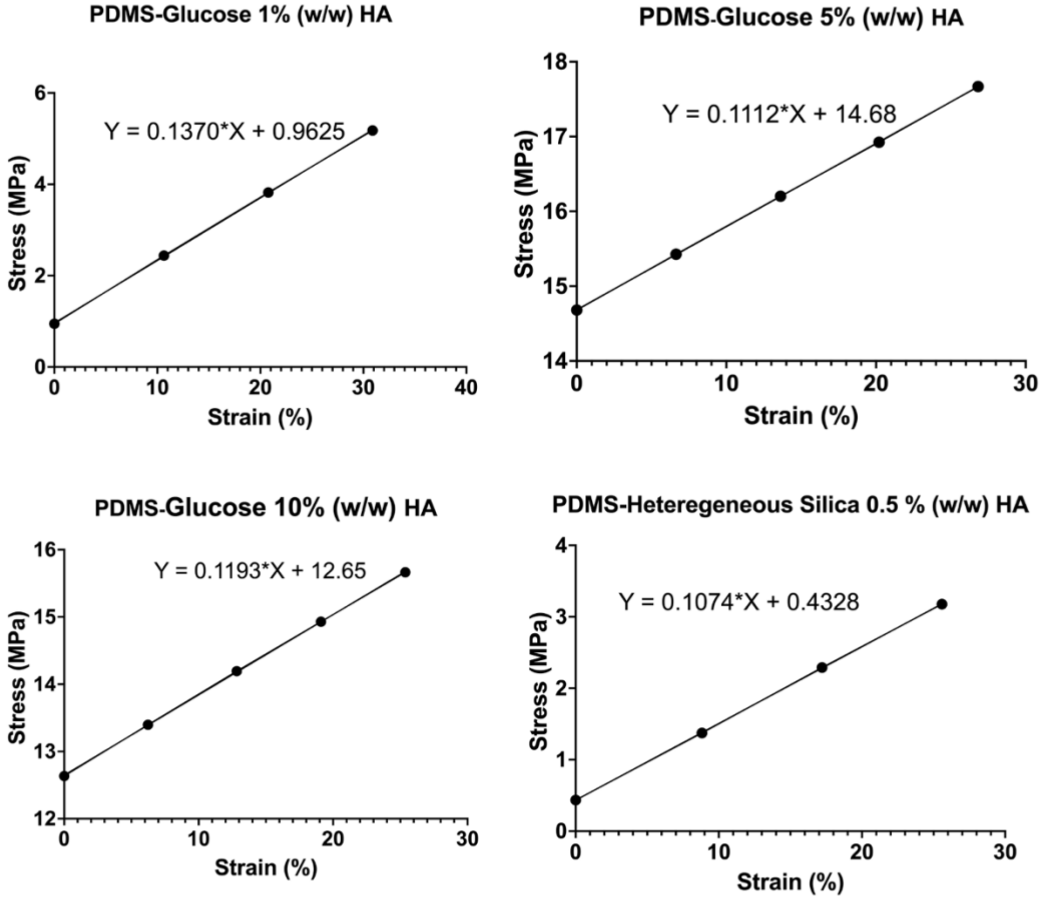

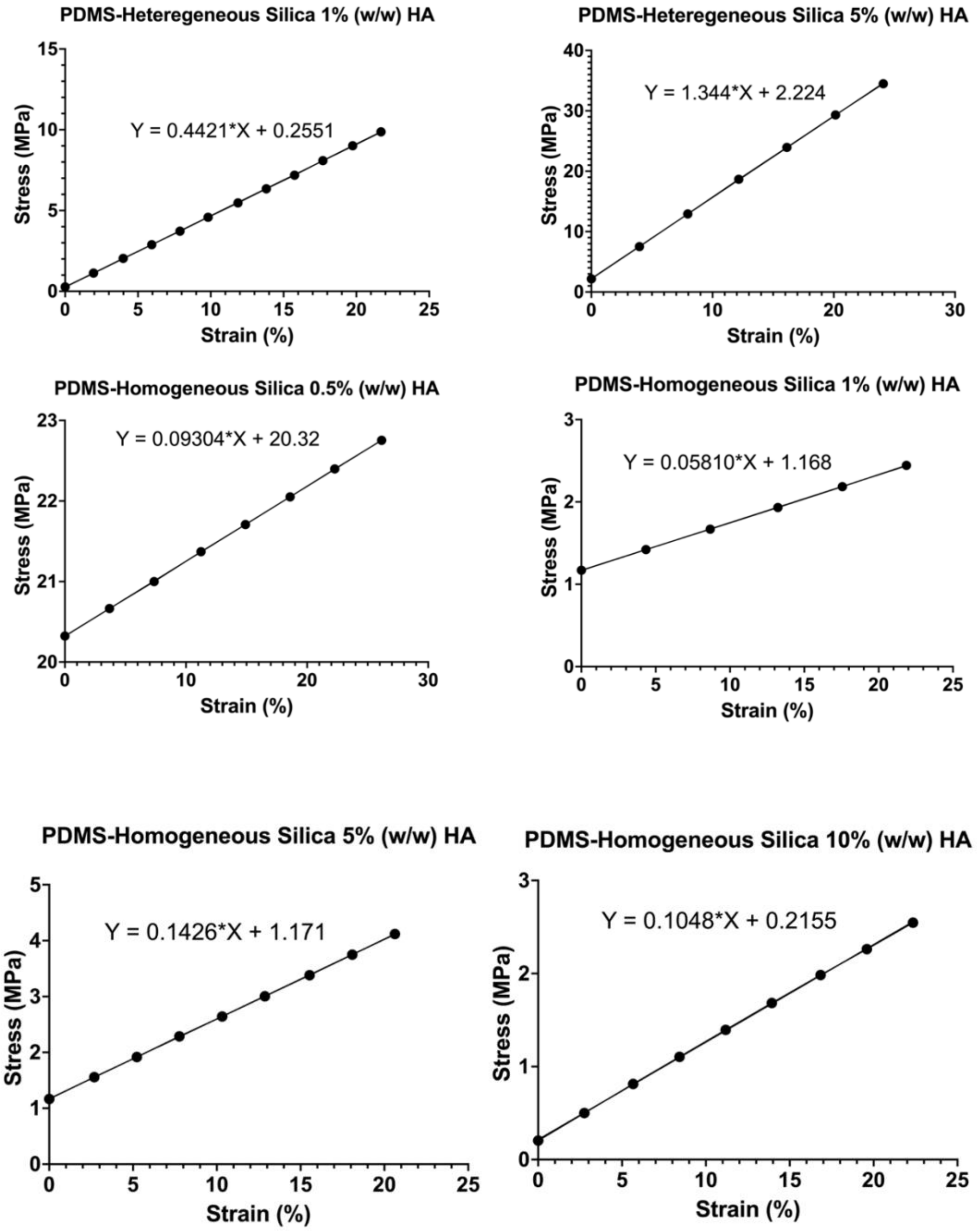

Figure A3.3: Stress versus Strain plots and trendlines (examples) for MNs with HA.

Annex 4: Porosity

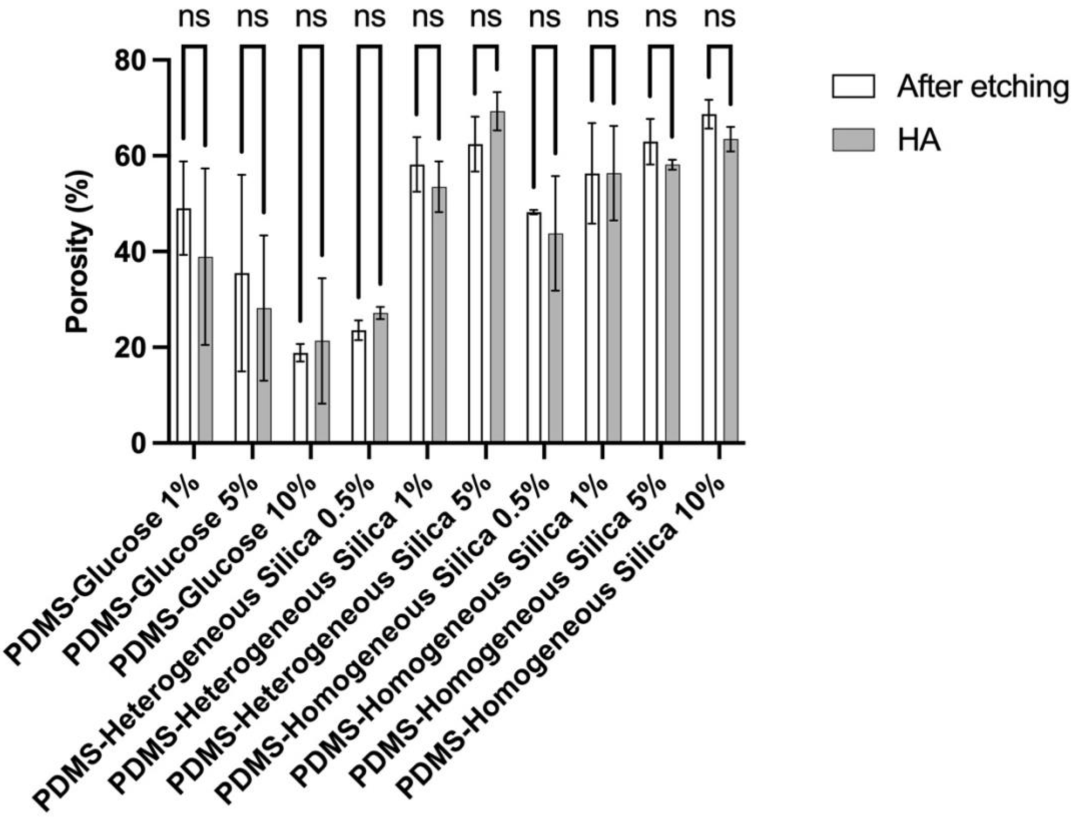

Figure A4.1: Porosity of MNs after etching and MNs with HA solution (N=3).

6. REFERENCES

[1] J. Ribas, J. Pawlikowska, and J. Rouwkema, ‘Microphysiological systems: analysis of the current status, challenges and commercial future’, *Microphysiological Syst.*, vol. 1, pp. 1–1, 2018, doi: 10.21037/mps.2018.10.01.

[2] S. Halldorsson, E. Lucumi, R. Gómez-Sjöberg, and R. M. T. Fleming, ‘Advantages and challenges of microfluidic cell culture in polydimethylsiloxane devices’, *Biosens. Bioelectron.*, vol. 63, pp. 218–231, Jan. 2015, doi: 10.1016/j.bios.2014.07.029.

[3] S. Syama and P. V. Mohanan, ‘Microfluidic based human-on-a-chip: A revolutionary technology in scientific research’, *Trends Food Sci. Technol.*, vol. 110, pp. 711–728, Apr. 2021, doi: 10.1016/j.tifs.2021.02.049.

[4] Y. Zheng *et al.*, ‘Design and fabrication of an integrated 3D dynamic multicellular liver-on-a-chip and its application in hepatotoxicity screening’, *Talanta*, vol. 241, p. 123262, May 2022, doi: 10.1016/j.talanta.2022.123262.

[5] F. Zhang *et al.*, ‘Design and fabrication of an integrated heart-on-a-chip platform for construction of cardiac tissue from human iPSC-derived cardiomyocytes and in situ evaluation of physiological function’, *Biosens. Bioelectron.*, vol. 179, p. 113080, May 2021, doi: 10.1016/j.bios.2021.113080.

[6] A. P. Haring, H. Sontheimer, and B. N. Johnson, ‘Microphysiological Human Brain and Neural Systems-on-a-Chip: Potential Alternatives to Small Animal Models and Emerging Platforms for Drug Discovery and Personalized Medicine’, *Stem Cell Rev. Rep.*, vol. 13, no. 3, pp. 381–406, Jun. 2017, doi: 10.1007/s12015-017-9738-0.

[7] T. T. Nieskens, O. Magnusson, M. Persson, P. Andersson, M. Söderberg, and A. Sjögren, ‘Development of a kidney-on-a-chip model that replicates an antisense oligonucleotide-induced kidney injury biomarker

response', *Toxicol. Lett.*, vol. 350, p. S58, Sep. 2021, doi: 10.1016/S0378-4274(21)00384-2.

[8] R. O. Rodrigues, P. C. Sousa, J. Gaspar, M. Bañobre-López, R. Lima, and G. Minas, 'Organ-on-a-Chip: A Preclinical Microfluidic Platform for the Progress of Nanomedicine', *Small*, vol. 16, no. 51, p. 2003517, Dec. 2020, doi: 10.1002/smll.202003517.

[9] S. Jalili-Firoozinezhad, C. C. Miranda, and J. M. S. Cabral, 'Modeling the Human Body on Microfluidic Chips', *Trends Biotechnol.*, vol. 39, no. 8, pp. 838–852, Aug. 2021, doi: 10.1016/j.tibtech.2021.01.004.

[10] K. Ronaldson-Bouchard and G. Vunjak-Novakovic, 'Organs-on-a-Chip: A Fast Track for Engineered Human Tissues in Drug Development', *Cell Stem Cell*, vol. 22, no. 3, pp. 310–324, Mar. 2018, doi: 10.1016/j.stem.2018.02.011.

[11] X. Joseph, V. Akhil, A. Arathi, and Pv. Mohanan, 'Comprehensive Development in Organ-On-A-Chip Technology', *J. Pharm. Sci.*, vol. 111, no. 1, pp. 18–31, Jan. 2022, doi: 10.1016/j.xphs.2021.07.014.

[12] D. C. Duffy, J. C. McDonald, O. J. A. Schueller, and G. M. Whitesides, 'Rapid Prototyping of Microfluidic Systems in Poly(dimethylsiloxane)', *Anal. Chem.*, vol. 70, no. 23, pp. 4974–4984, Dec. 1998, doi: 10.1021/ac980656z.

[13] M. P. Wolf, G. B. Salieb-Beugelaar, and P. Hunziker, 'PDMS with designer functionalities—Properties, modifications strategies, and applications', *Prog. Polym. Sci.*, vol. 83, pp. 97–134, Aug. 2018, doi: 10.1016/j.progpolymsci.2018.06.001.

[14] K. J. Regehr *et al.*, 'Biological implications of polydimethylsiloxane-based microfluidic cell culture', *Lab. Chip*, vol. 9, no. 15, p. 2132, 2009, doi: 10.1039/b903043c.

[15] P.-J. Wipff, H. Majd, C. Acharya, L. Buscemi, J.-J. Meister, and B. Hinz, 'The covalent attachment of adhesion molecules to silicone membranes for

cell stretching applications', *Biomaterials*, vol. 30, no. 9, pp. 1781–1789, Mar. 2009, doi: 10.1016/j.biomaterials.2008.12.022.

[16] G. Sriram *et al.*, 'Full-thickness human skin-on-chip with enhanced epidermal morphogenesis and barrier function', *Mater. Today*, vol. 21, no. 4, pp. 326–340, May 2018, doi: 10.1016/j.mattod.2017.11.002.

[17] N. X. T. Le, K. T. L. Trinh, and N. Y. Lee, 'Poly(acrylic acid) as an adhesion promoter for UV-assisted thermoplastic bonding: Application for the in vitro construction of human blood vessels', *Mater. Sci. Eng. C*, vol. 122, p. 111874, Mar. 2021, doi: 10.1016/j.msec.2021.111874.

[18] G. Pitingolo, P. Nizard, A. Riaud, and V. Taly, 'Beyond the on/off chip trade-off: A reversibly sealed microfluidic platform for 3D tumor microtissue analysis', *Sens. Actuators B Chem.*, vol. 274, pp. 393–401, Nov. 2018, doi: 10.1016/j.snb.2018.07.166.

[19] K.-J. Jang *et al.*, 'Human kidney proximal tubule-on-a-chip for drug transport and nephrotoxicity assessment', *Integr. Biol.*, vol. 5, no. 9, pp. 1119–1129, May 2013, doi: 10.1039/c3ib40049b.

[20] B. A. Hassell *et al.*, 'Human Organ Chip Models Recapitulate Orthotopic Lung Cancer Growth, Therapeutic Responses, and Tumor Dormancy In Vitro', *Cell Rep.*, vol. 21, no. 2, pp. 508–516, Oct. 2017, doi: 10.1016/j.celrep.2017.09.043.

[21] K. Kulthong *et al.*, 'Microfluidic chip for culturing intestinal epithelial cell layers: Characterization and comparison of drug transport between dynamic and static models', *Toxicol. In Vitro*, vol. 65, p. 104815, Jun. 2020, doi: 10.1016/j.tiv.2020.104815.

[22] H. Lee and D.-W. Cho, 'One-step fabrication of an organ-on-a-chip with spatial heterogeneity using a 3D bioprinting technology', *Lab. Chip*, vol. 16, no. 14, pp. 2618–2625, 2016, doi: 10.1039/C6LC00450D.

[23] M. Verhulsel, M. Vignes, S. Descroix, L. Malaquin, D. M. Vignjevic, and J.-L. Viovy, ‘A review of microfabrication and hydrogel engineering for micro-organs on chips’, *Biomaterials*, vol. 35, no. 6, pp. 1816–1832, Feb. 2014, doi: 10.1016/j.biomaterials.2013.11.021.

[24] Q. Hamid, C. Wang, J. Snyder, S. Williams, Y. Liu, and W. Sun, ‘Maskless fabrication of cell-laden microfluidic chips with localized surface functionalization for the co-culture of cancer cells’, *Biofabrication*, vol. 7, no. 1, p. 015012, 2015, doi: 10.1088/1758-5090/7/1/015012.

[25] D. Mandt *et al.*, ‘Fabrication of placental barrier structures within a microfluidic device utilizing two-photon polymerization’, *Int. J. Bioprinting*, vol. 4, no. 2, Jul. 2018, doi: 10.18063/ijb.v4i2.144.

[26] Y. Wu *et al.*, ‘The neurotoxicity of Nε-(carboxymethyl)lysine in food processing by a study based on animal and organotypic cell culture’, *Ecotoxicol. Environ. Saf.*, vol. 190, p. 110077, Mar. 2020, doi: 10.1016/j.ecoenv.2019.110077.

[27] J. Zhang, F. Chen, Z. He, Y. Ma, K. Uchiyama, and J.-M. Lin, ‘A novel approach for precisely controlled multiple cell patterning in microfluidic chips by inkjet printing and the detection of drug metabolism and diffusion’, *Analyst*, vol. 141, no. 10, pp. 2940–2947, 2016, doi: 10.1039/C6AN00395H.

[28] G. Tejada Jacob, V. E. Passamai, S. Katz, G. R. Castro, and V. Alvarez, ‘Hydrogels for extrusion-based bioprinting: General considerations’, *Bioprinting*, vol. 27, p. e00212, Aug. 2022, doi: 10.1016/j.bprint.2022.e00212.

[29] H.-W. Kang, S. J. Lee, I. K. Ko, C. Kengla, J. J. Yoo, and A. Atala, ‘A 3D bioprinting system to produce human-scale tissue constructs with structural integrity’, *Nat. Biotechnol.*, vol. 34, no. 3, pp. 312–319, Mar. 2016, doi: 10.1038/nbt.3413.

[30] F. Yu and D. Choudhury, ‘Microfluidic bioprinting for organ-on-a-chip models’, *Drug Discov. Today*, vol. 24, no. 6, pp. 1248–1257, Jun. 2019, doi: 10.1016/j.drudis.2019.03.025.

[31] Y. S. Zhang *et al.*, ‘Bioprinting 3D microfibrous scaffolds for engineering endothelialized myocardium and heart-on-a-chip’, *Biomaterials*, vol. 110, pp. 45–59, 2016, doi: https://doi.org/10.1016/j.biomaterials.2016.09.003.

[32] C. Tian, Q. Tu, W. Liu, and J. Wang, ‘Recent advances in microfluidic technologies for organ-on-a-chip’, *TrAC Trends Anal. Chem.*, vol. 117, pp. 146–156, Aug. 2019, doi: 10.1016/j.trac.2019.06.005.

[33] D. Huh, B. D. Matthews, A. Mammoto, M. Montoya-Zavala, H. Y. Hsin, and D. E. Ingber, ‘Reconstituting Organ-Level Lung Functions on a Chip’, *Science*, vol. 328, no. 5986, pp. 1662–1668, Jun. 2010, doi: 10.1126/science.1188302.

[34] S. I. Ahn *et al.*, ‘Microengineered human blood–brain barrier platform for understanding nanoparticle transport mechanisms’, *Nat. Commun.*, vol. 11, no. 1, p. 175, Dec. 2020, doi: 10.1038/s41467-019-13896-7.

[35] J. Wang, C. Wang, N. Xu, Z.-F. Liu, D.-W. Pang, and Z.-L. Zhang, ‘A virus-induced kidney disease model based on organ-on-a-chip: Pathogenesis exploration of virus-related renal dysfunctions’, *Biomaterials*, vol. 219, p. 119367, Oct. 2019, doi: 10.1016/j.biomaterials.2019.119367.

[36] H. J. Kim, H. Li, J. J. Collins, and D. E. Ingber, ‘Contributions of microbiome and mechanical deformation to intestinal bacterial overgrowth and inflammation in a human gut-on-a-chip’, *Proc. Natl. Acad. Sci.*, vol. 113, no. 1, Jan. 2016, doi: 10.1073/pnas.1522193112.

[37] S. Bersini *et al.*, ‘A microfluidic 3D in vitro model for specificity of breast cancer metastasis to bone’, *Biomaterials*, vol. 35, no. 8, pp. 2454–2461, Mar. 2014, doi: 10.1016/j.biomaterials.2013.11.050.

[38] V. S. Shirure, S. F. Lam, B. Shergill, Y. E. Chu, N. R. Ng, and S. C. George, ‘Quantitative design strategies for fine control of oxygen in microfluidic systems’, *Lab. Chip*, vol. 20, no. 16, pp. 3036–3050, 2020, doi: 10.1039/D0LC00350F.

[39] L. Ren *et al.*, ‘Investigation of Hypoxia-Induced Myocardial Injury Dynamics in a Tissue Interface Mimicking Microfluidic Device’, *Anal. Chem.*, vol. 85, no. 1, pp. 235–244, Jan. 2013, doi: 10.1021/ac3025812.

[40] A. Skardal *et al.*, ‘Multi-tissue interactions in an integrated three-tissue organ-on-a-chip platform’, *Sci. Rep.*, vol. 7, no. 1, p. 8837, Dec. 2017, doi: 10.1038/s41598-017-08879-x.

[41] L. J. Y. Ong *et al.*, ‘Self-aligning Tetris-Like (TILE) modular microfluidic platform for mimicking multi-organ interactions’, *Lab. Chip*, vol. 19, no. 13, pp. 2178–2191, 2019, doi: 10.1039/C9LC00160C.

[42] P. Loskill, S. G. Marcus, A. Mathur, W. M. Reese, and K. E. Healy, ‘μOrgano: A Lego®-Like Plug & Play System for Modular Multi-Organ-Chips’, *PLOS ONE*, vol. 10, no. 10, p. e0139587, Oct. 2015, doi: 10.1371/journal.pone.0139587.

[43] I. Maschmeyer *et al.*, ‘A four-organ-chip for interconnected long-term co-culture of human intestine, liver, skin and kidney equivalents’, *Lab. Chip*, vol. 15, no. 12, pp. 2688–2699, 2015, doi: 10.1039/C5LC00392J.

[44] T. Satoh *et al.*, ‘A multi-throughput multi-organ-on-a-chip system on a plate formatted pneumatic pressure-driven medium circulation platform’, *Lab. Chip*, vol. 18, no. 1, pp. 115–125, 2018, doi: 10.1039/C7LC00952F.

[45] G. Forte and P. Ertl, ‘Small Force, Big Impact: Next Generation Organ-on-a-Chip Systems Incorporating Biomechanical Cues’, *Front. Physiol.*, vol. 9, p. 8, 2018.

[46] Kaarj and Yoon, ‘Methods of Delivering Mechanical Stimuli to Organ-on-a-Chip’, *Micromachines*, vol. 10, no. 10, p. 700, Oct. 2019, doi: 10.3390/mi10100700.

[47] H. Chen *et al.*, ‘Microfluidic models of physiological or pathological flow shear stress for cell biology, disease modeling and drug development’, *TrAC Trends Anal. Chem.*, vol. 117, pp. 186–199, Aug. 2019, doi: 10.1016/j.trac.2019.06.023.

[48] Y. S. Zhang *et al.*, ‘Multisensor-integrated organs-on-chips platform for automated and continual in situ monitoring of organoid behaviors’, *Proc. Natl. Acad. Sci.*, vol. 114, no. 12, Mar. 2017, doi: 10.1073/pnas.1612906114.

[49] S. H. Lee and B.-H. Jun, ‘Advances in dynamic microphysiological organ-on-a-chip: Design principle and its biomedical application’, *J. Ind. Eng. Chem.*, vol. 71, pp. 65–77, Mar. 2019, doi: 10.1016/j.jiec.2018.11.041.

[50] L. C. Delon, A. Nilghaz, E. Cheah, C. Prestidge, and B. Thierry, ‘Unlocking the Potential of Organ-on-Chip Models through Pumpless and Tubeless Microfluidics’, p. 9, 2020.

[51] C. L. Thompson, S. Fu, H. K. Heywood, M. M. Knight, and S. D. Thorpe, ‘Mechanical Stimulation: A Crucial Element of Organ-on-Chip Models’, *Front. Bioeng. Biotechnol.*, vol. 8, p. 602646, Dec. 2020, doi: 10.3389/fbioe.2020.602646.

[52] S. A. M. Shaegh, F. D. Ferrari, and Y. S. Zhang, ‘A microfluidic optical platform for real-time monitoring of pH and oxygen in microfluidic bioreactors and organ-on-chip devices’, p. 15, 2016.

[53] O. Y. F. Henry, R. Villenave, M. J. Cronce, W. D. Leineweber, M. A. Benz, and D. E. Ingber, ‘Organs-on-chips with integrated electrodes for trans-epithelial electrical resistance (TEER) measurements of human epithelial barrier function’, *Lab. Chip*, vol. 17, no. 13, pp. 2264–2271, 2017, doi: 10.1039/C7LC00155J.

[54] F. Cantoni, G. Werr, L. Barbe, A. M. Porras, and M. Tenje, ‘A microfluidic chip carrier including temperature control and perfusion system for long-term cell imaging’, *HardwareX*, vol. 10, p. e00245, Oct. 2021, doi: 10.1016/j.ohx.2021.e00245.

[55] H. Zirath *et al.*, ‘Every Breath You Take: Non-invasive Real-Time Oxygen Biosensing in Two- and Three-Dimensional Microfluidic Cell Models’, *Front. Physiol.*, vol. 9, p. 815, Jul. 2018, doi: 10.3389/fphys.2018.00815.

[56] N. Zhang *et al.*, ‘Multifunctional 3D electrode platform for real-time in situ monitoring and stimulation of cardiac tissues’, *Biosens. Bioelectron.*, vol. 112, pp. 149–155, Jul. 2018, doi: 10.1016/j.bios.2018.04.037.

[57] H. Liu *et al.*, ‘Microdevice arrays with strain sensors for 3D mechanical stimulation and monitoring of engineered tissues’, *Biomaterials*, vol. 172, pp. 30–40, Jul. 2018, doi: 10.1016/j.biomaterials.2018.04.041.

[58] M. A. U. Khalid, Y. S. Kim, M. Ali, B. G. Lee, Y.-J. Cho, and K. H. Choi, ‘A lung cancer-on-chip platform with integrated biosensors for physiological monitoring and toxicity assessment’, *Biochem. Eng. J.*, vol. 155, p. 107469, Mar. 2020, doi: 10.1016/j.bej.2019.107469.

[59] Z. Liao *et al.*, ‘Recent advances in microfluidic chip integrated electronic biosensors for multiplexed detection’, *Biosens. Bioelectron.*, vol. 121, pp. 272–280, Dec. 2018, doi: 10.1016/j.bios.2018.08.061.

[60] Y. Zhu *et al.*, ‘State of the art in integrated biosensors for organ-on-a-chip applications’, *Curr. Opin. Biomed. Eng.*, vol. 19, p. 100309, Sep. 2021, doi: 10.1016/j.cobme.2021.100309.

[61] A. Tajeddin and N. Mustafaoglu, ‘Design and Fabrication of Organ-on-Chips: Promises and Challenges’, *Micromachines*, vol. 12, no. 12, p. 1443, Nov. 2021, doi: 10.3390/mi12121443.

[62] D. Bavli *et al.*, ‘Real-time monitoring of metabolic function in liver-on-chip microdevices tracks the dynamics of mitochondrial dysfunction’, *Proc. Natl. Acad. Sci.*, vol. 113, no. 16, Apr. 2016, doi: 10.1073/pnas.1522556113.

[63] J. Lee *et al.*, ‘A Heart-Breast Cancer-on-a-Chip Platform for Disease Modeling and Monitoring of Cardiotoxicity Induced by Cancer Chemotherapy’, *Small*, vol. 17, no. 15, p. 2004258, Apr. 2021, doi: 10.1002/smll.202004258.

[64] M. A. Ortega *et al.*, ‘Muscle-on-a-chip with an on-site multiplexed biosensing system for *in situ* monitoring of secreted IL-6 and TNF-α’, *Lab. Chip*, vol. 19, no. 15, pp. 2568–2580, 2019, doi: 10.1039/C9LC00285E.

[65] P. M. Misun, J. Rothe, Y. R. F. Schmid, A. Hierlemann, and O. Frey, ‘Multi-analyte biosensor interface for real-time monitoring of 3D microtissue spheroids in hanging-drop networks’, *Microsyst. Nanoeng.*, vol. 2, no. 1, p. 16022, Dec. 2016, doi: 10.1038/micronano.2016.22.

[66] Z. Liao *et al.*, ‘Microfluidic chip coupled with optical biosensors for simultaneous detection of multiple analytes: A review’, *Biosens. Bioelectron.*, vol. 126, pp. 697–706, Feb. 2019, doi: 10.1016/j.bios.2018.11.032.

[67] J. R. Mejía-Salazar and O. N. Oliveira, ‘Plasmonic Biosensing: Focus Review’, *Chem. Rev.*, vol. 118, no. 20, pp. 10617–10625, Oct. 2018, doi: 10.1021/acs.chemrev.8b00359.

[68] J. F. C. Loo, A. H. P. Ho, A. P. F. Turner, and W. C. Mak, ‘Integrated Printed Microfluidic Biosensors’, *Trends Biotechnol.*, vol. 37, no. 10, pp. 1104–1120, Oct. 2019, doi: 10.1016/j.tibtech.2019.03.009.

[69] X. Meng, Z. Zhang, and L. Li, ‘Micro/nano needles for advanced drug delivery’, *Prog. Nat. Sci. Mater. Int.*, vol. 30, no. 5, pp. 589–596, Oct. 2020, doi: 10.1016/j.pnsc.2020.09.016.

[70] U. Angkawinitwong *et al.*, ‘A Novel Transdermal Protein Delivery Strategy via Electrohydrodynamic Coating of PLGA Microparticles onto Microneedles’, *ACS Appl. Mater. Interfaces*, vol. 12, no. 11, pp. 12478–12488, Mar. 2020, doi: 10.1021/acsami.9b22425.

[71] C. Chiappini *et al.*, ‘Biodegradable silicon nanoneedles delivering nucleic acids intracellularly induce localized in vivo neovascularization’, *Nat. Mater.*, vol. 14, no. 5, pp. 532–539, May 2015, doi: 10.1038/nmat4249.

[72] J. Zhuang *et al.*, ‘Study on the fabrication and characterization of tip-loaded dissolving microneedles for transdermal drug delivery’, *Eur. J. Pharm. Biopharm.*, vol. 157, pp. 66–73, Dec. 2020, doi: 10.1016/j.ejpb.2020.10.002.

[73] T. Waghule *et al.*, ‘Microneedles: A smart approach and increasing potential for transdermal drug delivery system’, *Biomed. Pharmacother.*, vol. 109, pp. 1249–1258, Jan. 2019, doi: 10.1016/j.biopha.2018.10.078.

[74] K.-T. Chang, Y.-K. Shen, F.-Y. Fan, Y. Lin, and S.-C. Kang, ‘Optimal design and fabrication of a microneedle arrays patch’, *J. Manuf. Process.*, vol. 54, pp. 274–285, Jun. 2020, doi: 10.1016/j.jmapro.2020.02.024.

[75] V. Sonetha, S. Majumdar, and S. Shah, ‘Step-wise micro-fabrication techniques of microneedle arrays with applications in transdermal drug delivery – A review’, *J. Drug Deliv. Sci. Technol.*, vol. 68, p. 103119, Feb. 2022, doi: 10.1016/j.jddst.2022.103119.

[76] C. Chiappini, ‘Nanoneedle-Based Sensing in Biological Systems’, *ACS Sens.*, vol. 2, no. 8, pp. 1086–1102, Aug. 2017, doi: 10.1021/acssensors.7b00350.

[77] H. Chang *et al.*, ‘A Swellable Microneedle Patch to Rapidly Extract Skin Interstitial Fluid for Timely Metabolic Analysis’, *Adv. Mater.*, vol. 29, no. 37, p. 1702243, Oct. 2017, doi: 10.1002/adma.201702243.

[78] F. Meng *et al.*, ‘Polymeric-based microneedle arrays as potential platforms in the development of drugs delivery systems’, *J. Adv. Res.*, vol. 26, pp. 137–147, Nov. 2020, doi: 10.1016/j.jare.2020.07.017.

[79] R. Nagarkar, M. Singh, H. X. Nguyen, and S. Jonnalagadda, ‘A review of recent advances in microneedle technology for transdermal drug delivery’, *J. Drug Deliv. Sci. Technol.*, vol. 59, p. 101923, Oct. 2020, doi: 10.1016/j.jddst.2020.101923.

[80] S. Pradeep Narayanan and S. Raghavan, ‘Solid silicon microneedles for drug delivery applications’, *Int. J. Adv. Manuf. Technol.*, vol. 93, no. 1–4, pp. 407–422, Oct. 2017, doi: 10.1007/s00170-016-9698-6.

[81] K. Ita, ‘Modulation of transdermal drug delivery with coated microneedles’, *J. Drug Deliv. Sci. Technol.*, vol. 45, pp. 203–212, Jun. 2018, doi: 10.1016/j.jddst.2018.03.021.

[82] A. Ullah, C. M. Kim, and G. M. Kim, ‘Porous polymer coatings on metal microneedles for enhanced drug delivery’, *R. Soc. Open Sci.*, vol. 5, no. 4, p. 171609, Apr. 2018, doi: 10.1098/rsos.171609.

[83] Á. Cárcamo-Martínez, B. Mallon, J. Domínguez-Robles, L. K. Vora, Q. K. Anjani, and R. F. Donnelly, ‘Hollow microneedles: A perspective in biomedical applications’, *Int. J. Pharm.*, vol. 599, p. 120455, Apr. 2021, doi: 10.1016/j.ijpharm.2021.120455.

[84] L. Zhang, R. Guo, S. Wang, X. Yang, G. Ling, and P. Zhang, ‘Fabrication, evaluation and applications of dissolving microneedles’, *Int. J. Pharm.*, vol. 604, p. 120749, Jul. 2021, doi: 10.1016/j.ijpharm.2021.120749.

[85] K. Peng *et al.*, ‘Hydrogel-forming microneedles for rapid and efficient skin deposition of controlled release tip-implants’, *Mater. Sci. Eng. C*, vol. 127, p. 112226, Aug. 2021, doi: 10.1016/j.msec.2021.112226.

[86] K. van der Maaden, R. Luttge, P. J. Vos, J. Bouwstra, G. Kersten, and I. Ploemen, ‘Microneedle-based drug and vaccine delivery via nanoporous

microneedle arrays', *Drug Deliv. Transl. Res.*, vol. 5, no. 4, pp. 397–406, Aug. 2015, doi: 10.1007/s13346-015-0238-y.

[87] T. N. Tarbox, A. B. Watts, Z. Cui, and R. O. Williams, 'An update on coating/manufacturing techniques of microneedles', *Drug Deliv. Transl. Res.*, vol. 8, no. 6, pp. 1828–1843, Dec. 2018, doi: 10.1007/s13346-017-0466-4.

[88] Z. Faraji Rad, P. D. Prewett, and G. J. Davies, 'Rapid prototyping and customizable microneedle design: Ultra-sharp microneedle fabrication using two-photon polymerization and low-cost micromolding techniques', *Manuf. Lett.*, vol. 30, pp. 39–43, Oct. 2021, doi: 10.1016/j.mfglet.2021.10.007.

[89] H. Takahashi *et al.*, 'Scalable fabrication of microneedle arrays via spatially controlled UV exposure', *Microsyst. Nanoeng.*, vol. 2, no. 1, p. 16049, Dec. 2016, doi: 10.1038/micronano.2016.49.

[90] 'Nickel Microneedles Fabricated by Sequential Copper and Nickel Electroless Plating and Copper Chemical Wet Etching', *Sens. Mater.*, p. 45, 2008, doi: 10.18494/SAM.2008.507.

[91] Q. L. Wang, D. D. Zhu, X. B. Liu, B. Z. Chen, and X. D. Guo, 'Microneedles with Controlled Bubble Sizes and Drug Distributions for Efficient Transdermal Drug Delivery', *Sci. Rep.*, vol. 6, no. 1, p. 38755, Dec. 2016, doi: 10.1038/srep38755.

[92] S. Aoyagi, H. Izumi, Y. Isono, M. Fukuda, and H. Ogawa, 'Laser fabrication of high aspect ratio thin holes on biodegradable polymer and its application to a microneedle', *Sens. Actuators Phys.*, vol. 139, no. 1–2, pp. 293–302, Sep. 2007, doi: 10.1016/j.sna.2006.11.022.

[93] J. D. Kim, M. Kim, H. Yang, K. Lee, and H. Jung, 'Droplet-born air blowing: Novel dissolving microneedle fabrication', *J. Controlled Release*, vol. 170, no. 3, pp. 430–436, Sep. 2013, doi: 10.1016/j.jconrel.2013.05.026.

[94] C. P. P. Pere *et al.*, ‘3D printed microneedles for insulin skin delivery’, *Int. J. Pharm.*, vol. 544, no. 2, pp. 425–432, Jun. 2018, doi: 10.1016/j.ijpharm.2018.03.031.

[95] P. Dardano, I. Rea, and L. De Stefano, ‘Microneedles-based electrochemical sensors: New tools for advanced biosensing’, *Curr. Opin. Electrochem.*, vol. 17, pp. 121–127, Oct. 2019, doi: 10.1016/j.coelec.2019.05.012.

[96] S. Kusama *et al.*, ‘Transdermal electroosmotic flow generated by a porous microneedle array patch’, *Nat. Commun.*, vol. 12, no. 1, p. 658, Dec. 2021, doi: 10.1038/s41467-021-20948-4.

[97] L. Liu, H. Kai, K. Nagamine, Y. Ogawa, and M. Nishizawa, ‘Porous polymer microneedles with interconnecting microchannels for rapid fluid transport’, *RSC Adv.*, vol. 6, no. 54, pp. 48630–48635, 2016, doi: 10.1039/C6RA07882F.

[98] L. Bao, J. Park, G. Bonfante, and B. Kim, ‘Recent advances in porous microneedles: materials, fabrication, and transdermal applications’, *Drug Deliv. Transl. Res.*, vol. 12, no. 2, pp. 395–414, Feb. 2022, doi: 10.1007/s13346-021-01045-x.

[99] K. Takeuchi, N. Takama, R. Kinoshita, T. Okitsu, and B. Kim, ‘Flexible and porous microneedles of PDMS for continuous glucose monitoring’, *Biomed. Microdevices*, vol. 22, no. 4, p. 79, Dec. 2020, doi: 10.1007/s10544-020-00532-1.

[100] J. Li *et al.*, ‘Fabrication of gradient porous microneedle array by modified hot embossing for transdermal drug delivery’, *Mater. Sci. Eng. C*, vol. 96, pp. 576–582, Mar. 2019, doi: 10.1016/j.msec.2018.11.074.

[101] L. Humrez, M. Ramos, A. Al-Jumaily, M. Petchu, and J. Ingram, ‘Synthesis and characterisation of porous polymer microneedles’, *J. Polym.*

Res., vol. 18, no. 5, pp. 1043–1052, Sep. 2011, doi: 10.1007/s10965-010-9505-2.

[102] A. Mata, A. J. Fleischman, and S. Roy, ‘Characterization of Polydimethylsiloxane (PDMS) Properties for Biomedical Micro/Nanosystems’, *Biomed. Microdevices*, vol. 7, no. 4, pp. 281–293, Dec. 2005, doi: 10.1007/s10544-005-6070-2.

[103] D. Zhu, S. Handschuh-Wang, and X. Zhou, ‘Recent progress in fabrication and application of polydimethylsiloxane sponges’, *J. Mater. Chem. A*, vol. 5, no. 32, pp. 16467–16497, 2017, doi: 10.1039/C7TA04577H.

[104] Q. Lin, S. He, Q. Liu, J. Yang, X. Qi, and Y. Wang, ‘Construction of a 3D interconnected boron nitride nanosheets in a PDMS matrix for high thermal conductivity and high deformability’, *Compos. Sci. Technol.*, vol. 226, p. 109528, Jul. 2022, doi: 10.1016/j.compscitech.2022.109528.

[105] S. Kalidhasan and H.-Y. Lee, ‘Preparation of floating PDMS sponge catalysts embedded with copper oxide(s): A prelude to the study of its application toward the effective rhodamine B degradation by sonochemical method’, *J. Environ. Chem. Eng.*, vol. 10, no. 2, p. 107254, Apr. 2022, doi: 10.1016/j.jece.2022.107254.

[106] E. Pedraza *et al.*, ‘Macroporous Three-Dimensional PDMS Scaffolds for Extrahepatic Islet Transplantation’, *Cell Transplant.*, vol. 22, no. 7, pp. 1123–1135, Jul. 2013, doi: 10.3727/096368912X657440.

[107] S. Nikpour, Z. Ansari-Asl, T. Sedaghat, and E. Hoveizi, ‘Curcumin-loaded Fe-MOF/PDMS porous scaffold: Fabrication, characterization, and biocompatibility assessment’, *J. Ind. Eng. Chem.*, vol. 110, pp. 188–197, Jun. 2022, doi: 10.1016/j.jiec.2022.02.052.

[108] M. Chen, L. Zhang, S. Duan, S. Jing, H. Jiang, and C. Li, ‘Highly Stretchable Conductors Integrated with a Conductive Carbon Nanotube/Graphene Network and 3D Porous Poly(dimethylsiloxane)’, *Adv.*

Funct. Mater., vol. 24, no. 47, pp. 7548–7556, 2014, doi: https://doi.org/10.1002/adfm.201401886.

[109] L. Bao, J. Park, G. Bonfante, and B. Kim, 'Recent advances in porous microneedles: materials, fabrication, and transdermal applications', *Drug Deliv. Transl. Res.*, vol. 12, no. 2, pp. 395–414, Feb. 2022, doi: 10.1007/s13346-021-01045-x.

[110] Y. Jung *et al.*, 'Wearable piezoresistive strain sensor based on graphene-coated three-dimensional micro-porous PDMS sponge', *Micro Nano Syst. Lett.*, vol. 7, no. 1, p. 20, Dec. 2019, doi: 10.1186/s40486-019-0097-2.

[111] X.-Y. Yang, L.-H. Chen, Y. Li, J. C. Rooke, C. Sanchez, and B.-L. Su, 'Hierarchically porous materials: synthesis strategies and structure design', *Chem. Soc. Rev.*, vol. 46, no. 2, pp. 481–558, 2017, doi: 10.1039/C6CS00829A.

[112] N. Vilanova, Y. V. Kolen'ko, C. Solans, and C. Rodríguez-Abreu, 'Multiple emulsions as soft templates for the synthesis of multifunctional silicone porous particles', *J. Colloid Interface Sci.*, vol. 437, pp. 235–243, Jan. 2015, doi: 10.1016/j.jcis.2014.09.006.

[113] P. Thurgood, S. Baratchi, C. Szydzik, A. Mitchell, and K. Khoshmanesh, 'Porous PDMS structures for the storage and release of aqueous solutions into fluidic environments', *Lab Chip*, vol. 17, no. 14, pp. 2517–2527, 2017, doi: 10.1039/C7LC00350A.

[114] H. Wang, R. Zhang, D. Yuan, S. Xu, and L. Wang, 'Gas Foaming Guided Fabrication of 3D Porous Plasmonic Nanoplatform with Broadband Absorption, Tunable Shape, Excellent Stability, and High Photothermal Efficiency for Solar Water Purification', *Adv. Funct. Mater.*, vol. 30, no. 46, p. 2003995, Nov. 2020, doi: 10.1002/adfm.202003995.

[115] A. Salerno, M. Oliviero, E. Di Maio, S. Iannace, and P. A. Netti, 'Design of porous polymeric scaffolds by gas foaming of heterogeneous blends', *J. Mater. Sci. Mater. Med.*, vol. 20, no. 10, pp. 2043–2051, Oct. 2009, doi: 10.1007/s10856-009-3767-4.

[116] M. Abshirini, M. C. Saha, M. Cengiz Altan, and Y. Liu, 'Synthesis and characterization of hierarchical porous structure of polydimethylsiloxane (PDMS) sheets via two-step phase separation method', *Mater. Des.*, vol. 212, p. 110194, Dec. 2021, doi: 10.1016/j.matdes.2021.110194.

[117] F. Svec, 'Porous polymer monoliths: Amazingly wide variety of techniques enabling their preparation', *J. Chromatogr. A*, vol. 1217, no. 6, pp. 902–924, Feb. 2010, doi: 10.1016/j.chroma.2009.09.073.

[118] S. Hirobe *et al.*, 'Development and Clinical Study of a Self-Dissolving Microneedle Patch for Transcutaneous Immunization Device', *Pharm. Res.*, vol. 30, no. 10, pp. 2664–2674, Oct. 2013, doi: 10.1007/s11095-013-1092-6.

[119] P. Xue *et al.*, 'Surface Modification of Poly(dimethylsiloxane) with Polydopamine and Hyaluronic Acid To Enhance Hemocompatibility for Potential Applications in Medical Implants or Devices', *ACS Appl. Mater. Interfaces*, vol. 9, no. 39, pp. 33632–33644, Oct. 2017, doi: 10.1021/acsami.7b10260.

[120] J. Peixoto, P. Flores, and A. P. Souto, 'BREATHABLE, IMPERMEABLE AND ODOURLESS LINING FOR ORTHOPAEDIC FOOTWEAR APPLICATION', p. 7, 2012.

[121] C. Y. Beh *et al.*, 'Morphological and optical properties of porous hydroxyapatite/cornstarch (HAp/Cs) composites', *J. Mater. Res. Technol.*, vol. 9, no. 6, pp. 14267–14282, Nov. 2020, doi: 10.1016/j.jmrt.2020.10.012.

[122] L. Zhao, Z. Wen, F. Jiang, Z. Zheng, and S. Lu, 'Silk/polyols/GOD microneedle based electrochemical biosensor for continuous glucose

monitoring', *RSC Adv.*, vol. 10, no. 11, pp. 6163–6171, 2020, doi: 10.1039/C9RA10374K.

[123] G. Ducom, B. Laubie, A. Ohannessian, C. Chottier, P. Germain, and V. Chatain, 'Hydrolysis of polydimethylsiloxane fluids in controlled aqueous solutions', *Water Sci. Technol.*, vol. 68, no. 4, pp. 813–820, Aug. 2013, doi: 10.2166/wst.2013.308.

[124] K.-Y. Law, 'Definitions for Hydrophilicity, Hydrophobicity, and Superhydrophobicity: Getting the Basics Right', *J. Phys. Chem. Lett.*, vol. 5, no. 4, pp. 686–688, Feb. 2014, doi: 10.1021/jz402762h.

[125] B. Ruben *et al.*, 'Oxygen plasma treatments of polydimethylsiloxane surfaces: effect of the atomic oxygen on capillary flow in the microchannels', *Micro Nano Lett.*, vol. 12, no. 10, pp. 754–757, Oct. 2017, doi: 10.1049/mnl.2017.0230.

[126] A. Alizadeh, W. Hsu, M. Wang, and H. Daiguji, 'Electroosmotic flow: From microfluidics to nanofluidics', *ELECTROPHORESIS*, vol. 42, no. 7–8, pp. 834–868, Apr. 2021, doi: 10.1002/elps.202000313.

[127] I. Hoek, F. Tho, and W. M. Arnold, 'Sodium hydroxide treatment of PDMS based microfluidic devices', *Lab. Chip*, vol. 10, no. 17, p. 2283, 2010, doi: 10.1039/c004769d.

[128] Z. Wang, A. A. Volinsky, and N. D. Gallant, 'Crosslinking effect on polydimethylsiloxane elastic modulus measured by custom-built compression instrument', *J. Appl. Polym. Sci.*, vol. 131, no. 22, p. n/a-n/a, Nov. 2014, doi: 10.1002/app.41050.

[129] K. Yi, Y. Wang, K. Shi, J. Chi, J. Lyu, and Y. Zhao, 'Aptamer-decorated porous microneedles arrays for extraction and detection of skin interstitial fluid biomarkers', *Biosens. Bioelectron.*, vol. 190, p. 113404, Oct. 2021, doi: 10.1016/j.bios.2021.113404.

[130] K. Takeuchi, N. Takama, B. Kim, K. Sharma, P. Ruther, and O. Paul, ‘A Porous Microneedle Array Connected to Microfluidic System for ISF Collection’, in *2018 IEEE CPMT Symposium Japan (ICSJ)*, Kyoto, Nov. 2018, pp. 85–88. doi: 10.1109/ICSJ.2018.8602945.